DESIGN AND OPTIMIZATION OF FREQUENCY SELECTIVE SURFACES (FSS)

LUO XINGFANG

SCHOOL OF ELECTRICAL & ELECTRONIC ENGINEERING
NANYANG TECHNOLOGICAL UNIVERSITY

2006

Design and Optimization of Frequency Selective Surfaces (FSS)

Luo Xingfang

School of Electrical & Electronic Engineering

A thesis submitted to the Nanyang Technological University
in fulfillment of the requirement for the degree of
Doctor of Philosophy

2006

Statement of Originality

I hereby certify that the work embodied in this thesis is the result of original research and has not been submitted for a higher degree to any other University or Institution.

Date

Luo Xingfang

Acknowledgements

This thesis is the result of three years of work whereby I have been accompanied and supported by many people. It is my pleasure that I have now the opportunity to express my gratitude to all of them.

First of all, I would like to extend my wholehearted thanks to my supervisor, Assoc. Prof. Lee Ching Kwang, for his advice, guidance and encouragement throughout the research project at Nanyang Technological University. I am greatly indebted to his significant time and effort devoted in advising me.

I am grateful to my mentor, Dr. Qing Anyong, for his useful guidance on optimization technique and MoM technique. I would also like to give special thanks to Mr. Teo Peng Thian for some of useful discussion and advice in experimental setup for measurement. Their suggestions and encouragement helped me throughout the time of my study and research in NTU.

I would like to express my gratitude to Nanyang Technological University for financing me throughout these studies. Without the sponsorship, I would not have had the means to fulfill my dreams.

I am deeply indebted to my parents, who taught me the value of hard work by their own examples. They rendered me enormous support during the whole tenure of my research. I would like to share this moment of happiness with them. I am also grateful to my husband for the inspiration and moral support he provided throughout my research work. Without his loving support and understanding, I would never have completed my present work.

Many people have helped me out when I came across difficulties during the development of this thesis. I especially would like to thank my friends Sun Sheng, Sun Chen, Wang Hang, Xu Ying and Wang Wen for their discussions and encouragement in this project. I also would like to thank the lab technicians from Communication Lab IV for their help and logistic support throughout the project. In addition, I would like to express my special thank to staffs of Communication Lab I, Madam Eng Puay Cheng and especially Mr. Lim Cheng Chye, Steve for logistic supports for the use of anechoic chamber at school of EEE, NTU.

Finally, I would like to thank all who had directly or indirectly helped me in this thesis.

Summary

Frequency Selective Surfaces (FSS) have been applied in a number of commercial and defense sectors to provide multiple frequency band operation. The growing popularity of FSS has stimulated the urgent need to develop an efficient algorithm to guide the design of FSS. Presently, synthesizing an FSS with a desired frequency response is usually conducted through a tedious trial and error procedure. Here, the optimization technique is proposed in the design of FSS. Previous work on optimization of FSS has primarily focused on the applications of Genetic Algorithm (GA) with binary-coded. However, existing FSS designs suffer from major drawbacks. Firstly, the unit cell which is generated randomly is complicated and irregular in shape. It is difficult to fabricate and the analytical accuracy for such generated patterns is doubtful. Secondly, although the GA has been employed in the design of FSS, there is still room for researchers to find a much simpler, faster convergent optimization algorithm than GA.

In this thesis, our objective is to develop a more efficient optimization algorithm to optimize the standard, non-irregular FSS unit-cell and dielectric properties. Then we apply this newly developed optimization technique combined with the analytical method to solve the computationally intensive FSS design problem.

The analytical models derived for FSS are essential to the design of FSS. The spectral-domain Method of moments (MoM) is the most popular technique for the analysis of FSS.

It can accurately analyze multi-layered FSS with arbitrary shape elements. However, the existing spectral-domain MoM technique is not applicable to the normal incidence ($\theta = 0^0$) because some formulas are infinite at normal incidence. An improved spectral-domain MoM technique is derived which can be applicable to the normal incidence in this thesis. Another analytical method, the equivalent circuit model (ECM) requires shorter computational time and has been reported that it is accurate for the analysis of some element geometries such as double-square, gridded-square and gridded-double-square elements.

Both GA and differential evolution strategy (DES) are stochastic global optimization methods. The GA can be simply classified as simple genetic algorithm (SGA) and real-coded genetic algorithm (RGA) and their evolvements. In this thesis, three optimization algorithms, SGA, RGA and DES are investigated and compared. DES is found to be the most efficient and robust optimization tool among them because of its fastest convergence. Thus, DES is chosen as optimization tool to apply in the design of FSS.

A novel method using DES coupled with the spectral-domain MoM is proposed in the design of FSS structures with the prescribed performances. The DES is applied to optimize the dimensions and dielectric properties of FSS dipole array. The frequency response of FSS screen is analyzed by employing our improved spectral-domain MoM technique. The objective function is defined as the relative error between actual and prescribed frequency response. The synthesized results obtained for dipole array with and without substrates are in good agreement with the true profiles. In order to validate the predominance of the DES, the RGA is applied to the same design construction for

comparison. The results that the DES displays the faster convergence than the RGA further demonstrate that the DES is a more efficient and robust method in the design of FSS. This method is also applied on the design of band-stop and band-pass filter. Multi-layered hexagon array and gangbuster array are used as optimization objective. Obtained good pass-band and stop-band performances hint that we can optimize hexagon array or gangbuster array to obtain a filter with arbitrarily desired bandwidths using the proposed method without trial and error procedure.

Another novel design method using the DES combined with ECM is proposed to design FSS for multi-band application. The DES is employed to optimize the geometries of FSS unit cell while the ECM is used to analyze the frequency response of FSS with double-square, gridded-square and gridded-double-square array. The objective function is defined in relation to the performances of pass-band and stop-band. Six multi-band design examples are given to demonstrate the efficiency of the proposed method. Compared to the method (trial and error procedure) conducted by previous researchers for the same configuration design objective, one only needs to set the search range of optimization parameters and give the convergence criterion in our proposed method. The program would then automatically seek and find the optimum configuration parameters values in a very short computational time. Two of the designs, a gridded-square array and a double-square array, were fabricated and measured in anechoic chamber at NTU. Good agreements are observed between the simulated and measured results. The fast computational speed demonstrates that the proposed technique (DES coupled with ECM) is very effective and practical in the design of FSS.

List of Abbreviations

3G	3rd Generation
CPU	central processing unit
DES	differential evolution strategy
ECM	equivalent circuit model
EEE	Electrical and Electronic Engineering
EFIE	electric-field integral equation
ES	evolution strategy
FDTD	finite difference time domain
FEM	finite element method
FSS	frequency selective surfaces
GA	genetic algorithm
GSM	Global System for Mobile communications
GPS	Global Positioning System
HFSS	high-frequency structure simulator
MEMS	microelectromechanical system
MGA	micro-genetic algorithm
MoM	method of moments
NASA	National Aeronautics and Space Administration

NN	neural network
NTU	Nanyang Technological University
PEC	perfectly electric conducting
RGA	real-coded genetic algorithm
SA	simulated annealing
SGA	standard genetic algorithm
TE	transverse electric
TM	transverse magnetic

Table of Contents

List of Figures

List of Tables

Chapter 1 Introduction

1.1 Introduction

1.1.1 General Description

Frequency selective surfaces (FSS) are two-dimensional planar periodic arrays which are composed of one or multi-screen (arranged with conducting patch or aperture elements) embedded in one or multi-medium. They behave like spatial filters which reflect over one band of frequencies and are transparent over another.

FSS were first patented by Marconi as periodic structures as early as 1919 [1] and have been extensively studied since 1960s. A thorough review was reported by Mittra *et al* [2]. The first comprehensive book on the topic was compiled by Wu [3]. Vardaxoglou and Munk have also published some practical aspects of the design of FSS [4-6]. In recent years, FSS has been in great demand because of their low loss, flexibility in obtaining various frequency responses by tuning the structure parameters and some potential applications in both the commercial and military sectors to provide multiple frequency band operation.

1.1.2 Applications of FSS

The following is the summary of applications of transparent or opaque FSS arrays.

- FSS have provided the protection from harmful electromagnetic radiation especially in the 2-3 GHz band in the civilian environment, schools and hospitals etc. For example, the screen door of a microwave oven is made of a periodic array with metallic holes and is designed to reflect microwave radiation at 2.45 GHz while being transparent to the visible light allowing the user to look inside the oven.
- FSS have also been found useful in security (military installations, airport etc.) because of their frequency selective shielding capability. FSS are now employed in radomes (terrestrial and airborne), missiles and electromagnetic shielding applications [7-8]. At the operating frequency, the radome is mainly transparent, but reflecting at the out-of-band frequencies. They can also be used as quasi-optical frequency diplexer [9] and absorbers [10].
- The use of FSS has been successfully proven as a mean to increase the communication capabilities of satellite. In space missions such as Voyager, Galileo, and Cassini, the use of dual-reflector antennas with a subreflector made of an FSS has made it possible to share the main reflector among different frequency bands [11-13].
- FSS are able to cut-off unwanted radiation and have been utilized in Pico cellular wireless communications such as the Personal Handy-phone System in office environments to improve efficiency [14]. This is achieved by shielding the windows, floor and ceiling with FSS arrays to prevent leakage of radio waves between offices.
- In the near and far infrared wavelength region, the applications of FSS include filters, polarizers, beam splitters [15-17].

1.1.3 Classification of FSS

There are two fundamental types of FSS. The first consists of the metallic patches on a substrate. This configuration is commonly referred to as capacitive FSS and has a low-pass filter behavior. The other fundamental type consists of apertures on a metallic sheet. It behaves like a high-pass filter and is referred to as an inductive FSS. If the configuration of the elements has resonance characteristics, the capacitive FSS behaves like a band-stop filter around the resonance frequency and the inductive behaves like a band-pass filter. Figure 1-1 shows the typical transmission response of band-pass and band-stop FSS, where f_r stands for the resonant frequency of FSS structures.

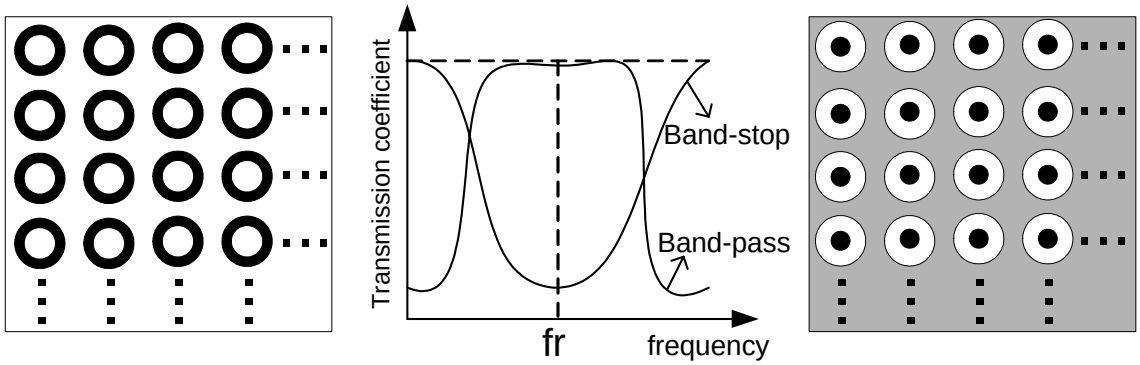

Figure 1-1 Typical band-stop and band-pass FSS (a) band-stop FSS (b) transmission response of band-stop and band-pass (c) band-pass FSS

FSS can be composed of passive or active elements. Passive elements are excited by incident plane wave to produce a discrete spectrum of transmitted and reflected plane waves. The amplitude and propagation direction of these waves depend on the exciting wave's propagation direction, polarization, and frequency. Polarization states of the

excitation field are typically divided into the orthogonal TE (electric field perpendicular to plane of incidence) and TM (magnetic field perpendicular to plane of incidence). The advantage of this kind of FSS is that they are relatively easy to design and manufacture but the disadvantage is that they are not reconfigurable once this surface is fabricated. On the other hand, FSS are active if elements are incorporated with PIN diodes [18-21], MEMS switches [22] or optically excited by semiconductor substrates such as silicon [23-24]. In the active FSS, the frequency properties can be tuned under the control of the semiconductor devices placed in and between FSS elements or optical illumination. These active devices make the size of the FSS much smaller than a passive one and are reconfigurable. However, the design and fabrication of active FSS is very challenging.

FSS can also be classified as thin or thick screen according to the thickness of FSS screen relative to the wavelength. Thin screen FSS are usually referred to as a screen with patch or aperture elements with thickness less than 0.001λ, where λ is the wavelength at the resonant frequency. A thin FSS is accurately modeled as “infinitely thin” in numerical simulations. Thin screen FSS are lightweight, small in volume and easy to fabricate with the conventional printed circuit technology. Thick screen FSS [25-26] are made of array elements with electrically larger thickness, and are mostly apertures used for high-pass applications. Compared with thin screen FSS, the advantage of thick screen FSS is that closely spaced frequency bands, shaper frequency roll-off and wider pass-band bandwidths. However, the conductivity of the structure can be approximated by a perfectly electric conducting (PEC) plate if materials with high conductivity like copper are used. If the material is not a metal with high conductivity, the FSS performance degrades and the PEC approximation is not applicable.

1.1.4 Definition of Grating Lobes

Figure 1-2 shows the onset of grating lobes in relation to the incident wave on FSS structure. Grating lobes are unwanted secondary main propagation waves that can occur at angles with higher order constructive interference when the inter-element spacing is electrically large.

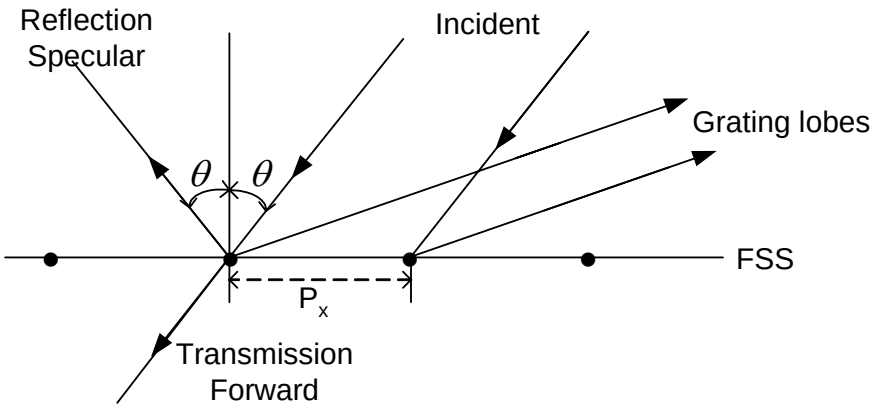

Figure 1-2 Illustration of grating lobes with the plane wave incidence on FSS structure

The onset condition of the lowest grating lobe frequency f_g is [5]

$$f_g = \frac{c}{P_x(1+\sin\theta)} \tag{1-1}$$

where P_x, θ and c are inter-element spacing, incident angle and speed of light propagation respectively. The lowest grating lobe frequency depends only on the angle of incidence and the inter-element spacing. For FSS array embedded on dielectric substrates, the lowest frequency of the onset of grating lobes will occur at

$$f_g = \frac{c}{P_x(\sqrt{\varepsilon_r}+\sin\theta)} \tag{1-2}$$

where ε_r is the dielectric constant of the substrate. A general rule for avoiding grating lobes is that the inter-element spacing must be less than one free space wavelength at normal incidence. The most practical method of avoiding grating lobes is to make the inter-element spacing no more than half of the wavelength of the highest frequency in the transmission or reflection band [5].

1.1.5 Factors Influencing the Performance in the Design of FSS

The frequency response and the filtering characteristics of FSS depend on the following physical and geometrical factors

- The geometry of the FSS elements (shape, dimensions and thickness of conductor).
- The thickness and the permittivity of homogeneous dielectric slabs as FSS substrates.
- The periodicity of the FSS array (inter-element spacing).
- The conductivity of the FSS elements.
- The number of FSS screens and dielectric layers in multi-layer FSS structures.
- The polarization and the angle of the incident field.

In the design of FSS, the choice of FSS element geometry is very important. The elements are selected based on the resonant frequency, bandwidth and sensitivity with respect to the angle of wave incidence. Parameters of element like shape, dimensions, lattice geometry and grating lobes must be taken into account according to the design specifications. Some standard FSS unit cell geometries are shown in Figure 1-3. A good designed element must have a stable resonant frequency response with respect to variation of incident angles, a large bandwidth, a low cross-polarization level and a small band separation between the reflection and transmission frequencies.

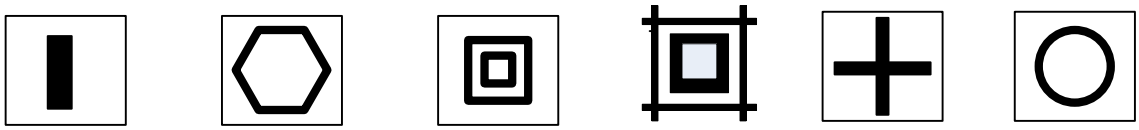

(a) (b) (c) (d) (e) (f)

Figure 1-3 Some typical FSS unit cell geometries. (a) Dipole (b) Hexagon (c) Double square (d) Gridded square (e) Cross dipole (f) Ring

In the design of FSS, one of the required specifications is the resonant frequency. The resonant frequency of FSS is determined by the geometry of elements [5]. For strip dipole element, the dipole will resonate when its length is approximately half a wavelength. For closed-loop types such as the square loop and the ring elements, resonance occurs when their average circumference is approximately one wavelength. Furthermore, the resonant frequency of FSS also depends heavily on the dielectric constant and thickness. The presence of dielectrics will shift the resonance wavelength of the FSS compared to the value in air to a longer wavelength. For FSS embedded in substrates, the dielectric properties must be included in the evaluation of effective wavelength. Resonant frequency increases toward that of free space as the dielectric thickness is reduced. Dielectrics are often used for stabilization of the resonant frequency with respect to the variation of the incident angles and also for structural support.

In the design of FSS, another required specification is the bandwidths of frequency response. In general, the bandwidths of FSS frequency response depend largely on the inter-element spacing. Decreasing the inter-element spacing will increase the reflection or transmission bandwidths. Furthermore, the improvement of the bandwidth also includes multi-layered FSS screens and increase of thickness of the supporting dielectric layer.

In the design of FSS, many applications also require the resonant curves to have flattop and faster roll off responses. This can be achieved by several planar arrays embedded in multi-layered dielectric mediums and cascaded together to obtain an enhanced frequency response. In general, multi-layered FSS have broader bandwidths and close band centre spacing compared with the single layer FSS [27]. However, the multi-layered FSS structures are more difficult and costly to manufacture and align together. The alignment procedure increases the cost and complexity over a single layer FSS in proportion to the number of stacked FSS.

The design of FSS structures for multi-band application has attracted much attention due to increasing demands on multi-functionality of antennas for communications. Various approaches can be found in the literatures [28-30]. Complex multi-band FSS are the result of one, or the combination of several of the following techniques: layered or stacked FSS, perturbation of a single-layered FSS, or the use of multi-resonant elements such as the concentric loops.

In this thesis, work on thin, perfectly conducting, passive, planar FSS is presented.

1.2 Past Research on the Design of FSS and Motivation of this Thesis

An increasing interest for researchers has been generated recently to design FSS for prescribed performance requirements in the multi-band applications. The design of FSS is a very challenging problem because their performances are dependent on many parameters such as the geometry and dimension of elements, the number of FSS screens and dielectric layers, and their electrical properties. Although the numerical analysis of

FSS has been reported extensively [2-4], there is still no much study concentrated on the design of FSS. Presently, synthesizing a FSS with a desired frequency response is conducted through a tedious trial and error procedure [12-13, 31-32]. However, this approach is heavily dependent on the designer's experience. Hence, a lot of time is wasted on the experiments for trying different parameters and may not be able to obtain the required results. For the experienced designers, they also have to try many configurations before fabrication and measurement. It is not only computationally expensive but also difficult to guarantee that it is an optimum design. Thus, optimization approach can overcome this problem and is proposed in the design of FSS structures in this thesis. It is more systematic and not only assures a high degree of freedom in the definition of the elements, but also is instrumental in realizing FSS that meet the prescribed frequency specifications.

The optimization of FSS structures includes two parts, the analysis of FSS and optimization algorithm. These two parts are linked by the objective function. The relative objective function gives a measurement on how close the optimization results approach the true profile. If the synthesized results fail to satisfy the desired specifications, the designable (optimization) parameters of the FSS are altered and put back into the new generation. The sequence of FSS analysis, comparison with the desired performance, and modification of optimization parameters is performed iteratively until the combined composites exhibit the desired frequency response for a required frequency response.

The theory of phased array antennas provides the starting point for the study of analyzing FSS. Various numerical methods such as the method of moments (MoM) [2-4], the equivalent circuit model (ECM) [12-13, 31-32], the finite element method (FEM) [33]

and the finite difference time domain (FDTD) [34] have been developed to predict the frequency characteristics of FSS structures. Among the many numerical techniques available, the MoM technique is the most popular for the analysis of FSS structures. The MoM technique is based on the work of Harrington who applied MoM to electromagnetic fields at the beginning of the 1960's [35]. It is a widely used numerical technique for electromagnetic problems such as phased arrays, waveguide discontinuities, antennas, scattering and filter design. The other analysis method, ECM in general is a less accurate technique but requires very short computational time in providing frequency response. ECM models for various FSS elements are based on empirical study. ECM has proven to be a useful tool for designing some printed FSS such as double-square, gridded-square and gridded-double-square array [12-13, 31-32]. FSS can also be modeled by commercial programs based on FEM (Ansoft HFSS) [36] or MoM (Ansoft Designer) [37].

The spectral-domain MoM technique can accurately analyze multi-layered FSS with arbitrary shape elements. However, the existing spectral-domain MoM technique is not applicable to the normal incidence ($\theta = 0$) because some formulas (such as transmission & reflection calculation, multi-layered Green function immittance matrix and the tangential incident electric field) are infinite at normal incidence. Therefore, a very small incident angle is considered as normal incidence in practice. This is imperfect and the performance of FSS structures at normal incidence is principal and preferred. Thus, it is necessary to re-derive and improve the spectral-domain MoM technique to handle above drawback. This is one of the motivations for this research. Furthermore, the existing spectral-domain MoM technique mostly employs the roof-top basis function which only can solve the problem where the conductor current flows towards x or y direction and no

continuous current exists in the border of unit cell. It is limited to analyze some arrays such as gangbuster array and hexagon array which have been proved good performance especially on broadband application [5]. The second motivation of this thesis is to find a way to analyze some arrays with good wide-band performance like gangbuster array and hexagon array.

For the optimization algorithm applied on the design of FSS, previous works have primarily focused on the applications of the global optimization algorithm, genetic algorithm (GA). In their design, Genetic Algorithm with binary-coded can randomly generate the cell structure of FSS screen with 16×16 (or 32×32) gridded discretization [38-42]. The frequency response of FSS structure is analyzed using spectral-domain MoM with roof-top basis function. Figure 1-4 shows the unit cell ((a) and (b)) or array ((c)) presented in [38, 41].

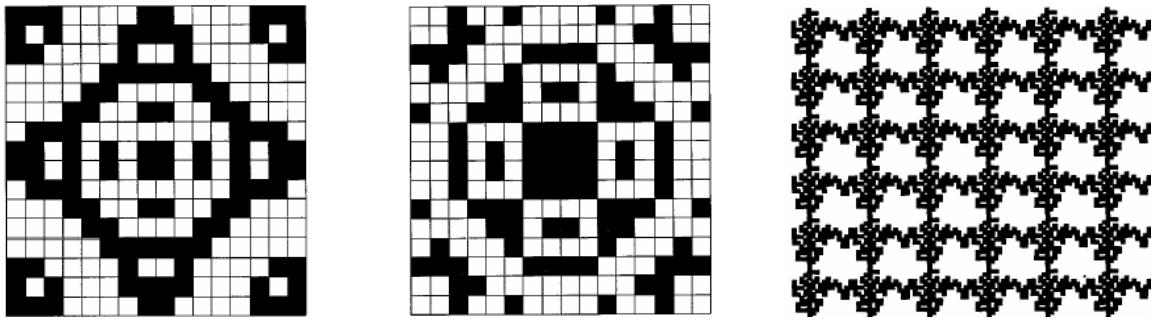

(a) (b) (c)

Figure 1-4 Unit cell presented in the previous researcher's work

However, existing FSS design suffers from major drawbacks. 1) The unit cell produced randomly is complicated and irregular in shape which is difficult to fabricate.

The performances of FSS structures are very sensitive to the geometries of the unit cell. It is difficult to obtain a good agreement between simulation and measurement under so many control parameters. 2) Continuous current exists on the border of a unit cell which needs to be especially treated otherwise the wrong simulation results will be obtained [43]. However it is unavoidable to produce the non-vanishing current crossing the border of a unit cell using their approach. In addition, no measured results are shown in their publications to verify the accuracy of the analysis for the generated structure. The analytical correctness for the generated structure is doubtful because only roof-top basis function is employed in their optimized approach. 3) Their approach (gridded discretization) is limited only for the analysis where the current flowing in x or y direction because the roof-top basis function is employed. It is unable to deal with some geometries with the current at slanting direction. As a result, some geometries with good performance may be missed and the generated structures may not be the optimum design using this approach. Therefore, in this thesis the typical FSS unit-cell is taken as optimization objective instead of randomly generating the geometries of unit cell from the optimization. Furthermore, although GA has been working on the design of FSS, there is still much left for researchers to find a much simpler, faster convergent optimization This forms another motivation for this research.

1.3 Objectives

In responding to the problems as mentioned before, one of our objectives is to improve the spectral-domain MoM technique so that it is applicable to the normal incidence. This is conducted by re-deriving the formulas for multi-layered Green's function and the

transmission & reflection coefficient expression. Furthermore, the other basis function should be considered to be employed in order to analyze some arrays such as gangbuster and hexagon array successfully.

The other prime objective of this thesis is to develop a more efficient optimization algorithm to tune the parameters and dielectric properties of the standard, non-irregular structure. In comparison with the performance of other optimization algorithms (standard genetic algorithm (SGA) and real-coded genetic algorithm (RGA)), differential evolution strategy (DES) has the fastest convergence performance and is found to be the most efficient optimization algorithms among them (This point will be validated in Chapter 3).

Our third objective is to apply this newly improved optimization technique to incorporate with analytical methods for the design of FSS. Therefore, DES combined with our improved spectral-domain MoM is proposed in the design of FSS with prescribed performance. Another analytical method, equivalent circuit model (ECM) has rapid computational time and is relatively accurate for some element geometries such as double-square, gridded-square and gridded-double-square array. Also, the design for multi-band FSS application is conducted through the combination of DES with ECM.

1.4 Major Contributions of the Thesis

The thesis focuses on the design and optimization of FSS. The major contributions of this thesis are:

1) An improved spectral-domain MoM technique is derived. Compared to the approach presented by Mittra and Chan [2-3], our method is applicable to the normal incidence

($\theta = 0$). In the Mittra and Chan's method, the denominator in the formulations of transmission & reflection coefficients and multi-layered Green's function equal to zero and become infinite at normal incidence. We overcome this problem through three aspects. Firstly, the expressions of transmission & reflection are derived based on electric field instead of vector electric potentials. Then, there are some revisions in the derivation of multi-layered Green's function. Lastly, the incident electric field is expressed in spherical coordinate system to avoid the tangential incident electric field vanishes at normal incidence. Furthermore, the other analytical method for FSS structures, ECM is reviewed. The thorough review creates a strong foundation for further study of FSS design.

2) Two types of global optimization algorithms, SGA and RGA are investigated. A novel optimization technique, DES is developed here and its performance is compared with SGA and RGA. DES is found to be the most efficient optimization method to apply in the design of FSS. Meanwhile, controlling parameters in DES optimization are also investigated.

3) A novel method on the design of FSS using DES coupled with spectral-domain MoM is proposed. The DES is employed to optimize the dimensions of the FSS unit cell and dielectric properties. The analysis of scattering from FSS screen is solved by the use of our derived spectral-domain MoM technique. The synthesized results are in good agreement with the true profiles in the design of FSS dipole array. This method is also used in the design of multi-layered hexagon array and gangbuster array. Broadband band-pass and band-stop filters are obtained. The results demonstrate the efficiency of the proposed FSS design method.

4) Another novel method on the design of multi-band FSS, which combines the DES (for optimization) with ECM (for analysis), is suggested. Some practical configuration designs such as double-square, gridded-square and gridded-double-square elements for multi-band application are studied to demonstrate the efficiency of proposed FSS design method. Two of designs were fabricated and experimentally tested. Good agreements between the simulated and measured results are obtained. Compared with previous researcher's works for the same design objective, our proposed method avoids the trial and error procedure. The required configuration can be easily obtained through DES optimization with the set range of optimization parameters and the defined objective function for special problem in a very short computational time.

1.5 Organization of the Thesis

The thesis consists of six chapters. Chapter 1 provides the brief literature review on the FSS. The past research on the design of FSS is reviewed and the motivation of our research is described. The objective of the thesis is presented and the major contributions of the research are listed. In chapter 2, two numerical methods for the analysis of FSS, spectral-domain MoM and ECM are reviewed. An improved spectral-domain MoM technique is proposed and derived which is applicable for normal incidence. The differences between our proposed method and Mittra and Chan's are hightlighted. Three global optimization algorithms, SGA, RGA and DES are investigated and compared in Chapter 3. DES is found to be the most efficient and robust optimization tool among them because of its fastest convergence. The parameters control in DES optimization is also investigated. In Chapter 4, DES is proposed to optimize the standard, non-irregular

geometries of FSS unit cell and dielectric properties. The analysis of FSS frequency response is conducted by our derived spectral-domain MoM technique. The novel design method is demonstrated through constructing FSS dipole array with and without substrates. The design of band-pass and band-stop filter using multi-layered hexagon and gangbuster array is also presented. In Chapter 5, a novel method using DES coupled with ECM is proposed to apply in the design of multi-band FSS structures. Six design examples are shown to demonstrate the efficiency of the proposed method. Two of the designs, a gridded-square array and a double-square array are manufactured and their measured results are presented. Summary and conclusion are presented in Chapter 6. The chapter also includes recommendations for future research works.

Chapter 2 Numerical Methods for the Analysis of Frequency Selective Surfaces

2.1 Introduction

As mentioned before, the spectral-domain MoM technique is the most popular for the analysis of FSS structures since it can analyze the multi-layered FSS structures accurately. The other analysis method, ECM in general is a less accurate technique but requires relatively shorter computational time in providing frequency response. It has been reported that ECM can accurately analyze some printed FSS such as double-square, gridded-square and gridded-double-square array [12-13, 31-32]. In this thesis, the spectral-domain MoM and ECM are selected as the numerical analytical tools of FSS frequency response for applying in the design of FSS with prescribed performance. These two analytical methods are reviewed in this chapter. Furthermore, some improvements on the spectral-domain MoM technique are proposed and implemented in this chapter which is applicable for normal incidence.

Section 2.2 provides the detailed description and formulations of analyzing FSS using our improved spectral-domain MoM technique. Previous researchers replaced the normal

incidence with a small incident angle because some formulas become infinite formulations exist in the expressions of transmission & reflection and Green's function at normal incidence. Our improved spectral-domain MoM technique avoids this drawback which can be applicable to the normal incidence. Furthermore, the piecewise sinusoidal basis function is proposed to apply in the analysis of hexagon and gangbuster array instead of rooftop basis function. This proposed method is employed as an analytical tool in the design of FSS with prescribed frequency response, which is presented in Chapter 4.

Section 2.3 presents the background and mathematical formulations of analyzing FSS using ECM. This technique is used as an analytical tool in the design of multi-band FSS, which is presented in Chapter 5.

2.2 Analysis of FSS using Spectral-domain Method of Moments (MoM)

In 1984, Tsao and Mittra presented a method known as the spectral-domain MoM technique to calculate the scattered fields from FSS [44]. A summary of spectral-domain MoM techniques for analyzing FSS was published by Mittra, Chan and Cwik [2] in 1988. The spectral-domain MoM method was also employed by Wu [3] and Vardaxoglou [4]. In this method, the incident plane wave induces electric surface currents on the conductors of the FSS (magnetic currents for slot FSS). An integral equation for a single unit cell relates the scattered fields from the FSS screen to the surface currents on the screen induced by the incident field. According to Floquet's theorem and Fourier transform, the convolution integral equation is converted to an infinite summation for periodic cells and is reduced to an algebraic matrix equation in spectral domain. The unknown current coefficients can be

determined by applying the spectral-domain Galerkin's method. The scattered fields are easily obtained once the surface current is known.

In spectral-domain MoM technique, there are two categories of basis functions used to represent the unknown surface currents, namely, entire-domain and sub-domain basis functions. The entire-domain basis functions are applicable only on standard element geometries (such as dipole, cross dipole, Jerusalem cross, circular ring etc.), while the sub-domain basis functions allow general patch geometries. The computation time for spectral-domain MoM in FSS applications is usually dominated by the calculation of the Green's function and matrix elements because each element of the matrix involves a doubly infinite summation and requires long convergence time. For standard element geometries, the entire-domain basis functions are usually preferable, since the matrix to invert is usually much smaller than the sub-domain one, and hence, the required computational time is shorter. It is also well known that the double summation over the Floquet modes is usually more rapidly convergent in the entire-domain case, also yielding shorter computational time.

The spectral-domain MoM technique has the ability to model patch elements (or apertures) of arbitrary shape of FSS. It can also model multi-layered FSS accurately. However, in the reported articles [2-3], it is not applicable for normal incidence. The existing problem is caused by 1) The tangential incident electric field vanishes at normal incidence. 2) In the derivation of multi-layered Green's function, the immittance matrix is infinite at normal incidence. 3) The formulas for calculating the transmission & reflection coefficient are infinite at normal incidence. The technique of spectral-domain MoM proposed in this thesis avoids these drawbacks [45]. This is achieved by expressing the

incident electric field in spherical coordinate system, some revisions in the derivation of multi-layered Green's function and developing the electric field-based reflection and transmission coefficients instead of vector potentials.

2.2.1 Freestanding FSS

An infinite freestanding FSS structure is shown in Figure 2-1. Initially, the relationship between the scattered electric field from the FSS screen and the induced surface currents on the screen by the incident field is derived.

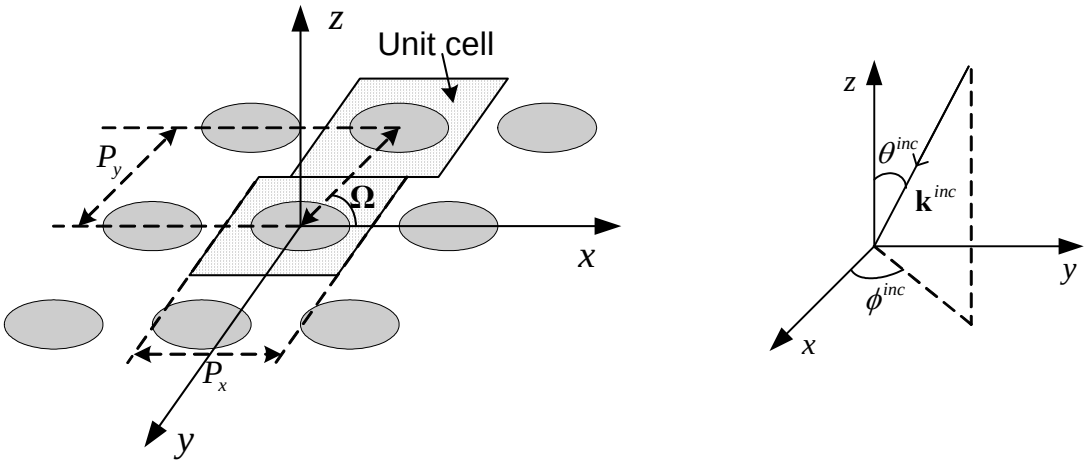

(a) (b)

Figure 2-1 Skewed freestanding FSS (a) geometry (b) incidence

The scattered electric field from a conducting patch at point r due to a source r' is

$$\mathbf{E}^s(\mathbf{r}) = -j\omega\mu_0\mathbf{A}(\mathbf{r}) + \frac{1}{j\omega\varepsilon_0}\nabla\left[\nabla\cdot\mathbf{A}(\mathbf{r})\right] \tag{2-1}$$

where μ_0 and ε_0 are the permeability and permittivity of the free space,

$$\mathbf{A}(\mathbf{r}) = \int_S G(\mathbf{r},\mathbf{r}')\mathbf{J}(\mathbf{r})\,d\mathbf{r}' = G^*\mathbf{J} \tag{2-2}$$

$$G(\mathbf{r},\mathbf{r}') = \frac{e^{-jk_0|\mathbf{r}-\mathbf{r}'|}}{4\pi|\mathbf{r}-\mathbf{r}'|} \tag{2-3}$$

The wave number is $k_0 = \omega\sqrt{\mu_0\varepsilon_0}$, the asterisk presents a convolution operation, $\mathbf{J}$ is the induced surface current on the conductor, and G is the free-space Green's function.

Since the tangential electric field vanishes on the surface S of the conducting patch, the boundary condition is

$$\left[\mathbf{E}^s(\mathbf{r}) + \mathbf{E}^{inc}(\mathbf{r})\right]\Big|_{\mathbf{r}\in S} = 0 \tag{2-4}$$

The electric-field integral equation (EFIE) for the perfectly electric conducting (PEC) patch can be obtained

$$-\mathbf{E}^{inc}(\mathbf{r})\Big|_{\mathbf{r}\in S} = \left\{-j\omega\mu_0\mathbf{A}(\mathbf{r}) + \frac{1}{j\omega\varepsilon_0}\nabla\left[\nabla\cdot\mathbf{A}(\mathbf{r})\right]\right\}\Big|_{\mathbf{r}\in S} \tag{2-5}$$

For a planar thin surface only surface current components J_x and J_y exist. We can get the matrix form of (2-5)

$$-\begin{bmatrix} E_x^{inc}(\mathbf{r}) \\ E_y^{inc}(\mathbf{r}) \end{bmatrix}\Bigg|_{\mathbf{r}\in S} = \frac{1}{j\omega\varepsilon_0}\begin{bmatrix} k_0^2 + \dfrac{\partial^2}{\partial x^2} & \dfrac{\partial^2}{\partial x\partial y} \\ \dfrac{\partial^2}{\partial x\partial y} & k_0^2 + \dfrac{\partial^2}{\partial y^2} \end{bmatrix}\begin{bmatrix} A_x(\mathbf{r}) \\ A_y(\mathbf{r}) \end{bmatrix}\Bigg|_{\mathbf{r}\in S} \tag{2-6}$$

Defining the Fourier transform pair as

$$\begin{aligned} \tilde{f}(\alpha,\beta) &= \int_{-\infty}^{\infty}\int_{-\infty}^{\infty} f(x,y)e^{-j\alpha x}e^{-j\beta y}dxdy \\ f(x,y) &= \frac{1}{(2\pi)^2}\int_{-\infty}^{\infty}\int_{-\infty}^{\infty} \tilde{f}(\alpha,\beta)e^{j\alpha x}e^{j\beta y}d\alpha d\beta \end{aligned} \tag{2-7}$$

In (2-6), $A_x = G^* J_x$, $A_y = G^* J_y$. In the Fourier domain, $\tilde{A}_x = \tilde{G}\tilde{J}_x$, $\tilde{A}_y = \tilde{G}\tilde{J}_y$. After the inverse Fourier transform of (2-6), by $\partial \mathbf{A}/\partial x \leftrightarrow j\alpha\tilde{\mathbf{A}}$, $\partial^2 \mathbf{A}/\partial x^2 \leftrightarrow -\alpha^2\tilde{\mathbf{A}}$, $\partial \mathbf{A}/\partial y \leftrightarrow j\beta\tilde{\mathbf{A}}$, $\partial^2 \mathbf{A}/\partial y^2 \leftrightarrow -\beta^2\tilde{\mathbf{A}}$, we can obtain the expression in spatial domain

$$
\begin{aligned}
&-\left[\begin{matrix} E_x^{inc}(\mathbf{r}) \\ E_y^{inc}(\mathbf{r}) \end{matrix}\right]\Bigg|_{\mathbf{r}\in S} \\
&= \frac{1}{(2\pi)^2 j\omega\varepsilon_0} \int_{-\infty}^{\infty}\int_{-\infty}^{\infty} \begin{bmatrix} k_0^2-\alpha^2 & -\alpha\beta \\ -\alpha\beta & k_0^2-\beta^2 \end{bmatrix} \tilde{G}(\alpha,\beta) \begin{bmatrix} \tilde{J}_x(\alpha,\beta) \\ \tilde{J}_y(\alpha,\beta) \end{bmatrix} e^{j\alpha x} e^{j\beta y} d\alpha d\beta \qquad (2\text{-}8) \\
&= \frac{1}{(2\pi)^2} \int_{-\infty}^{\infty}\int_{-\infty}^{\infty} \begin{bmatrix} \tilde{G}_{xx}(\alpha,\beta) & \tilde{G}_{xy}(\alpha,\beta) \\ \tilde{G}_{yx}(\alpha,\beta) & \tilde{G}_{yy}(\alpha,\beta) \end{bmatrix} \begin{bmatrix} \tilde{J}_x(\alpha,\beta) \\ \tilde{J}_y(\alpha,\beta) \end{bmatrix} e^{j\alpha x} e^{j\beta y} d\alpha d\beta
\end{aligned}
$$

where

$$
\begin{bmatrix} E_x^{inc}(\mathbf{r}) \\ E_y^{inc}(\mathbf{r}) \end{bmatrix} = \begin{bmatrix} E_{x0}^{inc} \\ E_{y0}^{inc} \end{bmatrix} e^{jk_x^{inc}x} e^{jk_y^{inc}y} \qquad (2\text{-}9)
$$

$$
k_x^{inc} = k_0 \sin\theta^{inc} \cos\phi^{inc}, \quad k_y^{inc} = k_0 \sin\theta^{inc} \sin\phi^{inc} \qquad (2\text{-}10)
$$

$$
\tilde{G}(\alpha,\beta) = \begin{cases} \dfrac{-j}{2\sqrt{k_0^2-\alpha^2-\beta^2}}, & k_0^2 > \alpha^2+\beta^2 \\ \dfrac{1}{2\sqrt{\alpha^2+\beta^2-k_0^2}}, & otherwise \end{cases} \qquad (2\text{-}11)
$$

$$
\begin{bmatrix} \tilde{G}_{xx}(\alpha,\beta) & \tilde{G}_{xy}(\alpha,\beta) \\ \tilde{G}_{yx}(\alpha,\beta) & \tilde{G}_{yy}(\alpha,\beta) \end{bmatrix} = \frac{1}{j\omega\varepsilon_0} \begin{bmatrix} k_0^2-\alpha^2 & -\alpha\beta \\ -\alpha\beta & k_0^2-\beta^2 \end{bmatrix} \tilde{G}(\alpha,\beta) \qquad (2\text{-}12)
$$

Applying Floquet's theorem for periodic structure, $J(x,y)$ can be expressed as

$$
J(x,y) = \sum_{m=-\infty}^{\infty}\sum_{n=-\infty}^{\infty} \tilde{J}_{mn} e^{j(2m\pi/P_x + k_x^{inc})x} e^{j(2n\pi/P_y + k_x^{inc})y} \qquad (2\text{-}13)
$$

where, P_x and P_y are the periodicity in the x and oblique direction respectively. k_x^{inc} and k_y^{inc} are the incident wave number in the x and y direction respectively. The derivation of (2-13) can be found in Appendix B. Substituted (2-13) into (2-8), we can obtain

$$\begin{aligned} &-\begin{bmatrix} E_x^{inc}(x,y) \\ E_y^{inc}(x,y) \end{bmatrix} \\ &= \sum_{m=-\infty}^{\infty}\sum_{n=-\infty}^{\infty} \begin{bmatrix} \tilde{G}_{xx}(\alpha_{mn},\beta_{mn}) & \tilde{G}_{xy}(\alpha_{mn},\beta_{mn}) \\ \tilde{G}_{yx}(\alpha_{mn},\beta_{mn}) & \tilde{G}_{yy}(\alpha_{mn},\beta_{mn}) \end{bmatrix} \begin{bmatrix} \tilde{J}_x(\alpha_{mn},\beta_{mn}) \\ \tilde{J}_y(\alpha_{mn},\beta_{mn}) \end{bmatrix} e^{j\alpha_{mn}x} e^{j\beta_{mn}y} \end{aligned} \tag{2-14}$$

where

$$\begin{bmatrix} \tilde{G}_{xx}(\alpha_{mn},\beta_{mn}) & \tilde{G}_{xy}(\alpha_{mn},\beta_{mn}) \\ \tilde{G}_{yx}(\alpha_{mn},\beta_{mn}) & \tilde{G}_{yy}(\alpha_{mn},\beta_{mn}) \end{bmatrix} = \frac{1}{j\omega\varepsilon_0} \begin{bmatrix} k_0^2-\alpha_{mn}^2 & -\alpha_{mn}\beta_{mn} \\ -\alpha_{mn}\beta_{mn} & k_0^2-\beta_{mn}^2 \end{bmatrix} \tilde{G}(\alpha_{mn},\beta_{mn})$$

$$\begin{aligned} \alpha_{mn} &= k_x^{inc} + \frac{2m\pi}{P_x} \\ \beta_{mn} &= k_y^{inc} + \frac{2n\pi}{P_y \sin\Omega} - \frac{2m\pi}{P_x}\cot\Omega \end{aligned} \tag{2-15}$$

Ω is the skew angle for the skewed FSS as shown in Figure 2-1(a).

Expand the surface current as

$$\begin{bmatrix} J_x(x,y) \\ J_y(x,y) \end{bmatrix} = \begin{bmatrix} \sum_{i=1}^{M} C_{xi} J_{xi}(x,y) \\ \sum_{j=1}^{N} C_{yj} J_{yj}(x,y) \end{bmatrix} \tag{2-16}$$

In Galerkin's method, the test function is chosen to be identical to the basis function. Thus, applying Galerkin's method, we have

$$-\begin{bmatrix} E_{x0}^{inc}\tilde{J}_{x1}^{*}(\alpha_{00},\beta_{00}) \\ \vdots \\ E_{x0}^{inc}\tilde{J}_{xM}^{*}(\alpha_{00},\beta_{00}) \\ E_{y0}^{inc}\tilde{J}_{y1}^{*}(\alpha_{00},\beta_{00}) \\ \vdots \\ E_{y0}^{inc}\tilde{J}_{yN}^{*}(\alpha_{00},\beta_{00}) \end{bmatrix} = \sum_{m=-\infty}^{\infty}\sum_{n=-\infty}^{\infty} \begin{bmatrix} \tilde{J}_{x1}^{*}(\alpha_{mn},\beta_{mn}) & & \\ \vdots & \mathbf{0} & \\ \tilde{J}_{xM}^{*}(\alpha_{mn},\beta_{mn}) & & \\ & \tilde{J}_{y1}^{*}(\alpha_{mn},\beta_{mn}) & \\ \mathbf{0} & \vdots & \\ & \tilde{J}_{yN}^{*}(\alpha_{mn},\beta_{mn}) & \end{bmatrix} \cdot \begin{bmatrix} \tilde{G}_{xx} & \tilde{G}_{xy} \\ \tilde{G}_{yx} & \tilde{G}_{yy} \end{bmatrix}$$

$$\cdot \begin{bmatrix} \tilde{J}_{x1}(\alpha_{mn},\beta_{mn}) & \cdots & \tilde{J}_{xM}(\alpha_{mn},\beta_{mn}) & & & \\ & \mathbf{0} & & \tilde{J}_{y1}(\alpha_{mn},\beta_{mn}) & \cdots & \tilde{J}_{yN}(\alpha_{mn},\beta_{mn}) \end{bmatrix} \cdot \begin{bmatrix} C_{x1} \\ \vdots \\ C_{xM} \\ C_{y1} \\ \vdots \\ C_{yN} \end{bmatrix} \tag{2-17}$$

From (2-4) and (2-14), the scattered electric fields can be expressed as

$$\begin{aligned} \begin{bmatrix} E_x^s(\mathbf{r}) \\ E_y^s(\mathbf{r}) \end{bmatrix} &= \sum_{m=-\infty}^{\infty}\sum_{n=-\infty}^{\infty} \begin{bmatrix} \tilde{G}_{xx}(\alpha_{mn},\beta_{mn}) & \tilde{G}_{xy}(\alpha_{mn},\beta_{mn}) \\ \tilde{G}_{yx}(\alpha_{mn},\beta_{mn}) & \tilde{G}_{yy}(\alpha_{mn},\beta_{mn}) \end{bmatrix} \begin{bmatrix} \tilde{J}_x(\alpha_{mn},\beta_{mn}) \\ \tilde{J}_y(\alpha_{mn},\beta_{mn}) \end{bmatrix} e^{j\alpha_{mn}x} e^{j\beta_{mn}y} \\ &= \sum_{m=-\infty}^{\infty}\sum_{n=-\infty}^{\infty} \tilde{\mathbf{E}}_{mn}^{s} e^{j\alpha_{mn}x} e^{j\beta_{mn}y} \end{aligned} \tag{2-18}$$

2.2.2 Rooftop Basis Function and Piecewise Sinusoidal Basis Function

The entire-domain basis functions for some standard FSS geometries can be found in [3]. However, for arbitrary unit-cell geometries, suitable entire-domain basis functions are not available. Therefore, it is necessary to employ the sub-domain basis functions to treat FSS screens. One of the most frequently used sub-domain basis functions is the rooftop function. It has a triangular or piecewise linear dependence in the direction of the current and a pulse or stepwise-constant dependence in the orthogonal direction as shown in Figure 2-2. It is expedient to discretize the unit cell into a grid and applied with the equal-size rooftop basis functions.

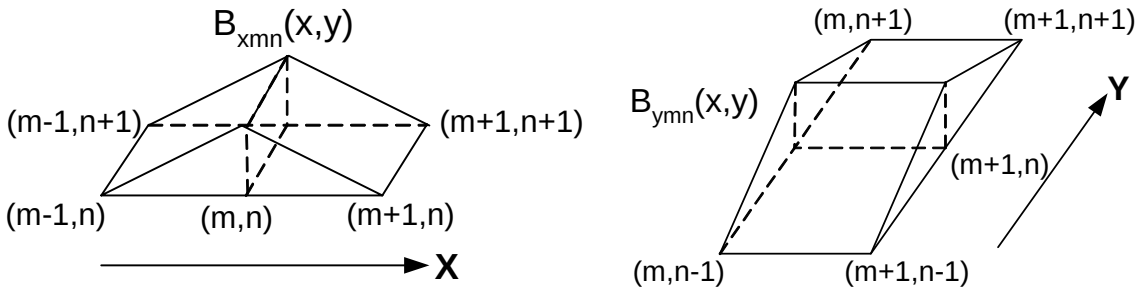

Figure 2-2 Rooftop basis functions

The current basis functions in spatial domain are described by the following equations

$$B_{xmn}(x,y) = \Lambda_x(m)\Pi_y(n+\tfrac{1}{2}) \tag{2-19}$$

$$B_{ymn}(x,y) = \Pi_x(m+\tfrac{1}{2})\Lambda_y(n) \tag{2-20}$$

where

$$\Lambda_x(m) = \begin{cases} 1-\left|x-m\Delta x\right|/\Delta x, & \left|x-m\Delta x\right| \le \Delta x \\ 0, & elsewhere \end{cases}, \qquad \Pi_y(n+\tfrac{1}{2}) = \begin{cases} 1, & \left|y-(n+\tfrac{1}{2})\Delta y\right| < \Delta y/2 \\ 0, & elsewhere \end{cases}$$

$$\Lambda_y(n) = \begin{cases} 1-\left|y-n\Delta y\right|/\Delta y, & \left|y-n\Delta y\right| < \Delta y \\ 0, & elsewhere \end{cases}, \qquad \Pi_x(m+\tfrac{1}{2}) = \begin{cases} 1, & \left|x-(m+\tfrac{1}{2})\Delta x\right| < \Delta x/2 \\ 0, & elsewhere \end{cases}$$

$$\Delta x = P_x/N_x, \qquad \Delta y = P_y/N_y$$

N_x and N_y are the total number of subsections for the unit cell in x and y direction respectively. After the Fourier transforms, the rooftop basis functions in the spectral domain can be expressed as

$$\tilde{B}_{xmn}(\alpha,\beta) = \left[\frac{\sin(\alpha_{mn}\Delta x/2)}{\alpha_{mn}\Delta x/2}\right]^2 \frac{\sin(\beta\Delta y/2)}{\beta\Delta y/2}\, e^{-jm\alpha\Delta x} e^{-jn\beta\Delta y} \tag{2-21}$$

$$\tilde{B}_{ymn}(\alpha,\beta) = \frac{\sin(\alpha\Delta x/2)}{\alpha\Delta x/2}\left[\frac{\sin(\beta\Delta y/2)}{\beta\Delta y/2}\right]^2 e^{-jm\alpha\Delta x} e^{-jn\beta\Delta y} \tag{2-22}$$

However, the rooftop basis function can only handle the cases where the conductor current flows in the x or y direction. For the current flowing in slanting direction, it is unable to yield an accurate answer. For some arrays such as gangbuster and hexagon array, it needs to employ new basis function to simulate their frequency response accurately. Thus, the piecewise sinusoidal basis function is proposed to apply in such arrays. The piecewise sinusoidal basis function not only can solve the skewed or bent wire problem, but also can save more computational time compared to the rooftop basis function since the matrix size is reduced greatly.

An arbitrary bent thin wire is shown in Figure 2-3 where a bent wire is divided into $p+1$ segments. Every two adjacent segments form a bent dipole.

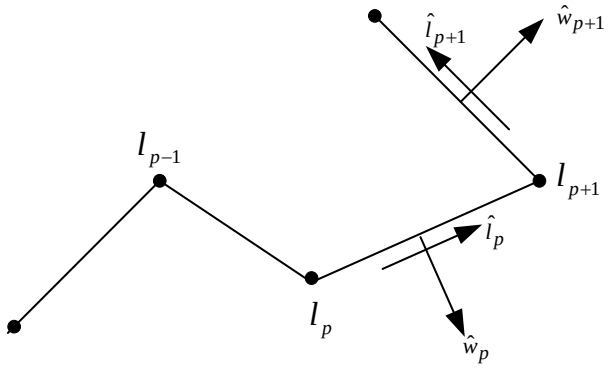

Figure 2-3 A bent thin wire

The current over the *pth* dipole is expressed as

$$J_p(\boldsymbol{\rho}) = \begin{cases} \hat{l}_p P_w(W) \dfrac{\sin k(l - l_{p-1})}{\sin k\Delta l_p} & l \in [l_{p-1}, l_p] \\ \hat{l}_{p+1} P_w(W) \dfrac{\sin k(l_{p+1} - l)}{\sin k\Delta l_{p+1}} & l \in [l_p, l_{p+1}] \end{cases} \tag{2-23}$$

Where k is the wave number of the medium which FSS screen is embedded in. $\Delta l_p = \left|\boldsymbol{\rho}_p - \boldsymbol{\rho}_{p-1}\right|$ and $\boldsymbol{\rho} = \hat{x}x + \hat{y}y$. l and W is the length and width of the wire respectively.

2.2.3 Spectral-domain Green's Function of Multi-layered FSS Structure

A multi-layered FSS structure embedded in N dielectric layers is shown in Figure 2-4.

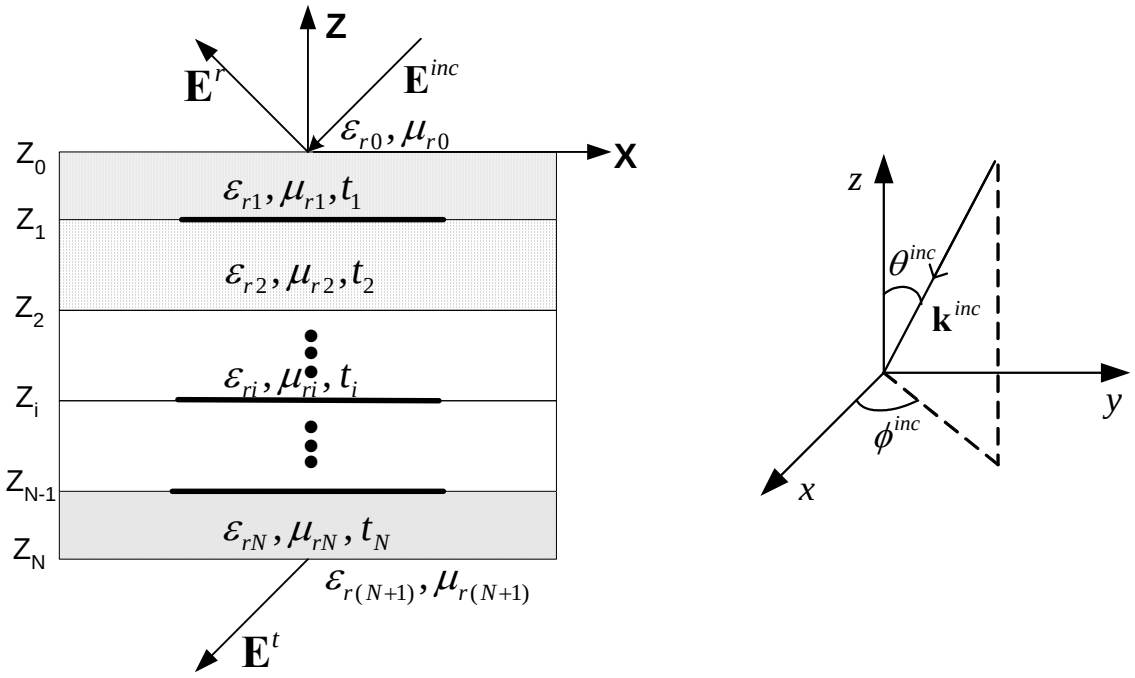

Figure 2-4 A multi-layered FSS structure embedded in N dielectric layers

ε_{ri}, μ_{ri} and t_i are the permittivity, the permeability and the thickness of the *ith* dielectric respectively. The spectral domain MoM technique in the freestanding FSS presented in Section 2.2.1 is still applicable. However, in (2-17), the spectral domain dyadic Green's function and the incident fields which induce surface current on FSS screens in the

presence of the dielectric structures have to be modified to account for a multi-screen FSS structure with multi-layered dielectrics.

The spectral Green's functions relating the current on the screen at the *jth* interface and the scattered field at the *ith* interface is derived. By the spectral-domain immittance approach, one gets

$$\begin{bmatrix} \tilde{G}_{xx}^{ij}(\alpha_{mn},\beta_{mn}) & \tilde{G}_{xy}^{ij}(\alpha_{mn},\beta_{mn}) \\ \tilde{G}_{yx}^{ij}(\alpha_{mn},\beta_{mn}) & \tilde{G}_{yy}^{ij}(\alpha_{mn},\beta_{mn}) \end{bmatrix} = \begin{bmatrix} \tilde{Z}^{TE,ij}\sin^2\phi_{mn} + \tilde{Z}^{TM,ij}\cos^2\phi_{mn} & (\tilde{Z}^{TM,ij} - \tilde{Z}^{TE,ij})\cos\phi_{mn}\sin\phi_{mn} \\ (\tilde{Z}^{TM,ij} - \tilde{Z}^{TE,ij})\cos\phi_{mn}\sin\phi_{mn} & \tilde{Z}^{TM,ij}\sin^2\phi_{mn} + \tilde{Z}^{TE,ij}\cos^2\phi_{mn} \end{bmatrix} \tag{2-24}$$

where

$$\cos\phi_{mn} = \alpha_{mn} \Big/ \sqrt{\alpha_{mn}^2 + \beta_{mn}^2}$$
$$\sin\phi_{mn} = \beta_{mn} \Big/ \sqrt{\alpha_{mn}^2 + \beta_{mn}^2} \tag{2-25}$$

For normal incidence ($\theta = 0$) and $\alpha_{00} = \beta_{00} = 0$ ($m = n = 0$), $\phi_{mn} = \phi^{inc}$. (2-24) can be rewritten as

$$\begin{bmatrix} \tilde{G}_{xx}^{ij}(\alpha_{00},\beta_{00}) & \tilde{G}_{xy}^{ij}(\alpha_{00},\beta_{00}) \\ \tilde{G}_{yx}^{ij}(\alpha_{00},\beta_{00}) & \tilde{G}_{yy}^{ij}(\alpha_{00},\beta_{00}) \end{bmatrix} = \begin{bmatrix} \tilde{Z}^{TE,ij}\sin^2\phi^{inc} + \tilde{Z}^{TM,ij}\cos^2\phi^{inc} & (\tilde{Z}^{TM,ij} - \tilde{Z}^{TE,ij})\cos\phi^{inc}\sin\phi^{inc} \\ (\tilde{Z}^{TM,ij} - \tilde{Z}^{TE,ij})\cos\phi^{inc}\sin\phi^{inc} & \tilde{Z}^{TM,ij}\sin^2\phi^{inc} + \tilde{Z}^{TE,ij}\cos^2\phi^{inc} \end{bmatrix} \tag{2-26}$$

Eq. (2-26) is different from the definition presented in Mittra and Chen's method [2-3]. θ is replaced by ϕ in our derivation. Thus, the multi-layered Green's function can be applicable at normal incidence.

In order to derive the Green's function, it is necessary to derive Z in (2-24). According to transmission line theory, the general equation for the input admittance is [3]

$$Y_{in} = Y_0 \frac{Y_0 + Y_L \coth \gamma t}{Y_0 \coth \gamma t + Y_L} \tag{2-27}$$

where Y_0 is the characteristic admittance of the medium and $\gamma = \sqrt{\alpha^2 + \beta^2 - \varepsilon_r \mu_r k_0^2}$. ε_r and μ_r are the permittivity and the permeability of dielectric respectively. t denotes the thickness of the medium. The transmission line equivalent model is depicted in Figure 2-5.

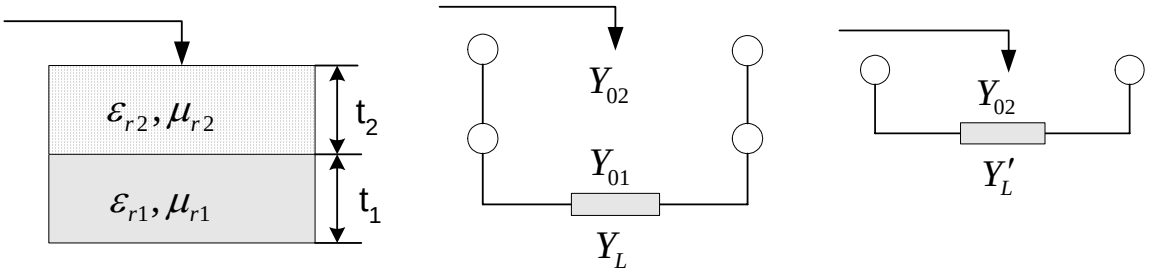

Figure 2-5 Equivalent transmission line model

By using of (2-27) successively, the input admittance looking downward is obtained

$$Y_{in} = Y_{02} \frac{Y_{02} + Y_{L'} \coth \gamma_2 t_2}{Y_{02} \coth \gamma_2 t_2 + Y_{L'}} \tag{2-28}$$

where

$$Y_{L'} = Y_{01} \frac{Y_{01} + Y_L \coth \gamma_1 t_1}{Y_{01} \coth \gamma_1 t_1 + Y_L}$$

$$\gamma_i = \sqrt{\alpha^2 + \beta^2 - \varepsilon_{ri} \mu_{ri} k_0^2} \tag{2-29}$$

The TE and TM case characteristic admittance of a medium are defined as follows

$$\begin{aligned} Y_0^{TE} &= -\gamma / j\omega\mu \\ Y_0^{TM} &= -j\omega\varepsilon/\gamma \end{aligned} \tag{2-30}$$

The input admittance looking upward can similarly be obtained. Therefore, the input impedance that relates the current on the screen at the jth interface and the scattered field at the same interface due to this current is then

$$Z^{TM/TE,jj} = 1/(Y_{bottom}^{TM/TE} + Y_{top}^{TM/TE}) \tag{2-31}$$

where Y_{bottom} and Y_{top} represent the input admittance looking downward and upward from the jth interface respectively.

On the other hand, when the scattered field is evaluated at a distance t away from the current source as depicted in Figure 2-6, it is necessary to modify (2-31) to obtain the impedance $Z^{TM/TE,(j-1)j}$. In Figure 2-6, Y_L^{j-1} is the input admittance looking upward from the top surface, that is, it includes all layers above the $(j-1)th$ interface. It is obtained by successively using (2-27).

To transfer the impedance to that at the $(j-1)th$ interface, one needs to multiply (2-31) by the factor

$$\begin{aligned} Y_{tran}^{(j-1)j} &= Y_{0j} \Big/ \left(Y_{0j} \cosh \gamma_j t_j + Y_{L(j-1)} \sinh \gamma_j t_j \right), \\ Y_{tran}^{(j+1)j} &= Y_{0(j+1)} \Big/ \left(Y_{0(j+1)} \cosh \gamma_{j+1} t_{j+1} + Y_{L(j+1)} \sinh \gamma_{j+1} t_{j+1} \right) \end{aligned} \tag{2-32}$$

Therefore

$$\begin{aligned} Z^{TM/TE,(j-1)j} &= Y_{tran}^{TM/TE,(j-1)j} Z^{TM/TE,jj} \\ Z^{TM/TE,(j+1)j} &= Y_{tran}^{TM/TE,(j+1)j} Z^{TM/TE,jj} \end{aligned} \tag{2-33}$$

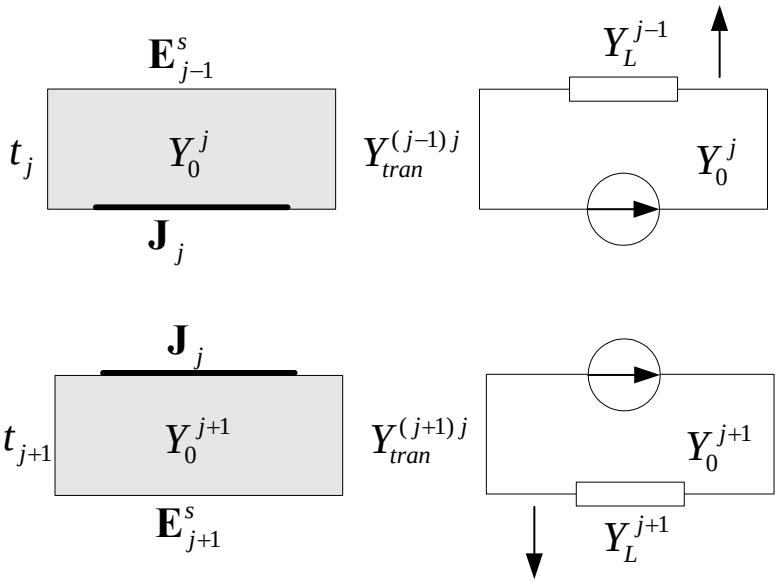

Figure 2-6 Relationship between the current and the scattered field at different location

By using (2-32) successively, one obtains the impedance $Z^{TM/TE,ij}$ as

$$Z^{TM/TE,ij} = Z^{TM/TE,jj} \cdot \begin{cases} \prod_{l=i+1}^{j} Y_{tran}^{TM/TE,(l-1)l} & i < j \\ \prod_{l=j}^{i-1} Y_{tran}^{TM/TE,(l+1)l} & i > j \end{cases} \tag{2-34}$$

Substituting (2-34) into (2-26), the spectral Green's functions relating the current on the FSS screen at the *jth* interface and the scattered field at the *ith* interface is obtained.

2.2.4 Excitation of Incident Electric Fields on FSS Screens

As mentioned before, for multi-screen FSS embedded in multi-layered mediums as shown in Figure 2-4, it is necessary to compute the incident electric field excitation on the FSS screen $\tilde{\mathbf{E}}^i$, where i denotes the layer position of FSS screens. The incident field is

calculated in the presence of the dielectric structures but with all FSS screens removed. In addition, the reflected electric field on the top interface $\tilde{\mathbf{E}}^r$ and the transmitted electric field on the bottom interface $\tilde{\mathbf{E}}^t$ can also be determined here.

In general, the incident wave is of both the parallel polarization (TM incidence) and perpendicular polarization (TE incidence) as shown in Figure 2-7.

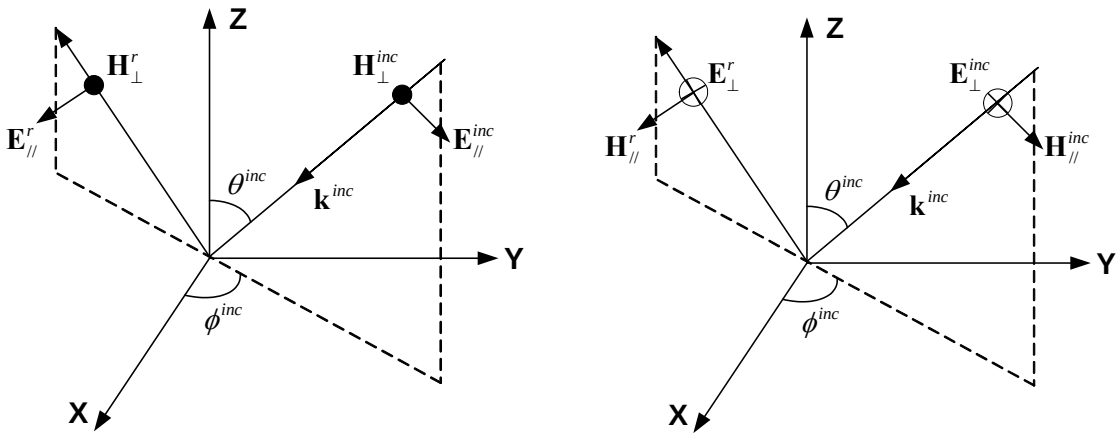

(a) (b)

Figure 2-7 Plane wave incidence (a) incident wave with parallel polarization (b) incident wave with perpendicular polarization

The incident wave propagation vector can be expressed as

$$\mathbf{k}^{inc} = -\hat{x}k_x^{inc} - \hat{y}k_y^{inc} - \hat{z}k_z^{inc} \tag{2-35}$$

Where

$$k_x^{inc} = k_0 \sin\theta^{inc} \cos\phi^{inc}, \quad k_y^{inc} = k_0 \sin\theta^{inc} \sin\phi^{inc}$$

$$\gamma_0 = \sqrt{\left(k_x^{inc}\right)^2 + \left(k_y^{inc}\right)^2 - k_0^{\,2}} = jk_0 \cos\theta^{inc}$$

$$k_z^{inc} = k_0 \cos\theta^{inc} = -j\gamma_0$$

If field intensity of the incident wave is expressed in spherical coordinate system, then the incident electric field $\tilde{\mathbf{E}}^{inc}$ can be resolved to $\tilde{\mathbf{E}}_{//}^{inc}$ in the parallel polarization incident wave and $\tilde{\mathbf{E}}_{\perp}^{inc}$ in the perpendicular polarization incident wave.

$$\tilde{\mathbf{E}}^{inc} = \tilde{\mathbf{E}}_{//}^{inc} + \tilde{\mathbf{E}}_{\perp}^{inc} \tag{2-36}$$

where

$$\begin{aligned} \tilde{\mathbf{E}}_{//}^{inc} &= \hat{\theta}^{inc} = \hat{x}\cos\theta^{inc} + \hat{y}\cos\theta^{inc}\sin\phi^{inc} - \hat{z}\sin\theta^{inc} \\ \tilde{\mathbf{E}}_{\perp}^{inc} &= \hat{\phi}^{inc} = -\hat{x}\sin\phi^{inc} + \hat{y}\cos\phi^{inc} \end{aligned} \tag{2-37}$$

Thus, unlike (2-35), the incident electric field is not vanished at normal incidence ($\theta = 0^0$). For incidence mode (m,n),

$$\begin{aligned} \hat{\theta}_{mn} &= \hat{x}\cos\theta_{mn}\cos\phi_{mn} + \hat{y}\cos\theta_{mn}\sin\phi_{mn} - \hat{z}\sin\theta_{mn} \\ \hat{\phi}_{mn} &= -\hat{x}\sin\phi_{mn} + \hat{y}\cos\phi_{mn} \end{aligned} \tag{2-38}$$

2.2.4.1 Incident Wave with Parallel Polarization (TM)

For incident wave with parallel polarization, the exciting electric field in each layer can be written as

$$\begin{aligned} \tilde{\mathbf{E}}_{//}^{0} &= \tilde{\mathbf{E}}_{//}^{inc} + \tilde{\mathbf{E}}_{//}^{r} = \hat{\theta}_d^0 e^{\gamma_{00}^0 z_0} + \hat{\theta}_u^0 R^{//} e^{-\gamma_{00}^0 z_0} \\ \tilde{\mathbf{E}}_{//}^{i} &= \hat{\theta}_d^i C_d^i e^{\gamma_{00}^i z_i} + \hat{\theta}_u^i C_u^i e^{-\gamma_{00}^i z_i} \\ \tilde{\mathbf{E}}_{//}^{N+1} &= \tilde{\mathbf{E}}_{//}^{t} = \hat{\theta}_d^{N+1} T^{//} e^{\gamma_{00}^{N+1} z_N} \end{aligned} \tag{2-39}$$

where $\hat{\theta}_d^i$ and $\hat{\theta}_u^i$ are the elevation unit vectors of the downward and upward waves in the *ith* layer respectively, C_d^i and C_u^i are the electric field coefficient of downward and upward waves in the *ith* layer respectively, and

$$\hat{\theta}_d^i = -\hat{\theta}_u^i = \hat{x}\cos\theta^i\cos\phi^{inc} + \hat{y}\cos\theta^i\sin\phi^{inc} \tag{2-40}$$

$$\cos\theta^i = \frac{\gamma_{00}^i}{jk^i}, \quad k^i = k_0\sqrt{\varepsilon_{ri}\mu_{ri}}, \quad \gamma_{00}^i = jk_0\sqrt{\varepsilon_{ri}\mu_{ri} - k_0^2\sin^2\theta^{inc}}$$

$$\tilde{\mathbf{E}}_{//}^{inc} = \left(\hat{x}\cos\phi^{inc} + \hat{y}\sin\phi^{inc}\right)\cos\theta^{inc}e^{\gamma_{00}^0 z_0} - \hat{z}\sin\theta^{inc}e^{\gamma_{00}^0 z_0} \tag{2-41}$$

$$\tilde{\mathbf{E}}_{//}^{r} = \left(-\hat{x}\cos\phi^{inc} + \hat{y}\sin\phi^{inc}\right)R^{//}\cos\theta^{inc}e^{-\gamma_{00}^0 z_0} - \hat{z}R^{//}\sin\theta^{inc}e^{-\gamma_{00}^0 z_0} \tag{2-42}$$

$$\tilde{\mathbf{E}}_{//}^{i} = \left(\hat{x}\cos\phi^{inc} + \hat{y}\sin\phi^{inc}\right)\frac{\gamma_{00}^i}{jk^i}\left(C_d^i e^{\gamma_{00}^i z_i} - C_u^i e^{-\gamma_{00}^i z_i}\right) - \hat{z}\left(C_d^i e^{\gamma_{00}^i z_i} + C_u^i e^{-\gamma_{00}^i z_i}\right)\sin\theta^i \tag{2-43}$$

$$\tilde{\mathbf{E}}_{//}^{t} = \left(\hat{x}\cos\phi^{inc} + \hat{y}\sin\phi^{inc}\right)T^{//}e^{\gamma_{00}^{N+1} z_N}\frac{\gamma_{00}^{N+1}}{jk^{N+1}} - \hat{z}T^{//}e^{\gamma_{00}^{N+1} z_N}\sin\theta^{inc} \tag{2-44}$$

From the time-harmonic Maxwell's equation

$$\mathbf{H} = \frac{1}{-j\omega\mu}\nabla\times\mathbf{E} = \frac{1}{\omega\mu}\mathbf{k}\times\mathbf{E} \tag{2-45}$$

The magnetic field in each dielectric layer can be expressed as

$$\begin{aligned}
\tilde{\mathbf{H}}_{\perp}^{0} &= -\hat{\phi}^{inc}\frac{k^0}{\omega\mu_0\mu_{r0}}\left(e^{\gamma_{00}^0 z_0} + R^{//}e^{-\gamma_{00}^0 z_0}\right) \\
\tilde{\mathbf{H}}_{\perp}^{i} &= -\hat{\phi}^{inc}\frac{k^i}{\omega\mu_0\mu_{ri}}\left(C_d^i e^{\gamma_{00}^i z_i} + C_u^i e^{-\gamma_{00}^i z_i}\right) \\
\tilde{\mathbf{H}}_{\perp}^{N+1} &= -\hat{\phi}^{inc}\frac{k^{N+1}}{\omega\mu_0\mu_{r(N+1)}}T^{//}e^{\gamma_{00}^{N+1} z_N}
\end{aligned} \tag{2-46}$$

The tangential components of the electric fields and magnetic fields between the two adjacent layers are equal (the boundary conditions). Therefore, we have

$$\begin{aligned}\hat{\rho}^{inc}\cdot\tilde{\mathbf{E}}^{i}_{//}&=\hat{\rho}^{inc}\cdot\tilde{\mathbf{E}}^{i+1}_{//},\quad 0\le i\le N\\ \hat{\phi}^{inc}\cdot\tilde{\mathbf{H}}^{i}_{\perp}&=\hat{\phi}^{inc}\cdot\tilde{\mathbf{H}}^{i+1}_{\perp},\quad 0\le i\le N\end{aligned}\tag{2-47}$$

where

$$\hat{\rho}^{inc}\cdot=\hat{x}\cos\phi^{inc}+\hat{y}\sin\phi^{inc}$$

Substitute (2-39) and (2-46) into (2-47), we obtain

$$\begin{aligned}&\frac{\gamma_{00}^{0}}{k^{0}}\left(e^{\gamma_{00}^{0}z_0}-R^{//}e^{-\gamma_{00}^{0}z_0}\right)=\frac{\gamma_{00}^{1}}{k^{1}}\left(C_d^1e^{\gamma_{00}^{1}z_0}-C_u^1e^{-\gamma_{00}^{1}z_0}\right)\\ &\frac{k^{0}}{\mu_{r0}}\left(e^{\gamma_{00}^{0}z_0}+R^{//}e^{-\gamma_{00}^{0}z_0}\right)=\frac{k^{1}}{\mu_{r1}}\left(C_d^1e^{\gamma_{00}^{1}z_0}+C_u^1e^{-\gamma_{00}^{1}z_0}\right)\\ &\frac{\gamma_{00}^{i}}{k^{i}}\left(C_d^ie^{\gamma_{00}^{i}z_i}-C_u^ie^{-\gamma_{00}^{i}z_i}\right)=\frac{\gamma_{00}^{i+1}}{k^{i+1}}\left(C_d^{i+1}e^{\gamma_{00}^{i+1}z_i}-C_u^{i+1}e^{-\gamma_{00}^{i+1}z_i}\right)\\ &\frac{k^{i}}{\mu_{ri}}\left(C_d^ie^{\gamma_{00}^{i}z_i}+C_u^ie^{-\gamma_{00}^{i}z_i}\right)=\frac{k^{i+1}}{\mu_{r(i+1)}}\left(C_d^{i+1}e^{\gamma_{00}^{i+1}z_i}+C_u^{i+1}e^{-\gamma_{00}^{i+1}z_i}\right)\\ &\frac{\gamma_{00}^{N}}{k^{N}}\left(C_d^Ne^{\gamma_{00}^{N}z_N}-C_u^Ne^{-\gamma_{00}^{N}z_N}\right)=\frac{\gamma_{00}^{N+1}}{k^{N+1}}T^{//}e^{\gamma_{00}^{N+1}z_N}\\ &\frac{k^{N}}{\mu_{rN}}\left(C_d^Ne^{\gamma_{00}^{N}z_N}+C_u^Ne^{-\gamma_{00}^{N}z_N}\right)=\frac{k^{N+1}}{\mu_{r(N+1)}}T^{//}e^{\gamma_{00}^{N+1}z_N}\end{aligned}\tag{2-48}$$

All the coefficients in (2-48) can be determined numerically through a matrix equation

$$\mathbf{A}_{//}=\mathbf{x}_{//}\cdot\mathbf{b}_{//}\tag{2-49}$$

where

$$\mathbf{x}_{//}=\begin{bmatrix}R^{//} & C_d^1 & C_u^1 & \cdots & C_d^N & C_u^N & T^{//}\end{bmatrix}^T$$

$$\mathbf{b}_{//}=\begin{bmatrix}-\frac{\gamma_{00}^{0}}{k^{0}}e^{\gamma_{00}^{0}z_0} & -\frac{k^{0}}{\mu_{r0}}e^{\gamma_{00}^{0}z_0} & 0 & \cdots & 0\end{bmatrix}^T$$

$$A_{11}=-\frac{\gamma_{00}^{0}}{k^{0}}e^{-\gamma_{00}^{0}z_0},\ A_{12}=-\frac{\gamma_{00}^{1}}{k^{1}}e^{\gamma_{00}^{1}z_0},\ A_{13}=\frac{\gamma_{00}^{1}}{k^{1}}e^{-\gamma_{00}^{1}z_0}$$

$$A_{21}=\frac{k^{0}}{\mu_{r0}}e^{-\gamma_{00}^{0}z_0},\ A_{22}=-\frac{k^{1}}{\mu_{r1}}e^{\gamma_{00}^{1}z_0},\ A_{23}=-\frac{k^{1}}{\mu_{r1}}e^{-\gamma_{00}^{1}z_0}$$

$$A_{2i+1,2i} = \frac{\gamma_{00}^i}{k^i} e^{\gamma_{00}^i z_i}, \qquad A_{2i+1,2i+1} = -\frac{\gamma_{00}^i}{k^i} e^{-\gamma_{00}^i z_i},$$

$$A_{2i+1,2i+2} = -\frac{\gamma_{00}^{i+1}}{k^{i+1}} e^{\gamma_{00}^{i+1} z_i}, \quad A_{2i+1,2i+3} = \frac{\gamma_{00}^{i+1}}{k^{i+1}} e^{-\gamma_{00}^{i+1} z_i}$$

$$A_{2i+2,2i} = \frac{k^i}{\mu_r^i} e^{\gamma_{00}^i z_i}, \qquad A_{2i+2,2i+1} = \frac{k^i}{\mu_r^i} e^{-\gamma_{00}^i z_i}$$

$$A_{2i+2,2i+2} = -\frac{k^{i+1}}{\mu_r^{i+1}} e^{\gamma_{00}^{i+1} z_i}, \quad A_{2i+2,2i+3} = -\frac{k^{i+1}}{\mu_r^{i+1}} e^{-\gamma_{00}^{i+1} z_i}$$

$$A_{2N+1,2N} = \frac{\gamma_{00}^N}{k^N} e^{\gamma_{00}^N z_N}, \quad A_{2N+1,2N+1} = -\frac{\gamma_{00}^N}{k^N} e^{-\gamma_{00}^N z_N}, \quad A_{2N+1,2N+2} = -\frac{\gamma_{00}^{N+1}}{k^{N+1}} e^{\gamma_{00}^{N+1} z_N}$$

$$A_{2N+2,2N} = \frac{k^N}{\mu_{rN}} e^{\gamma_{00}^N z_N}, \quad A_{2N+2,2N+1} = \frac{k^N}{\mu_{rN}} e^{-\gamma_{00}^N z_N}, \quad A_{2N+2,2N+2} = -\frac{k^{N+1}}{\mu_{r(N+1)}} e^{\gamma_{00}^{N+1} z_N}$$

2.2.4.2 Incident Wave with Perpendicular Polarization (TE)

For incident wave with perpendicular polarization, the exciting magnetic fields in each layer is written as

$$\begin{aligned}
\tilde{\mathbf{H}}_{//}^0 &= \frac{1}{\eta_0}\left(\hat{\theta}_d^0 e^{\gamma_{00}^0 z_0} + \hat{\theta}_u^0 R^{\perp} e^{-\gamma_{00}^0 z_0}\right) \\
\tilde{\mathbf{H}}_{//}^i &= \frac{1}{\eta_0}\left(\hat{\theta}_d^i C_d^i e^{\gamma_{00}^i z_i} + \hat{\theta}_u^i C_u^i e^{-\gamma_{00}^i z_i}\right) \\
\tilde{\mathbf{H}}_{//}^{N+1} &= \frac{1}{\eta_0}\hat{\theta}_d^{N+1} T^{\perp} e^{\gamma_{00}^{N+1} z_N}
\end{aligned} \tag{2-50}$$

From the time-harmonic Maxwell's equation

$$\mathbf{E} = \frac{1}{j\omega\varepsilon}\nabla \times \mathbf{H} = \frac{-1}{\omega\varepsilon}\mathbf{k} \times \mathbf{H} \tag{2-51}$$

The exciting electric field in each layer is obtained as

$$\begin{aligned}
\tilde{\mathbf{E}}_{\perp}^{0} &= \tilde{\mathbf{E}}_{\perp}^{inc} + \tilde{\mathbf{E}}_{\perp}^{r} = \hat{\phi}^{inc}\left(e^{\gamma_{00}^{0} z_0} + R^{\perp} e^{-\gamma_{00}^{0} z_0}\right) \\
\tilde{\mathbf{E}}_{\perp}^{i} &= \hat{\phi}^{inc}\frac{1}{\eta_0}\frac{k^i}{\omega\varepsilon_0\varepsilon_{ri}}\left(C_d^i e^{\gamma_{00}^{i} z_i} + C_u^i e^{-\gamma_{00}^{i} z_i}\right) \\
\tilde{\mathbf{E}}_{\perp}^{N+1} &= \tilde{\mathbf{E}}_{\perp}^{t} = \hat{\phi}^{inc}\frac{1}{\eta_0}\frac{k^{N+1}}{\omega\varepsilon_0\varepsilon_{r(N+1)}} T^{\perp} e^{\gamma_{00}^{N+1} z_N}
\end{aligned} \tag{2-52}$$

where $\eta_0 = 120\pi$

$$\tilde{\mathbf{E}}_{\perp}^{inc} = \left(-\hat{x}\sin\phi^{inc} + \hat{y}\cos\phi^{inc}\right) e^{\gamma_{00}^{0} z_0} \tag{2-53}$$

$$\tilde{\mathbf{E}}_{\perp}^{r} = \left(-\hat{x}\sin\phi^{inc} + \hat{y}\cos\phi^{inc}\right) R^{\perp} e^{-\gamma_{00}^{0} z_0} \tag{2-54}$$

$$\tilde{\mathbf{E}}_{\perp}^{i} = \left(-\hat{x}\sin\phi^{inc} + \hat{y}\cos\phi^{inc}\right)\frac{1}{\eta_0}\frac{k^i}{\omega\varepsilon_0\varepsilon_{ri}}\left(C_d^i e^{\gamma_{00}^{i} z_i} + C_u^i e^{-\gamma_{00}^{i} z_i}\right) \tag{2-55}$$

$$\tilde{\mathbf{E}}_{\perp}^{t} = \left(-\hat{x}\sin\phi^{inc} + \hat{y}\cos\phi^{inc}\right)\frac{1}{\eta_0}\frac{k^{N+1}}{\omega\varepsilon_0\varepsilon_{r(N+1)}} T^{\perp} e^{\gamma_{00}^{N+1} z_N} \tag{2-56}$$

Similar to incident wave with parallel polarization, applying the boundary conditions

$$\begin{aligned}
\hat{\rho}^{inc}\cdot\tilde{\mathbf{H}}_{//}^{i} &= \hat{\rho}^{inc}\cdot\tilde{\mathbf{H}}_{//}^{i+1} \quad 0 \le i \le N \\
\hat{\phi}^{inc}\cdot\tilde{\mathbf{E}}_{\perp}^{i} &= \hat{\phi}^{inc}\cdot\tilde{\mathbf{E}}_{\perp}^{i+1} \quad 0 \le i \le N
\end{aligned} \tag{2-57}$$

and substituting (2-50) and (2-52) into (2-57), we get

$$\begin{aligned}
&\frac{\gamma_{00}^{0}}{k^0}\left(e^{\gamma_{00}^{0} z_0} - R^{\perp} e^{-\gamma_{00}^{0} z_0}\right) = \frac{\gamma_{00}^{1}}{k^1}\left(C_d^1 e^{\gamma_{00}^{1} z_0} - C_u^1 e^{-\gamma_{00}^{1} z_0}\right) \\
&\frac{k^0}{\varepsilon_{r0}}\left(e^{\gamma_{00}^{0} z_0} + R^{\perp} e^{-\gamma_{00}^{0} z_0}\right) = \frac{k^1}{\varepsilon_{r1}}\left(C_d^1 e^{\gamma_{00}^{1} z_0} + C_u^1 e^{-\gamma_{00}^{1} z_0}\right) \\
&\frac{\gamma_{00}^{i}}{k^i}\left(C_d^i e^{\gamma_{00}^{i} z_i} - C_u^i e^{-\gamma_{00}^{i} z_i}\right) = \frac{\gamma_{00}^{i+1}}{k^{i+1}}\left(C_d^{i+1} e^{\gamma_{00}^{i+1} z_i} - C_u^{i+1} e^{-\gamma_{00}^{i+1} z_i}\right) \\
&\frac{k^i}{\varepsilon_{ri}}\left(C_d^i e^{\gamma_{00}^{i} z_i} + C_u^i e^{-\gamma_{00}^{i} z_i}\right) = \frac{k^{i+1}}{\varepsilon_{r(i+1)}}\left(C_d^{i+1} e^{\gamma_{00}^{i+1} z_i} + C_u^{i+1} e^{-\gamma_{00}^{i+1} z_i}\right) \\
&\frac{\gamma_{00}^{N}}{k^N}\left(C_d^N e^{\gamma_{00}^{N} z_N} - C_u^N e^{-\gamma_{00}^{N} z_N}\right) = \frac{\gamma_{00}^{N+1}}{k^{N+1}} T^{\perp} e^{\gamma_{00}^{N+1} z_N} \\
&\frac{k^N}{\varepsilon_{rN}}\left(C_d^N e^{\gamma_{00}^{N} z_N} + C_u^N e^{-\gamma_{00}^{N} z_N}\right) = \frac{k^{N+1}}{\varepsilon_{r(N+1)}} T^{\perp} e^{\gamma_{00}^{N+1} z_N}
\end{aligned} \tag{2-58}$$

Therefore, it is possible to unify (2-49) by defining

$$\xi_i = \begin{cases} \mu_{ri} & \text{incident wave with parallel polarization} \\ \varepsilon_{ri} & \text{incident wave with perpendicular polarization} \end{cases} \tag{2-59}$$

Hence, the coefficients in (2-52) can also be solved through matrix equations.

The incident field exciting on FSS screen $\tilde{\mathbf{E}}^i_{//}$ and $\tilde{\mathbf{E}}^i_{\perp}$, the reflected field on the top interface $\tilde{\mathbf{E}}^r_{//}$ and $\tilde{\mathbf{E}}^r_{\perp}$, and the transmitted field on the bottom interface $\tilde{\mathbf{E}}^t_{//}$ and $\tilde{\mathbf{E}}^t_{\perp}$ can also be determined according to (2-41)-(2-44) and (2-53)-(2-56) after vector $[\mathbf{x}]$ is solved.

2.2.5 Reflection and Transmission Coefficients

Similar to the incident electric field, the reflected electric field of mode (m,n) can also be decomposed into components of parallel and perpendicular polarization.

$$\tilde{\mathbf{E}}^r_{mn} = \left(\tilde{\mathbf{E}}^r_{mn}\right)_{//} + \left(\tilde{\mathbf{E}}^r_{mn}\right)_{\perp} = \hat{\theta}^r_{mn} R^{//}_{mn} + \hat{\phi}^r_{mn} R^{\perp}_{mn} \tag{2-60}$$

where

$$\begin{aligned} \hat{\theta}^r_{mn} &= \hat{x}\cos\theta^r_{mn}\cos\phi^r_{mn} + \hat{y}\cos\theta^r_{mn}\sin\phi^r_{mn} - \hat{z}\sin\theta^r_{mn} \\ \hat{\phi}^r_{mn} &= -\hat{x}\sin\phi^r_{mn} + \hat{y}\cos\phi^r_{mn} \end{aligned} \tag{2-61}$$

$$\theta^r_{mn} = \theta_{mn}, \quad \phi^r_{mn} = \phi_{mn} + \pi \tag{2-62}$$

The reflection coefficient with perpendicular polarization can be computed directly from

$$R^{\perp}_{mn} = -\tilde{\mathbf{E}}^r_{mn} \cdot \hat{\phi}^r_{mn} = -\left(\tilde{\mathbf{E}}^r_{mn}\right)_x \sin\phi_{mn} + \left(\tilde{\mathbf{E}}^r_{mn}\right)_y \cos\phi_{mn} \tag{2-63}$$

where the total reflected fields $\tilde{\mathbf{E}}^r_{mn}$ can be obtained from the summation of scattered field in eq. (2-18) and reflected excitation field in parallel or perpendicular incidence (eq. (2-

41) or eq. (2-53)). In (2-60), the perpendicular polarization component of the reflection electric field is

$$\left(\tilde{\mathbf{E}}_{mn}^{r}\right)_{\perp} = -\hat{\phi}_{mn}^{r} R_{mn}^{\perp} = R_{mn}^{\perp}\left(\hat{x}\sin\phi_{mn}^{r} - \hat{y}\cos\phi_{mn}^{r}\right) = -R_{mn}^{\perp}\left(\hat{x}\sin\phi_{mn} - \hat{y}\cos\phi_{mn}\right) \tag{2-64}$$

$$\begin{cases} \left(\tilde{\mathbf{E}}_{mn}^{r}\right)_{\perp}^{x} = -R_{mn}^{\perp}\sin\phi_{mn} \\ \left(\tilde{\mathbf{E}}_{mn}^{r}\right)_{\perp}^{y} = R_{mn}^{\perp}\cos\phi_{mn} \end{cases} \tag{2-65}$$

$$\begin{cases} \left(\tilde{\mathbf{E}}_{mn}^{r}\right)_{//}^{x} = \tilde{\mathbf{E}}_{mn}^{r} - \left(\tilde{\mathbf{E}}_{mn}^{r}\right)_{\perp}^{x} \\ \left(\tilde{\mathbf{E}}_{mn}^{r}\right)_{//}^{y} = \tilde{\mathbf{E}}_{mn}^{r} - \left(\tilde{\mathbf{E}}_{mn}^{r}\right)_{\perp}^{y} \end{cases} \tag{2-66}$$

The component parallel to the plane of reflection in mode (m,n) is expressed as

$$\begin{aligned} \left(\tilde{\mathbf{E}}_{mn}^{r}\right)_{//} &= \hat{\theta}_{mn}^{r} R_{mn}^{//} = R_{mn}^{//}\left(\hat{x}\cos\theta_{mn}^{r}\cos\phi_{mn}^{r} + \hat{y}\cos\theta_{mn}^{r}\sin\phi_{mn}^{r} - \hat{z}\sin\theta_{mn}^{r}\right) \\ &= -R_{mn}^{//}\cos\theta_{mn}\left(\hat{x}\cos\phi_{mn} + \hat{y}\sin\phi_{mn}\right) - \hat{z}R_{mn}^{//}\sin\theta_{mn} \end{aligned} \tag{2-67}$$

where

$$\cos\theta_{mn} = \gamma_{mn}/jk_0, \qquad \gamma_{mn} = \sqrt{\alpha_{mn}^2 + \beta_{mn}^2 - k_0^2}\,.$$

From (2-67), we can get

$$\begin{cases} \left(\tilde{\mathbf{E}}_{mn}^{r}\right)_{//}^{x} = -R_{mn}^{//}\cos\theta_{mn}\cos\phi_{mn} \\ \left(\tilde{\mathbf{E}}_{mn}^{r}\right)_{//}^{y} = -R_{mn}^{//}\cos\theta_{mn}\sin\phi_{mn} \end{cases} \tag{2-68}$$

The reflection coefficients with parallel polarization can then be derived as

$$R_{mn}^{//} = -\frac{\left(\tilde{\mathbf{E}}_{mn}^{r}\right)_{//}^{x}\cos\phi_{mn} + \left(\tilde{\mathbf{E}}_{mn}^{r}\right)_{//}^{y}\sin\phi_{mn}}{\cos\theta_{mn}} = -\frac{\left(\tilde{\mathbf{E}}_{mn}^{r}\right)_{//}^{x}\cos\phi_{mn} + \left(\tilde{\mathbf{E}}_{mn}^{r}\right)_{//}^{y}\sin\phi_{mn}}{\gamma_{mn}/jk_0} \tag{2-69}$$

The transmitted electric field can be written as the summation of parallel polarization component and perpendicular polarization component.

$$\tilde{\mathbf{E}}^t_{mn} = \left(\tilde{\mathbf{E}}^t_{mn}\right)_{//} + \left(\tilde{\mathbf{E}}^t_{mn}\right)_{\perp} = \hat{\theta}^t_{mn} T^{//}_{mn} + \hat{\phi}^t_{mn} T^{\perp}_{mn} \tag{2-70}$$

where

$$\begin{aligned} \hat{\theta}^t_{mn} &= \hat{x}\cos\theta^t_{mn}\cos\phi^t_{mn} + \hat{y}\cos\theta^t_{mn}\sin\phi^t_{mn} - \hat{z}\sin\theta^t_{mn} \\ \hat{\phi}^t_{mn} &= -\hat{x}\sin\phi^t_{mn} + \hat{y}\cos\phi^t_{mn} \end{aligned} \tag{2-71}$$

$$\theta^t_{mn} = \theta_{mn}\,,\ \phi^t_{mn} = \phi_{mn} \tag{2-72}$$

The transmission coefficient with perpendicular polarization can be computed directly according to

$$T^{\perp}_{mn} = \tilde{\mathbf{E}}^t_{mn} \cdot \hat{\phi}^t_{mn} = -\left(\tilde{\mathbf{E}}^t_{mn}\right)_x \sin\phi_{mn} + \left(\tilde{\mathbf{E}}^t_{mn}\right)_y \cos\phi_{mn} \tag{2-73}$$

Where $\tilde{\mathbf{E}}^t_{mn}$ is the summation of scattered field in eq. (2-18) and transmitted field in parallel or perpendicular incidence (eq.(2-44) or eq. (2-56)).

In (2-70), the perpendicular incidence component of transmitted field is

$$\left(\tilde{\mathbf{E}}^t_{mn}\right)_{\perp} = \hat{\phi}^t_{mn} T^{\perp}_{mn} = T^{\perp}_{mn}\left(-\hat{x}\sin\phi^t_{mn} + \hat{y}\cos\phi^t_{mn}\right) \tag{2-74}$$

Accordingly

$$\begin{cases} \left(\tilde{\mathbf{E}}^t_{mn}\right)^x_{//} = \tilde{\mathbf{E}}^t_{mn} - \left(\tilde{\mathbf{E}}^t_{mn}\right)^x_{\perp} \\ \left(\tilde{\mathbf{E}}^t_{mn}\right)^y_{//} = \tilde{\mathbf{E}}^t_{mn} - \left(\tilde{\mathbf{E}}^t_{mn}\right)^y_{\perp} \end{cases} \tag{2-75}$$

In (2-70), the parallel polarization component of transmitted field can be expressed as

$$\begin{aligned} \left(\tilde{\mathbf{E}}^t_{mn}\right)_{//} &= \hat{\theta}^t_{mn} T^{//}_{mn} = T^{//}_{mn}\left(\hat{x}\cos\theta^t_{mn}\cos\phi^t_{mn} + \hat{y}\cos\theta^t_{mn}\sin\phi^t_{mn} - \hat{z}\sin\theta^t_{mn}\right) \\ &= T^{//}_{mn}\cos\theta_{mn}\left(\hat{x}\cos\phi_{mn} + \hat{y}\sin\phi_{mn}\right) - \hat{z}T^{//}_{mn}\sin\theta_{mn} \end{aligned} \tag{2-76}$$

$$\begin{aligned} \left(\tilde{\mathbf{E}}^t_{mn}\right)^x_{//} &= T^{//}_{mn}\cos\theta_{mn}\cos\phi_{mn} \\ \left(\tilde{\mathbf{E}}^t_{mn}\right)^y_{//} &= T^{//}_{mn}\cos\theta_{mn}\sin\phi_{mn} \end{aligned} \tag{2-77}$$

The transmission coefficient with parallel polarization can then be derived as

$$T_{mn}^{//} = \frac{\left(\tilde{\mathbf{E}}_{mn}^{t}\right)_{//}^{x}\cos\phi_{mn} + \left(\tilde{\mathbf{E}}_{mn}^{t}\right)_{//}^{y}\sin\phi_{mn}}{\cos\theta_{mn}} = \frac{\left(\tilde{\mathbf{E}}_{mn}^{t}\right)_{//}^{x}\cos\phi_{mn} + \left(\tilde{\mathbf{E}}_{mn}^{t}\right)_{//}^{y}\sin\phi_{mn}}{\gamma_{mn}/jk_0} \tag{2-78}$$

For mode 00, $\theta_{mn} = \theta_{00} = \theta^{inc}$, $\phi_{mn} = \phi_{00} = \phi^{inc}$, therefore, (2-63), (2-69), (2-73) and (2-78) can be re-written as

$$R_{00}^{\perp} = -\left(\tilde{\mathbf{E}}_{00}^{r}\right)_x \sin\phi^{inc} + \left(\tilde{\mathbf{E}}_{00}^{r}\right)_y \cos\phi^{inc} \tag{2-79}$$

$$R_{00}^{//} = -\frac{\left(\tilde{\mathbf{E}}_{00}^{r}\right)_{//}^{x}\cos\phi^{inc} + \left(\tilde{\mathbf{E}}_{00}^{r}\right)_{//}^{y}\sin\phi^{inc}}{\gamma_{00}/jk_0} \tag{2-80}$$

$$T_{00}^{\perp} = -\left(\tilde{\mathbf{E}}_{00}^{t}\right)_x \sin\phi^{inc} + \left(\tilde{\mathbf{E}}_{00}^{t}\right)_y \cos\phi^{inc} \tag{2-81}$$

$$T_{00}^{//} = \frac{\left(\tilde{\mathbf{E}}_{00}^{t}\right)_{//}^{x}\cos\phi^{inc} + \left(\tilde{\mathbf{E}}_{00}^{t}\right)_{//}^{y}\sin\phi^{inc}}{\gamma_{00}/jk_0} \tag{2-82}$$

2.3 Analysis of FSS using Equivalent Circuit Model (ECM)

The ECM technique was first applied to FSS by Anderson [46]. The empirical model is based partly on an extension of expressions for reactance developed by Marcuvitz [47] and Wait [48]. The equivalent circuit parameter expressions were derived by Marcuvitz for infinite strip gratings and supplemented by Archer [49] to give complete modeling equations. The basic circuit modeling expressions, presented by Marcuvitz, can only be applied at oblique angles of incidence to an inductive component illuminated by a TE incident wave or a capacitive component illuminated by a TM incident wave. Archer derived modified equations for the two other cases i.e., inductive TM incidence and

capacitive TE incidence. He obtained explicit expressions for the normalized wave reactance of inductive strip gratings in TE and TM incident waves. Langley and Parker [31, 50] successfully used the approach to analyze arrays of single squares and double squares at normal incidence. Lee and Langley [13, 32, 51] applied the modified equations derived from Archer in terms of first order coefficients for the correction term in equivalent circuit model to compute the transmission characteristics of the strips at oblique angles of incidence in all planes. Such geometries include double-square, gridded-square and gridded-double-square elements.

In the ECM model, the interaction of incident waves with an infinite periodic array of elements is represented as a wave traveling down a transmission line, with shunt lumped circuit impedances representing the array. For an infinite array of thin, continuous, perfectly conducting narrow strips the shunt impedance is either inductive or capacitive, depending on whether the incident wave is polarized parallel or perpendicular to the strips. The circuit models of the FSS are determined in terms of the geometries of the FSS elements where inductive and capacitive circuit components can be identified. From the solution of circuit, the transmission coefficients of the FSS screen are determined.

The ECM is unable to model the effects of the dielectric substrate and superstrate accurately since this approach uses the quasi-static approximation to calculate the circuit components. Furthermore, the method is less accurate at higher frequencies, particularly in the grating lobe region. The equivalent circuit components are valid for wavelength λ and angles of incidence θ in the range $\lambda > p(1+\sin\theta)$, where p is the periodicity between elements. However, this method is a useful analytical tool in the design of FSS

since it is able to provide frequency response of a FSS with very short-computational time once the required geometrical parameters are determined.

2.3.1 Formulations of ECM

As mentioned before, the ECM technique represents the FSS by an equivalent circuit. The values of inductances L and capacitances C can be determined from a modification of the strip array formulas developed by Marcuvitz and Wait. Figure 2-8 shows a plane wave incident on an inductive strip grating, where P is the periodicity of the conductors, w is the width of the strip, g is the distance between two strips and θ and ϕ are the incident angles.

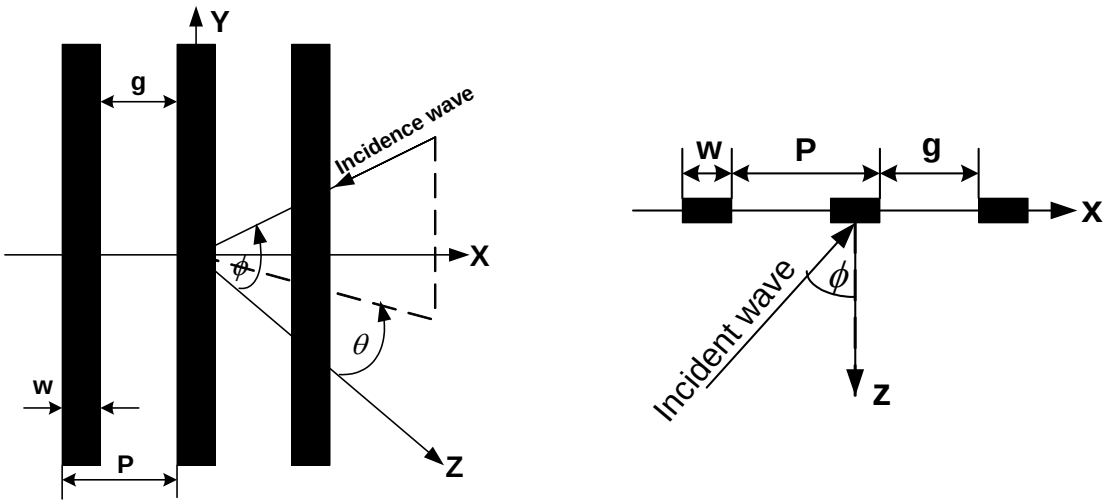

(a) (b)

Figure 2-8 A plane wave incident on an inductive strip grating (a) Front view (b) Side view

The normalized inductances or capacitances of the strip grating immittances expressions of TE incidence for inductance X_{TE} and capacitance B_{TE} and TM incidence for inductance X_{TM} and capacitance B_{TM} take the form [13, 31-32].

$$X_{TE} = \omega L_{TE} = F(p,w,\lambda) = \frac{p\cos\theta}{\lambda}\left[\ln\cos ec\left(\frac{\pi w}{2p}\right) + G(p,w,\lambda,\theta)\right] \tag{2-83}$$

$$B_{TE} = \omega C_{TE} = \frac{4p\sec\theta}{\lambda}\left[\ln\cos ec\left(\frac{\pi g}{2p}\right) + G(p,g,\lambda,\theta)\right] \tag{2-84}$$

$$X_{TM} = \omega L_{TM} = \frac{p\sec\phi}{\lambda}\left[\ln\cos ec\left(\frac{\pi w}{2p}\right) + G(p,w,\lambda,\phi)\right] \tag{2-85}$$

$$B_{TM} = \omega C_{TM} = 4F(p,g,\lambda) = \frac{4p\cos\phi}{\lambda}\left[\ln\cos ec\left(\frac{\pi g}{2p}\right) + G(p,g,\lambda,\phi)\right] \tag{2-86}$$

where λ is the wavelength, and the correction term $G(p, \frac{w}{g}, \lambda, \frac{\theta}{\phi})$ is given as

$$G(p,\frac{w}{g},\lambda,\frac{\theta}{\phi}) = \frac{0.5(1-\beta^2)^2\left[\left(1-\frac{\beta^2}{4}\right)(C_+ + C_-) + 4\beta^2 C_+ C_-\right]}{\left(1-\frac{\beta^2}{4}\right) + \beta^2\left(1+\frac{\beta^2}{2}-\frac{\beta^4}{8}\right)(C_+ + C_-) + 2\beta^6 C_+ C_-} \tag{2-87}$$

where

$$\beta = \sin\left(\pi \frac{w}{g} \Big/ 2p\right)$$

$$C_\pm = \frac{1}{\sqrt{\left(\frac{p\sin\theta}{\lambda} \pm 1\right)^2 - \frac{p^2}{\lambda^2}}} - 1 \qquad \text{in } G(p,w,\lambda,\theta) \text{ and } G(p,g,\lambda,\phi) \tag{2-88}$$

$$C_\pm = \frac{1}{\sqrt{1-\left(\frac{p\cos\phi}{\lambda}\right)^2}} - 1 \qquad \text{in } G(p,g,\lambda,\theta) \text{ and } G(p,w,\lambda,\phi) \tag{2-89}$$

The normalized admittance Y of an array at oblique incidence can be calculated according to the equivalent circuit. The transmission coefficient T of the array is determined from

$$|T|^2 = \frac{4}{4+|Y|^2} \tag{2-90}$$

The effect of the supporting substrate is included in simple equivalent circuit models by incorporating an effective dielectric constant ε_{reff} in the calculation of susceptances [31]. Equivalent circuit model for FSS elements have been derived for double-square [13, 32, 50], gridded-square [13, 32, 51], gridded-double-square [12-13], Jerusalem crosses [52], gridded Jerusalem cross [53-54], and superdense linear dipole [55]. For double-square, gridded-square and gridded-double-square elements, the accuracy of the models had been validated by experimental results [12-13, 31-32, 50-51].

2.4 Conclusions

In this chapter, two numerical methods for the analysis of FSS, spectral-domain MoM and ECM are introduced. These methods have been applied to analyze the frequency response of FSS screen in the design of FSS, which are presented in the chapter 4 and 5.

Our improved spectral-domain MoM presented in Section 2.2 provides the accurate analysis about complicated FSS structures. The most prominent advantage of the improved method is that it can handle normal incidence. The formulas derived in section 2.2.4 and 2.2.5 are different from those presented by Mittra and Chan. Some revisions for the derivation of multi-layered Green's function are implemented (section 2.2.3). The

expressions for the transmission & reflection coefficient are derived based on electric field instead of previous vector electric potentials (section 2.2.5). Furthermore, the incident electric field is expressed in spherical coordinate system so that the expression of incident field do not equal to zero at normal incidence. The piecewise sinusoidal basis function is presented which can be employed to analyze the hexagon and gangbuster array instead of rooftop basis function and is presented in Chapter 4.

The ECM presented in Section 2.3 is an empirical modeling technique. It allows rapid computation of frequency response and provides relatively accurate analysis for some geometries such as double-square, gridded-square and gridded-double-square elements.

Chapter 3 Optimization Methodology

3.1 Introduction

The design of FSS is in nature an optimization problem. An optimization technique is proposed to avoid traditional trial and error procedure. As mentioned before, one of the objectives of this research is to develop a suitable optimization tool to apply in the design of FSS structures.

The optimization is the process of attempting to obtain a best optimal solution to the problem under consideration. The optimization methods can be classified as local and global techniques. The local and global techniques can be distinguished from each other by the fact that the former produces results that are highly dependent on the initial guesses, while the latter are largely independent of the starting points. The global optimization methods [56-63], including the evolution strategy (ES), the Monte Carlo method, the neural network (NN), the simulated annealing (SA), and the genetic algorithm (GA) [58-63], are in general stochastic. They tolerate deterioration in the objective

function to some extent during the iteration process that enables them to find the region of the global optimum with a high probability no matter where the strategy is started. They are rather simple to implement, stable in convergence, and able to find the desired optimum with a good probability. Since the stochastic strategies are zeroth order methods and hence only the function value of the objective function is required, one does not have to concern about the continuity of the objective function or its gradient during the optimization process. On the other hand, the global techniques are much better at dealing with solution spaces having discontinuities, constrained parameters. Therefore, the global optimization algorithms based on them offer many advantages over the local optimization algorithms such as strong search ability, simplicity, versatility, and high level of robustness. However, they usually demand a high number of function evaluations.

Both GA and differential evolution strategy (DES) are stochastic global optimization methods. GA can be simply classified as the simple genetic algorithm (SGA) with binary-coded, real-coded genetic algorithm (RGA) and their evolvements. In this chapter, three optimization algorithms including SGA, RGA and DES are studied.

Section 3.2 introduces the principle of GA, and the operational process of SGA and RGA. The novel optimization technique for FSS using DES is developed and its operational process is demonstrated in Section 3.3. In Section 3.4, the performance of three optimization algorithms is investigated through a function optimization. DES is found to be the most efficient and robust method among them because of its fastest convergence. Section 3.5 investigates the different combinations of parameter values effecting DES convergence performance.

3.2 Genetic Algorithm (GA)

GA is a set of stochastic global optimization methods based on genetic recombination and evolution in nature. The advent of computers and powerful computational techniques now enables us to apply Nature's optimization processes in the form of genetic algorithm in solving electromagnetic problems. GA has been widely used in solving EM problems such as the synthesis of antennas [64-67], absorbers [68-69], filters [70], inverse scattering problems [71] and FSS [38-42, 72-76]. GA is highly suitable for optimizing multimodal problems, and operates with ease on discrete parameters. It is necessary to create an objective function in the development of GA for a specific problem. This created objective function will be optimized by GA and is linked to the GA code. The objective function is used to measure the difference between the optimized performance and the desired performance. The fitness of an individual population member reflects how good the solution is to the problem being solved. GA operates on a population in the search space simultaneously and performs a global optimization by the three genetic operations, i.e., selection, crossover and mutation. The selection operator is responsible for the algorithm's convergence and the crossover operator is the main search tool. The mutation operator can prevent the premature convergence. The GA is less likely to converge to a local optimum. Traditionally and commonly used GA is the simply genetic algorithm (SGA). In recent years, real-coded genetic algorithm (RGA) has attracted the attention of many researchers because of its simplicity and efficiency.

3.2.1 Simple Genetic Algorithm (SGA)

Genes are the basic building blocks of genetic algorithm. GA operates directly on the encoding of a chromosome, which is composed of an array of genes in a computer algorithm. In SGA, a gene is a binary encoding of a parameter. The flow chart of SGA optimizer [64-66] is shown in Figure 3-1.

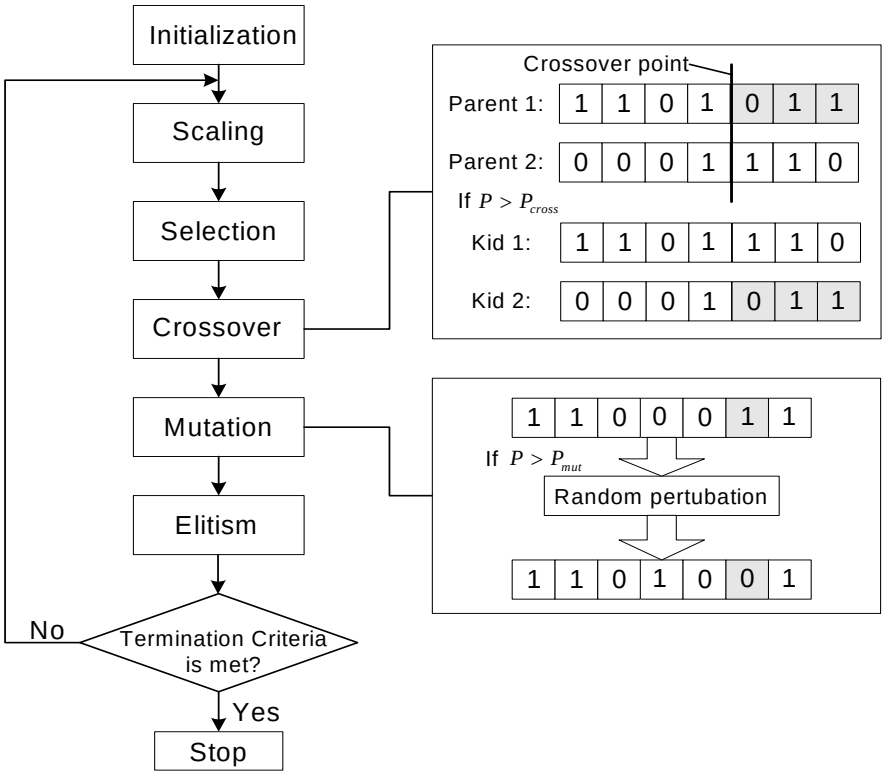

Figure 3-1 Flowchart of SGA

Step 1: Initialization

The SGA starts with constructing an initial population consisting of N_{pop} chromosomes generated randomly within the search space. The chromosome has N_{par}

optimization parameters and each parameter is randomly encoded with L genes. The genes g_j are selected from the binary alphabet {0,1}. The real-valued parameters x_k can be decoded through a simple linear transformation

$$x_k = x_k^{\min} + \frac{\sum_{j=1}^{L} g_j 2^{L-j}}{2^L - 1}(x_k^{\max} - x_k^{\min}), \qquad k = 1, 2, \cdots, N_{par} \tag{3-1}$$

where $x_k^{\min}$ and $x_k^{\max}$ denote the minimum and maximum permissible values of the *kth* parameter, respectively.

Step 2: Scaling Operator

GA is a maximizer by nature. Most of the schemes described are applied to minimization problems. An appropriate fitness scaling is needed in the search for minimum. The operator scales the values of objective function into fitness value through a linear transformation

$$fitness(i) = 1 \Big/ object(i), \qquad i = 1, \cdots, N_{pop} \tag{3-2}$$

where, N_{pop} is the size of population. Each chromosome has an associated fitness function, assigning a relative merit to that chromosome. Fitness values are computed for each chromosome through substituting each initial solution string into the objective function.

The population is entered into the main GA loop to search the optimum solution for the problem. GA operators are applied to the initial population, thereby evolving the initial population into improved generations. These operators are applied in the given order to obtain the next generation of solution strings.

Step 3: Selection Operator

The selection operator implements the principle of the survival of the fittest. The chromosomes are ranked from the most-fit to the least-fit, according to their respective fitness functions. The selective operator selects good chromosomes and produces a mating pool. Unacceptable chromosomes are discarded, leaving a superior species-subset of the original list. The most common selection methods are roulette-wheel, ranking and tournament selection. The tournament selection has been shown to provide faster convergence than the other two selections [62]. The tournament selection method is taken in our research in optimization process. In tournament selection, N chromosomes are selected at random from the population. These N chromosomes compete on the basis of their fitness. The chromosome with the highest fitness wins the tournaments and is placed into the mating pool. Then, these N individuals are placed back into the general population and the process is repeated. In the end, mating pool is usually of the same size as the population size.

Step 4: Crossover Operator

Crossover follows selection. Two parent members are chosen from the mating pool. A pair of children is generated by crossing over the mated pairs with probability P_{cross}. The parents reproduce enough to offset the discarded chromosomes. Thus, the total number of chromosomes remains constant after every iteration. The single-point crossover is taken in our research. Referring to the Figure 3-1, if $P > P_{cross}$, a random crossover point in the parent's chromosomes is selected. The portion of the chromosome preceding the selected point is copied from parent 1 to kid 1, and from parent 2 to kid 2. The portion of the

chromosome of parent 1 following the randomly selected point is placed in the corresponding positions in kid 2, and vice versa for the remaining portion of parent 2's chromosome. If $P < P_{cross}$, the entire chromosome of parent 1 is copied into kid 1, and similarly for parent 2 and kid 2. The crossover operator can produce better individuals. The probability P_{cross} is typically taken as 0.6-0.9 [64].

Step 5: Mutation Operator

The mutation is finally operated to generate the next population by randomly perturbing genes of chromosomes after crossover. Some of the genes in the candidate offspring are inverted with a probability P_{mut}. If $P > P_{mut}$, a gene in the chromosome is randomly selected and changed from 1 to 0 or 0 to 1. Usually, the mutation probability P_{mut} is taken as 0.001-0.1 [64]. The mutation operator provides important features that are not given by the other two operators. Most importantly, it not only provides the algorithm with a mechanism for escaping local maxima but also is included to prevent premature convergence.

Step 6: Elitism Model

The elitist model is used to avoid convergence difficulty. In GA, it is possible for the next generation to have a best individual with a lower fitness than a preceding generation. The Elitism replaces the worst individual in the newly generated generation with the best one in the previous generation.

The iterative application of the scaling selection, crossover and mutation operators leads to new populations with improved average fitness. The process is repeated until an acceptable solution is obtained. The implementation of a stopping criterion depends

highly on the desired optimum solution. Possible termination conditions may due to 1) a given number of generations has been completed; 2) the objective function of the best solution has reached an acceptable level; 3) the sequential increase in the fitness is negligible over several generations; 4) a combination of the above conditions.

3.2.2 Real-coded Genetic Algorithm (RGA)

SGA does not operate directly on the optimization parameters but on a discretized representation of them. Discretization error will inevitably be introduced when encoding a real number. The encoding and decoding operations for the algorithm require longer computational time for problems with real optimization parameters. It is therefore worth developing a novel GA that work directly on the real optimization parameters. In recent years, many researchers have concentrated on using real valued genes in GA (RGA). The RGA is robust, accurate, and efficient because the floating-point representation is conceptually closest to the real design space, and moreover, the string length reduces to the number of design variables. Both theoretical proof and practical experiences show that RGA usually works better than SGA, especially for problems with real optimization parameters [63, 71, 77].

The operation process of RGA is generally similar to those of SGA. The flow chart of RGA is depicted in Figure 3-2. It can be seen that after initializing the population, the selection, crossover and mutation operations are typically preceded by a fitness scaling process, which scales the objective function value into fitness value in RGA optimization process. However, in initialization process, the population is generated according to

$$\mathbf{x}_k = \mathbf{x}_k^{\min} + R_k \times (\mathbf{x}_k^{\max} - \mathbf{x}_k^{\min}), \qquad k = 1, 2, \cdots, N_{par} \tag{3-3}$$

where $R_k \in [0,1]$ is a random real number with a uniform distribution. $\mathbf{x}_k^{\min}$ and $x_k^{\max}$ denote the minimum and maximum permissible values of the kth parameter, respectively.

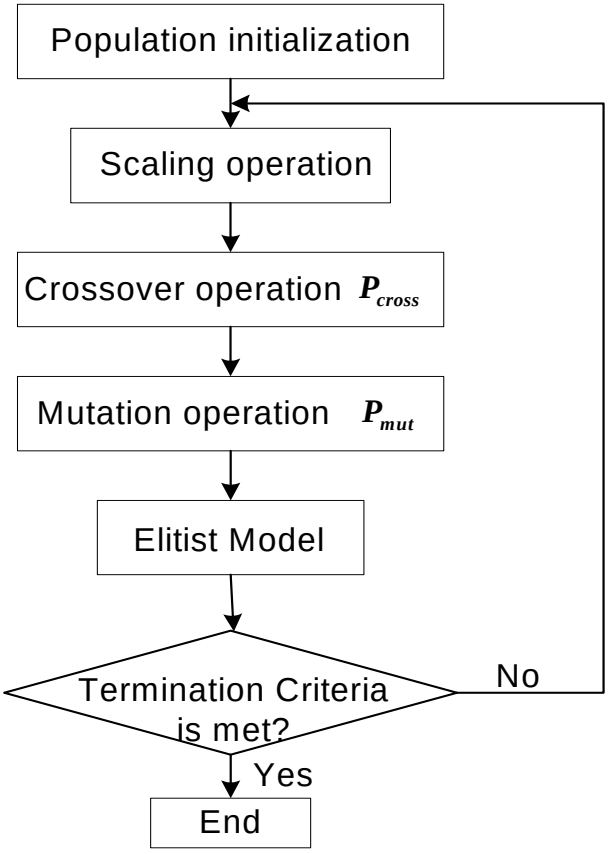

Figure 3-2 Flow chart of RGA

Consequently, the crossover and mutation operators used in RGA are quite different from those in SGA. Here, the arithmetical one-point crossover and the random perturbation mutation are employed and introduced.

Suppose that the *ith* chromosome and the *jth* chromosome in the parents' population are to be crossed. A crossover site k_{cross} is selected randomly within the range of $1 \le k_{cross} \le N_{par}$. Then, the two new children members are generated by keeping the genes of the parents members between position 1 and k_{cross} unchanged, and swapping the genes of the parents members between position $k_{cross}+1$ and N_{par} as follows

$$\begin{aligned} x_k^{c,i} &= \alpha x_k^{p,i} + (1-\alpha) x_k^{p,j} \\ x_k^{c,j} &= (1-\alpha) x_k^{p,i} + \alpha x_k^{p,j} \end{aligned}, \qquad k_{cross}+1 \le k \le N_{par} \tag{3-4}$$

where the superscript c and p represent children and parents respectively. $x_k^{p,i}$ and $x_k^{p,j}$ are the two parents members with $x_k^{c,i}$ and $x_k^{c,j}$ being the two children members. $0 \le \alpha \le 1.0$ is a random real number.

The mutation is finally operated to generate the next population by randomly perturbing genes of chromosomes after crossover. The random perturbation mutation alters a gene of the candidate offspring by adding a random perturbation term on it. A gene is altered with a probability P_{mut} according to

$$x_k^{m,i} = x_k^{c,i} + \beta \gamma_k \tag{3-5}$$

where the superscript m and c denote mutation and crossover respectively. β is a random real number which ranging from $-1.0 \le \beta \le +1.0$, γ_k is the mutation amplitude of the *kth* gene and is typically 10% or less of the search range of the *kth* variable. Here, $\gamma_k = 0.01 \times \left(x_k^{\max} - x_k^{\min} \right)$.

3.3 Differential Evolution Strategy (DES)

The other global optimizer, the differential evolution strategy (DES) [78-79] is one of the recent significant inventions in optimization field. DES is quite similar to the GA but the operators involved are quite different. In each evolution loop of DES, the mutation, crossover and selection operations are executed in sequence. DES has already been applied to the solution of various challenging engineering tasks. It has been rapidly gaining in acceptance and has been shown to outperform other known global optimization methods on a number of synthesized problems [78-86]. It is a powerful and simple evolutionary algorithm for optimizing real-valued, multi-modal functions. Function parameters are encoded as floating-point variables and mutated with a simple arithmetic operation. With its power, speed, simple construction and ease of use, DES is becoming an important tool for routinely extracting solutions to other real-world problems.

3.3.1 Operation Process of DES

As mentioned before, DES is very similar to GA. DES also operates on a population of N_{pop} candidate solutions, or chromosomes. Each chromosome consists of N_{par} parameters, or genes, represented by floating-point numbers. In DES, the executing sequence of the main evolution loop is the mutation, crossover and selection while the selection, crossover and mutation in sequence for GA evolution. Next, the operation process of DES is introduced. Figure 3-3 shows the flowchart of the DES. Full details can be found in Appendix C.

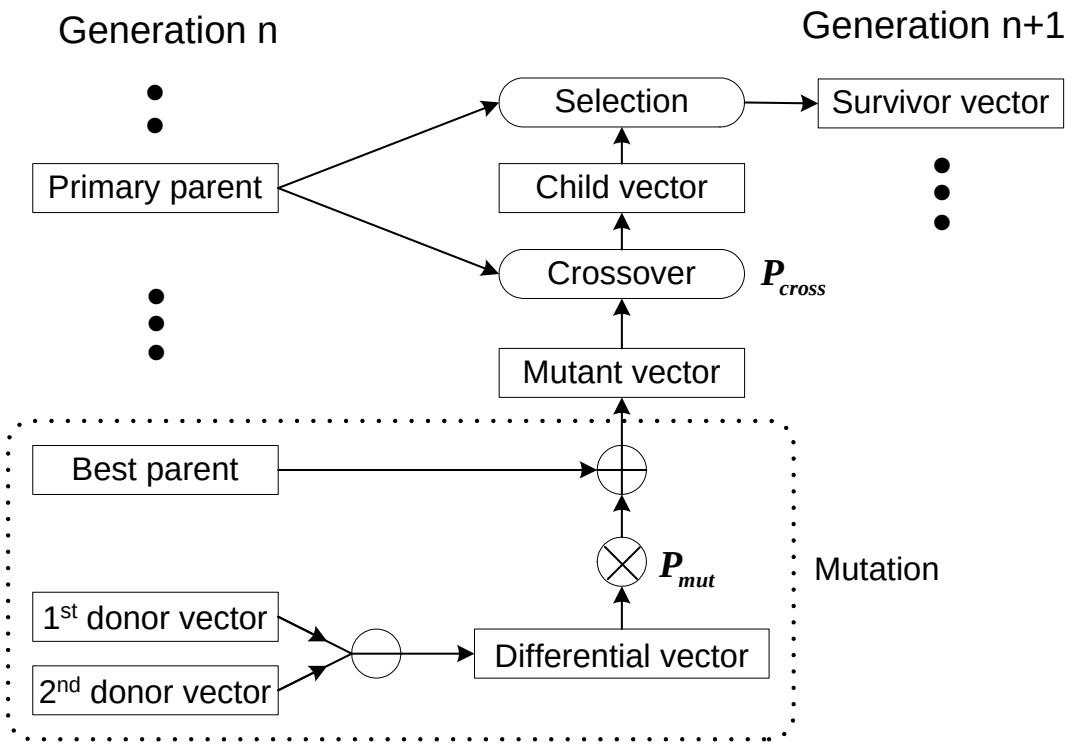

Figure 3-3 Flowchart of DES

Step1: Initialization

For establishing a starting point for seeking optimum, the population must be initialized. The initial population is generated according to

$$\mathbf{x}_{i,j}^{P} = \mathbf{x}_{j}^{\min} + R_j \times (\mathbf{x}_{j}^{\max} - \mathbf{x}_{j}^{\min}), \quad 1 \le i \le N_{pop}, \quad j = 1, 2, \cdots, N_{par} \tag{3-6}$$

Where $R_j \in [0,1]$ is a random number with a uniform distribution, and $x_j^{\min}$ and $x_j^{\max}$ denote the minimum and maximum permissible values of the jth parameter respectively. The population size is set initially and generally kept constant for all generations. After initialization, the algorithm evolves to the genetic evolution loop by mutation, crossover and selection operator in sequence.

Step 2: Mutation Operator

Mutation operation is the key procedure in DES. The basic idea is that a differential vector (mutant vector) is created by subtracting two distinct donor vectors randomly selected from the current population.

$$\mathbf{x}^{m,i} = \mathbf{x}^{n,opt} + P_{mut}(\mathbf{x}^{n,p_1} - \mathbf{x}^{n,p_2}),\ i \neq p_1 \ \ and \ \ i \neq p_2 \tag{3-7}$$

where the superscript m denotes mating pool, $\mathbf{x}^{n,opt}$ represents the best chromosome in nth generation and $\left\{\mathbf{x}^{n,p_1}, \mathbf{x}^{n,p_2}\right\}$ are the two arbitrary distinct chromosomes for parent nth generation. They are different from each other and also different from $\mathbf{x}^{n,opt}$. The mutation intensity P_{mut} is the real-valued factor which is commonly in the range of [0.4,1] that scales the differential variations, and therefore controls mutation operation [78]. To avoid the values of some individuals exceed their prescribed upper and lower search range of $\left\{\mathbf{x}_j^{\min}, \mathbf{x}_j^{\max}\right\}$, it will be replaced by taking the average

$$\left(\mathbf{x}^{m,i}\right)_j = \begin{cases} \dfrac{\left(\mathbf{x}^{m,i}\right)_j + \mathbf{x}_j^{\max}}{2} \\ \dfrac{\left(\mathbf{x}^{m,i}\right)_j + \mathbf{x}_j^{\min}}{2} \end{cases}, \qquad 1 \le i \le N_{pop}, \quad j = 1, 2, \cdots, N_{par} \tag{3-8}$$

Step 3: Crossover Operator

Crossover is the next operation in which child vectors $\mathbf{x}^{c,i}$ is formed where

$$\left(\mathbf{x}^{c,i}\right)_j = \begin{cases} \left(\mathbf{x}^{M,i}\right)_{j,} & \gamma \le P_{cross} \\ \left(\mathbf{x}^{n,i}\right)_{j,} & otherwise \end{cases}, \quad 1 \le i \le N_{pop}, \qquad 1 \le j \le N_{par} \tag{3-9}$$

The superscript c denotes children population, γ is a real random number in the range of [0,1] and P_{cross} is the probability of crossover. If $\gamma \le P_{cross}$, the gene is loaded from the mutant vector. Otherwise, it is loaded from the parent vectors. To ensure that parent and child vectors differ in at least one gene, a randomly chosen gene of the child will be replaced by the corresponding gene of the mutant vector. P_{mut} and P_{cross} both are important control parameters in DES optimization process.

Step 4: Selection Operator

The selection operation is to produce better offspring. Unlike the GA, DES does not use ranking or tournament selection. Instead, the fitness value of each child $x^{c,i}$ competes with that of its parent $x^{n,i}$, and survives in next generation only if its fitness is better. This selection criterion results in fast convergence. As the result, all the individuals of the next generation are as good as or better than their counterparts in the current generation.

$$\mathbf{x}^{n+1,i} = \begin{cases} \mathbf{x}^{c,i}, & if \quad fitness(\mathbf{x}^{c,i}) < fitness(\mathbf{x}^{n,i}) \\ \mathbf{x}^{n,i}, & otherwise \end{cases} \tag{3-10}$$

Step 5: Iteration

The initial population evolves to the better next generation by mutation, crossover (or recombination), and selection. The evolution is continuous until either the best population yields the desired tolerance, or the generation count reaches the maximum number.

3.3.2 Difference between DES and RGA

According to the above description of the operation process, the advantages of DES over RGA can be summarized in the following.

Firstly, in DES, the selection of parents is not based on fitness. Each individual of the current generation can become a primary parent only once. A crossover with a mutated secondary parent creates one child, not two, as in most RGA. This child is only compared to one individual: its primary parent, not to all of the individuals in the current population, and the fitter one wins a spot in the next generation. As a result, all of the individuals of the next generation are as good as or better than their counterparts in the current generation. Hence, DES does not require the elitist strategy widely used in RGA.

Secondly, in RGA, the selection, crossover and mutation are executed in sequence. However, in DES, the executing sequence is the mutation, crossover and selection. The former shows the slower convergence under this executing order. DES avoids the slow convergence by mutating secondary parents with population-derived difference vectors. As generations pass, these differentials tend to adapt to the natural scaling of the problem. For example, if the population becomes compact in one variable but remains widely dispersed in another, the differentials sampled from it will be small in the first variable, but larger in the other. This automatic adaptation significantly improves the convergence of the algorithm.

Finally, in RGA, all offspring are accepted and all parents are abandoned at the end of every operation, regardless of their characteristics. This gives rise to a problem that good parent may be replaced by its deteriorated offspring. Consequently, improvement on the

average performance of the offspring population over its parent population cannot always be guaranteed. The DES eradicates the drawbacks of the RGA as mentioned before. It gives all parent individuals equal chance to generate offspring. The mutation operation is carried out on parent individuals instead of potential offspring individuals at the beginning of each evolution loop. After crossover, the offspring individual competes with its parent to qualify in the next generation. The average performance of the offspring population over its parent population is improved.

3.4 Function Optimization

The performance of SGA, RGA and DES are investigated by minimizing the following objective function.

$$f(\mathbf{x}) = \sum_{i=1}^{20} x_i^2 \tag{3-11}$$

The optimization parameters and population size are set to be $N_{par} = 20$ and $N_{pop} = 200$ respectively. The search range of the solution is set within $-500.0 \le x_i \le +500.0$. The convergence criterion is set to be $f(x) < 0.01$. The program will be terminated after 1000 generations if it still cannot be converged. For fair comparison, all the simulation of SGA, RGA and DES are based on the above conditions.

For SGA, the length of the code string of the optimization parameter is set to be 8. The best combination of the crossover probability and the mutation probability is $P_{cross} = 1.0$ and $P_{mut} = 0.04$ respectively. For RGA, $P_{cross} = 0.9$ and $P_{mut} = 0.1$. For DES,

the crossover probability and the mutation intensity is taken as $P_{cross} = 0.9$ and $P_{mut} = 0.7$ respectively. Ten trials were conducted to eradicate the randomness. The simulation convergence curves of SGA, RGA and DES for the above function optimization are shown in Figure 3-4 and Figure 3-5. In order to present the difference clearly, the average values for DES and RGA with their variations are shown in Figure 3-5(b).

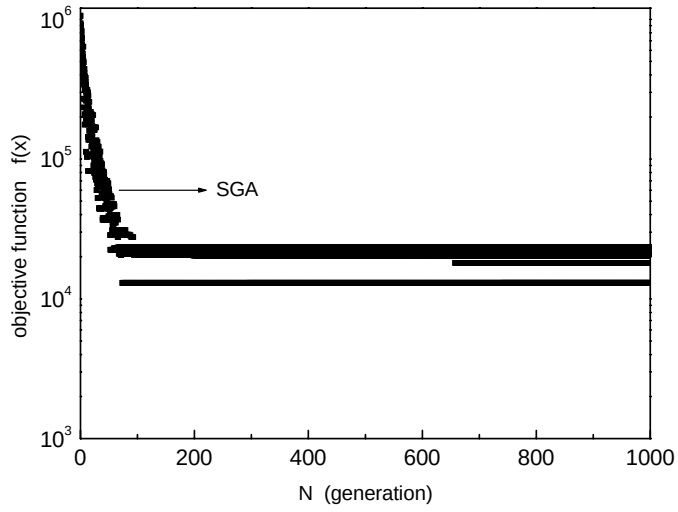

Figure 3-4 Convergence behaviour of SGA for function optimization

It can be seen that SGA cannot converge to desired criterion within larger search range and higher numbers of optimized parameters as shown in Figure 3-4. In SGA, an acceptable optimization result is possible when the search range is reduced to $-20.0 \le x_i \le +20.0$. The number of parameters is reduced to $N_{par} = 10$ and the convergence criterion is reset as $f(x) \le 0.03$. The population size N_{pop} remains to be 200. Ten trials were executed. The results are shown in Figure 3-6.

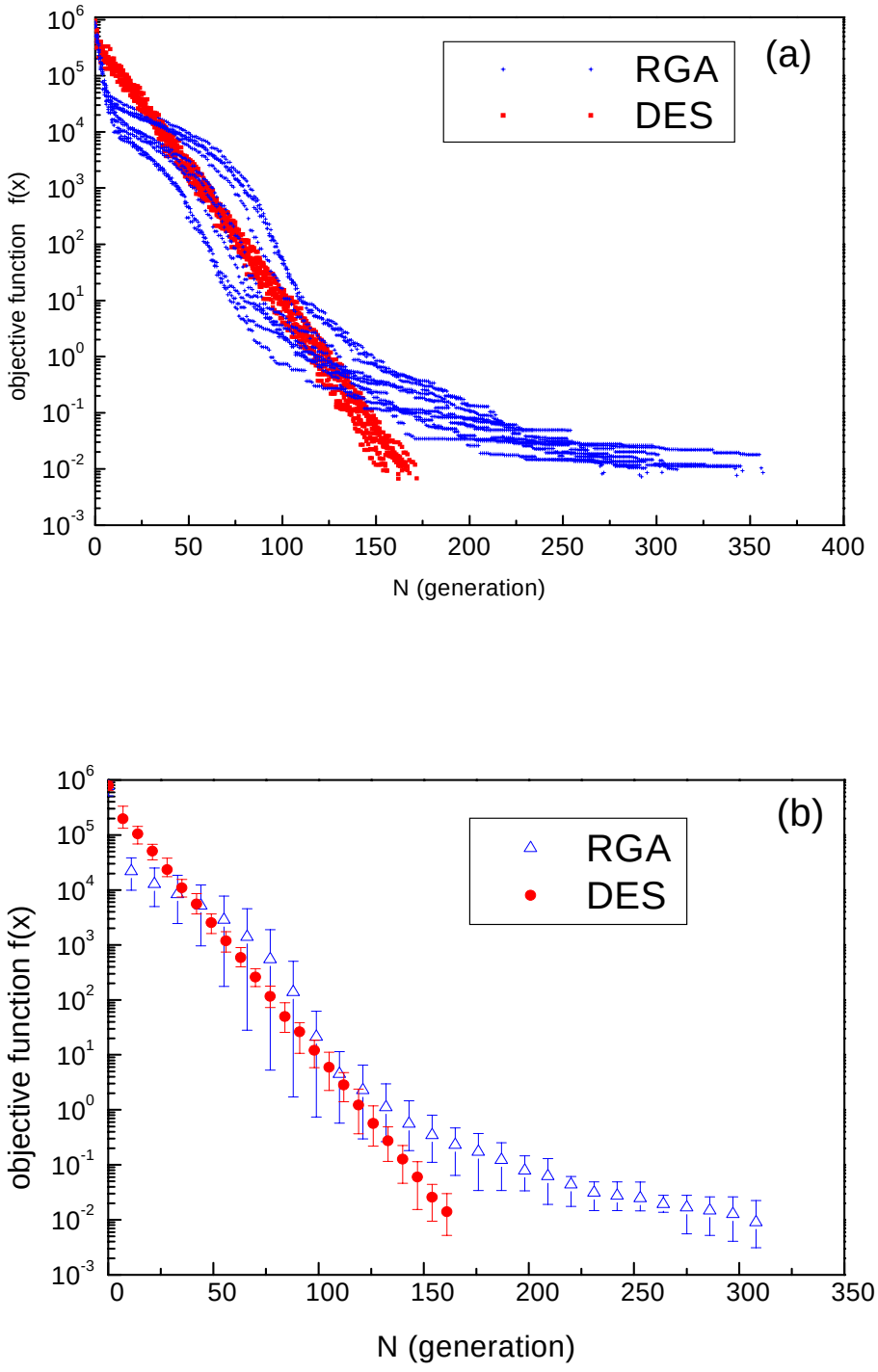

Figure 3-5 Function optimization (a) Comparison of convergence behaviour between DES and RGA (b) The average values for DES and RGA with their variations

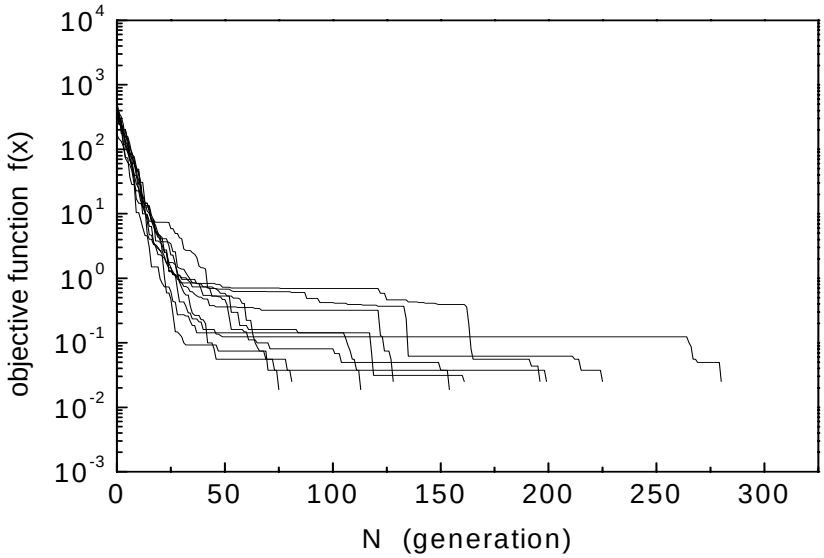

Figure 3-6 Convergence behaviour of SGA after reducing the parameters numbers, the search range and convergence criterion

Referring to Figure 3-5, both RGA and DES are able to search and obtain the acceptable optimum solution. In the simulation of DES, the total number of generations that converges to the desired solution is between 154 and 172 with the average number of generations being 163. In the simulation of RGA, the required number of generations is between 271 and 357 with the average number of generations being 308. Obviously, the DES outperforms the RGA because the former converges to the desired solution with fewer generations than RGA. Furthermore, the search abilities of RGA and DES are much stronger than SGA from the comparison between Figure 3-4 and Figure 3-5. As mentioned before, RGA and DES operate on the real valued parameters directly while SGA operate on the binary code. RGA and DES are more efficient than SGA since the encoding and decoding operation are avoided. In conclusion, DES is the most efficient and robust optimization tool among the three.

3.5 Parameter Control in DES

In DES, the selection for values of population size (N_{pop}), crossover probability (P_{cross}) and mutation intensity (P_{mut}) is very important. It will determine the convergence performance of DES and also the efficiency of obtaining an optimum solution. To find out the best combination of those parameters that give the solution of the problem accurately and efficiently, the experiments are conducted by minimizing the following object function

$$f(\mathbf{x}) = \sum_{i=1}^{30} \left(x_i - i \right)^2 \tag{3-12}$$

The optimization parameters are $N_{par} = 30$. The search range of the solution is set within $-500.0 \le x_i \le +500.0$. The convergence criterion is set to be $f(x) < 0.001$. The program will be terminated after 1000 generations if it still cannot be converged.

Six trials were run for each case to eradicate the randomness. The population size is taken as $N_{pop} = 200$. The comparisons of convergence behaviour for various combinations of P_{cross} and P_{mut} are shown in Figure 3-7. The combinations that were not included in figure are those which cannot be converged within 1000 generations such as $P_{cross} = 0.9, P_{mut} = 0.6$ and $P_{cross} = 0.9, P_{mut} = 0.9$. It is observed that DES has the better convergence performance at $P_{mut} = 0.7$ for this function optimization.

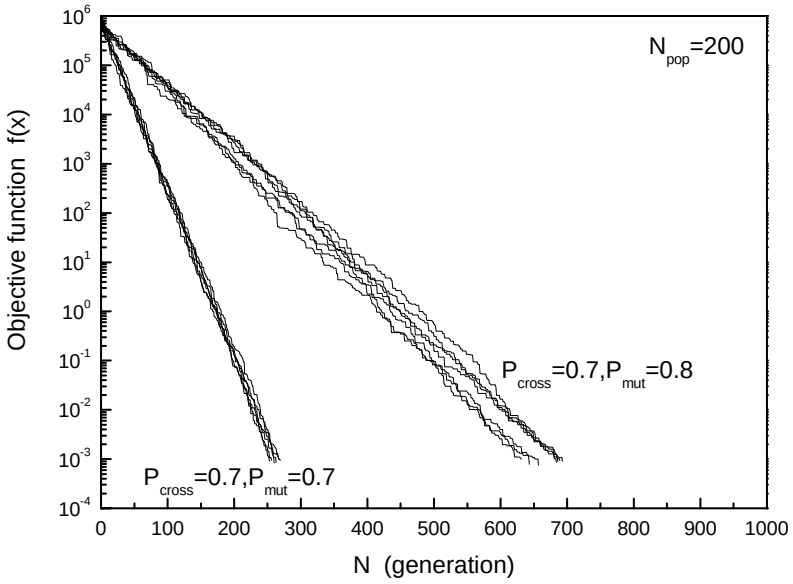

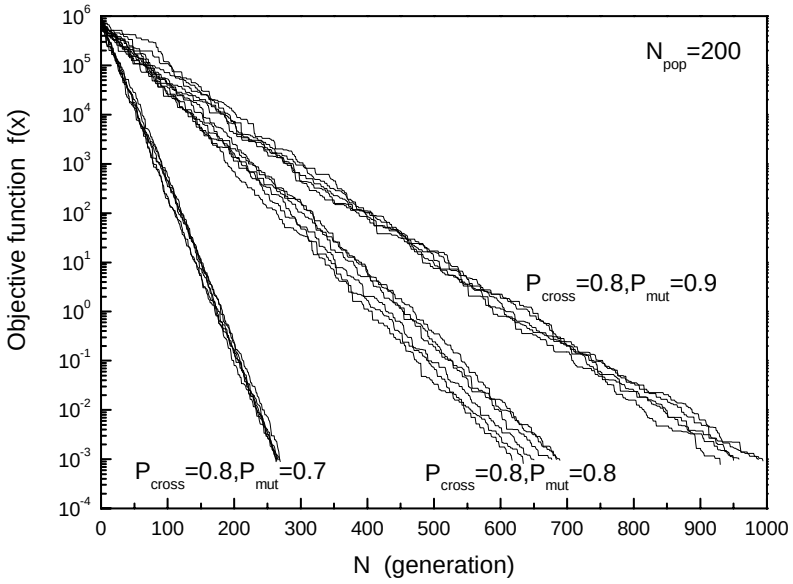

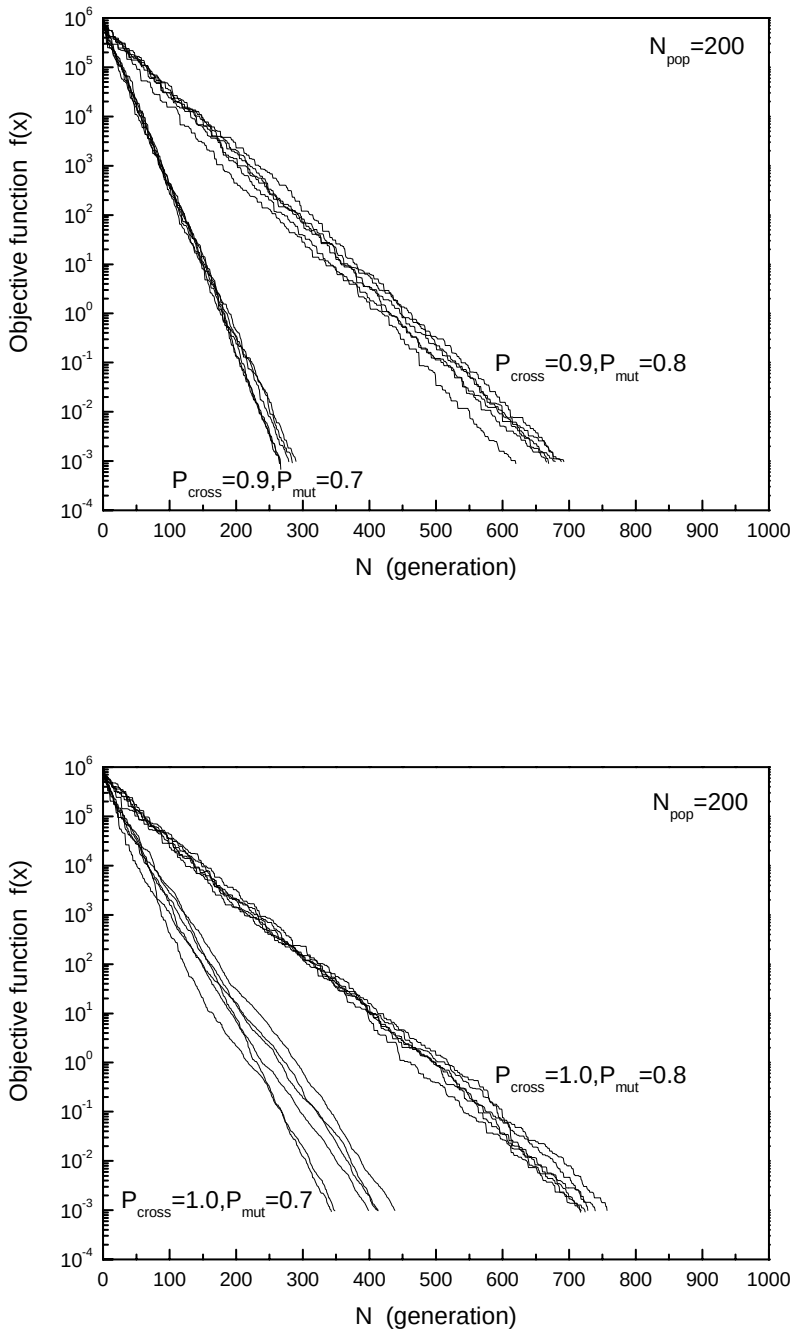

Figure 3-7 Convergence behaviour for function optimization with different combinations of P_{cross} and P_{mut} at $N_{pop} = 200$

Table 3-1 presents the average convergence generations for different value of crossover probability at $P_{mut} = 0.7$ and $N_{pop} = 200$. Increasing the population size to 300, the average convergence generations for different P_{cross} are shown in Table 3-2. It is observed that DES has the fastest convergence speed when the crossover probability is taken as 0.7. Furthermore, it needs longer convergence time with the increment of population size.

Table 3-1 Average convergence generations for different crossover probability at $P_{mut} = 0.7$ and $N_{pop} = 200$

Crossover probability (P_{cross})	Mutation intensity (P_{mut})	Average convergence generations
0.7	0.7	261
0.8	0.7	266
0.9	0.7	275
1.0	0.7	392

Table 3-2 Average convergence generations for different crossover probability at $P_{mut} = 0.7$ and $N_{pop} = 300$

Crossover probability (P_{cross})	Mutation intensity (P_{mut})	Average convergence generations
0.7	0.7	274
0.8	0.7	279
0.9	0.7	288
1.0	0.7	309

The typical value of the population size (N_{pop}) is often set as between $5\times N_{par}$ and $10\times N_{par}$. The bigger size of the population can create more chances for DES to converge to the global optimum at the expense of computational time. The crossover probability (P_{cross}) is often taken as [0,1]. A value of close to one for P_{cross} will increase the speed of DES convergence. The mutation intensity (P_{mut}) is suggested to take the range of [0.4,1]. Greater values of P_{mut} make it possible to explore the whole search space and to prevent premature convergence of DES. For the complicated optimization problem such as the design of FSS, it is desirable to have bigger population size, greater crossover probability and mutation intensity in order to obtain the optimum solution.

3.6 Conclusions

Optimization tools are proposed to apply in the design of FSS in our research. In this chapter, three global optimization algorithms, namely SGA, RGA and DES are investigated.

The operation process of SGA is described in Section 3.2.1. SGA operates on the binary encoding of a chromosome. It requires lengthy computational time for problems with real optimization parameters since encoding and decoding operations are the requirements. In SGA, the selection, crossover and mutation operators are executed in sequence preceded by a fitness scaling process after initializing the population. From the function optimization presented in Section 3.4, it can be seen that the convergence behaviour of SGA is poorer than RGA and DES. It only can be converged under narrower search range, less optimization parameters and lower convergence criterion.

The operation process of RGA is demonstrated in Section 3.2.2. The process is generally similar to that of SGA. However, the crossover and mutation operators used in RGA are quite different from those in SGA. RGA operates directly on the optimization parameters and avoids the encoding and decoding operation. From comparison of the function optimization in Section 3.4, it can be concluded that RGA is robust, accurate, and efficient optimization tool but it has poorer convergence performance than DES.

Section 3.3 gives the operation process of DES and the theory comparison between DES and RGA. In DES, the mutation, crossover and selection operators are executed in sequence. Furthermore, DES does not require the scaling operator and elitist strategy.

Section 3.4 investigates the convergence behaviours of SGA, RGA and DES through minimizing the objective function. All comparison made for SGA, RGA and DES are based on the same conditions including the search range, convergence criterion. DES is found to have the most efficient and robust optimization tool among them because of its fastest convergence. Thus, DES will be chosen as optimization tool to optimize the FSS unit cell and dielectric properties in the design of FSS with prescribed performance in this thesis.

In DES, the user is required to choose three parameters values. They are population size (N_{pop}), crossover probability (P_{cross}) and mutation intensity (P_{mut}). Section 3.5 investigates the effect for DES convergence performance with different parameters combinations in function optimization. The selections of parameters values are suggested for solving optimization problems.

Chapter 4 Design of Frequency Selective Surfaces Using Differential Evolution Strategy Coupled with spectral-domain Method of Moments

4.1 Introduction

Although theoretical analysis of FSS structures has been studied extensively [2-3], little research has been conducted on the systematic design of FSS. The design of FSS is a challenging problem as its performance depends on various parameters such as the shape of FSS unit-cell, the number of FSS screens and dielectric layers, as well as their electrical properties. Moreover, synthesizing an FSS with a desired frequency response is usually conducted through a tedious trial and error procedure. For complex applications, such as the design of wide-band band-pass or band-stop filters using multi-screen FSS embedded in multi-layered dielectric, the conventional trial and error approach is very time-consuming, extremely cumbersome, and may in fact fail to realize a successful design. The growing popularity of FSS has stimulated the urgent need to develop an efficient algorithm to guide the design of FSS.

The design of FSS is in nature an optimization problem. The field of optimization of FSS design has recently become popular because the conventional analytic approach are

not general sufficiently, and it is limited for human mind to conceive a successful FSS configurations to meet the specifications for a particular design without the benefit of an optimization procedure. Optimization approach is more systematic and not only assures a high degree of freedom in the definition of the elements, but also is instrumental in realizing FSS that meet the prescribed frequency specifications.

Previous work on optimization of FSS has primarily focused on the applications of Genetic Algorithm (GA) [38-42, 72-76]. Chakravarty *et al* have utilized successfully a micro-genetic algorithm (MGA) to design the spatial filters and broad-band microwave absorbers employing multiple FSS screen and multiple dielectrics [39-42]. In their designs, Genetic Algorithm with binary coded can randomly generate the cell structure of FSS screen with 16×16 (or 32×32) gridded discretization. As mentioned before, the resulted unit cells are complicated and irregular in shape which is difficult to fabricate. Furthermore, the continuous current existing on the border of produced unit cell should be treated in particular. Otherwise, it would cause incorrect simulation results if only rooftop basis function is employed. However, the continuous current cannot be avoided on the border of unit cell using their approach. In addition, their approach cannot handle the conductor current in the slanting direction because of rooftop basis function employed. As a result, some geometries with good performance may be missed and it is unable to give the optimum design. Responding to the above drawbacks, the other optimization algorithm (not binary-coded) is employed to optimize the standard, non-irregular structure of FSS unit-cell [2-3] and dielectric properties with the prescribed frequency response in this thesis.

In chapter 3, the performance of GA (SGA and RGA) and DES are compared for the same function optimization. The results exhibit that DES has the faster convergence performance than SGA and RGA. Therefore, in this chapter, DES is chosen as optimization algorithm. In the optimization of FSS, the objective function is the relative error of the frequency response of FSS. Thus, analysis of FSS is of great importance in the design of FSS. The spectral-domain MoM technique is the most popular for the analysis of FSS among several techniques available and is used as analysis tool to obtain the frequency response of FSS screen. For the analysis of hexagon array and gangbuster array, piecewise sinusoidal basis function is employed instead of rooftop basis function.

The FSS design process using optimization approach is explained in Section 4.2. In Section 4.3, an FSS dipole array with and without dielectric substrates is selected as the design objective. The entire-domain basis functions of the dipole elements in spectral domain are derived. Examples are given to demonstrate the design of FSS using DES combined with spectral-domain MoM. For comparison, RGA is also applied to optimize the same FSS construction design (Section 4.4.1). In Section 4.4, the multi-layered gangbuster array and hexagon array are designed for the application of band-pass or band-stop filter using the proposed approach. The gangbuster array and hexagon array are chosen due to their superior bandwidth and stability to different incident angles and polarization. These two arrays are analyzed by employing piecewise sinusoidal basis function instead of common rooftop basis function. By using our proposed optimization method, DES coupled with spectral-domain MoM, the arbitrarily desired band-stop or band-pass filter can be obtained by optimizing the dimensions and dielectric properties of gangbuster array or hexagon array.

4.2 Design Process of FSS Structures

For the design of FSS, one often starts with a given desired frequency response or a set of FSS specifications. A key step in the design procedure entails the choice of the parameters controlling the optimization procedure. Referring to Figure 2-3, the optimization of FSS with multi screens and multi-layered mediums depends on the following parameters:

1) The geometry of the FSS unit cell.
2) The periodicity of the FSS unit cell.
3) The thickness and the permittivity of each dielectric layer.
4) The position of FSS screens.

For a freestanding FSS, only optimization parameters of the above 1) and 2) are applied.

The objective function is mathematically defined as a relative error function with respect to the frequency response of the FSS [82]. The relative error function gives a measurement on how close the optimization results approach the true profile. The problem of FSS design can therefore be cast into an optimization problem by minimizing the relative error function of frequency response coefficients affected by the optimization parameters.

The flow chart of the design process of FSS using DES is shown in Figure 4-1. The optimization starts with a random initial population. The chromosomes randomly select a set of genes, representing individual optimization parameters. These parameters consist of the information of the FSS structures. In RGA, the initial population evolves to the better next generation by the scaling selection, crossover and mutation operators in sequence. However, in DES, the iterative application of the mutation, crossover and selection

operators in sequence leads to new populations with improved average fitness. Keeping the best individual from the previous converged generations, a new random population is chosen and the evolution process restarted. The objective function can be achieved by the relative difference of the root mean square of the actual and the desired FSS frequency response. FSS characteristics obtained from the analysis of MoM are compared with the prescribed specifications. If the results fail to satisfy the desired specifications, the designable (optimization) parameters of the FSS are altered in a systematic manner. Members of the entire sub-population are then put back into the general population and the process is repeated. The sequence of FSS analysis, comparison with the desired performance, and modification of optimization parameters is performed iteratively until the combined composites exhibit the desired frequency response for a prescribed set of frequencies and angles for the TE or TM polarization.

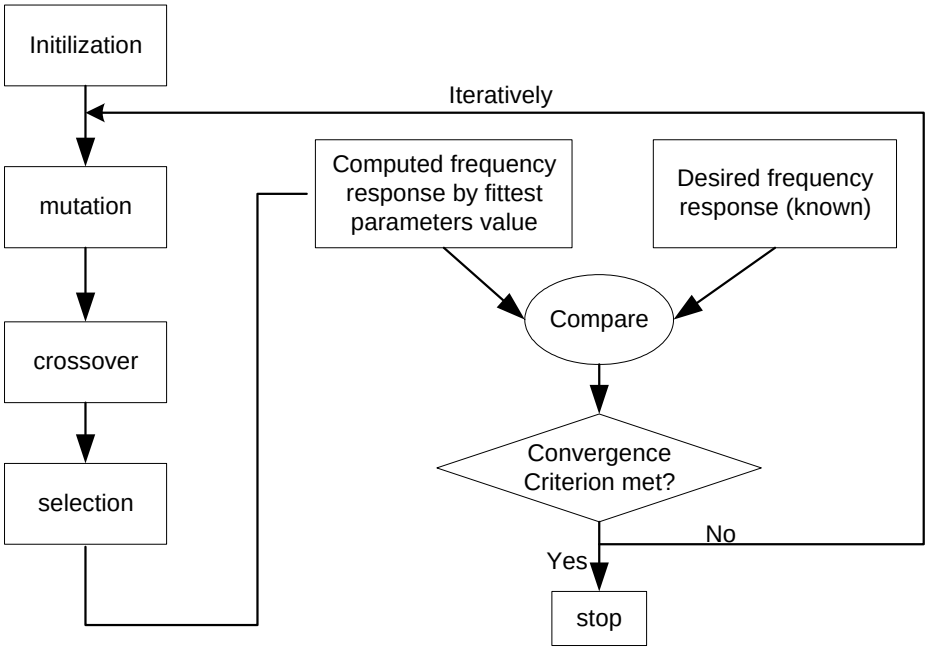

Figure 4-1 Flow chart of the FSS design process using DES

4.3 Design of FSS Dipole Array

4.3.1 Synthesis Construction

A dipole array without and with dielectric substrate as shown in Figure 4-2 is considered here to demonstrate the above-proposed approach because of its simplicity in analyzing its performance, easy fabrication and application.

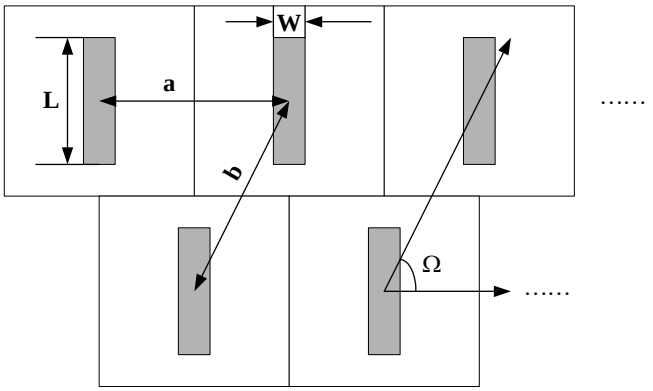

(a)

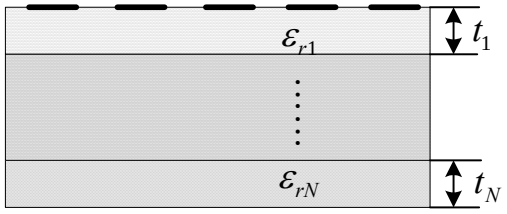

(b)

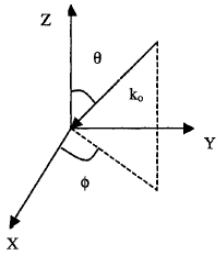

(c)

Figure 4-2 FSS dipole array (a) skewed freestanding FSS (b) with substrates (c) incidence

A key step in the design procedure entails the choosing of the parameters controlling the optimization procedure. Referring to Figure 4-2, the configuration parameters of an FSS with dipole elements are: the periodicity a in the x direction, the periodicity b in the oblique direction, the width W of the dipole, the length L of the dipole, the skewed

angle Ω, electrical characteristics of dielectric substrate ε_r and the thickness of dielectric substrate t. For freestanding FSS, five optimization parameters are determined as $\mathbf{x} = [a, b, L, W, \Omega]$.

Mittra *et al* [2] have presented the entire-domain basis functions for typical FSS elements such as dipole, square patch, cross dipole and Jerusalem cross. The basis functions of the dipole element in spatial domain are

$$\begin{aligned} J_{xp} &= 0 \\ J_{yp} &= \hat{y} \sin\left[\frac{p\pi}{L}(y + \frac{L}{2})\right] P_x(0, W) P_y(0, L) \end{aligned} \tag{4-1}$$

where $p = 1, 2, \cdots$, W and L are the width and length of the dipole respectively, and

$$P_x(x_0, W) = \begin{cases} 1, & |x - x_0| \le \dfrac{W}{2} \\ 0, & otherwise \end{cases}$$

$$P_y(y_0, L) = \begin{cases} 1, & |y - y_0| \le \dfrac{L}{2} \\ 0, & otherwise \end{cases}$$

Therefore, the current basis functions in the spectral domain are derived as

$$\tilde{J}_{xp} = 0$$

$$\tilde{J}_{yp}(\alpha, \beta) = jW \sin c(\alpha W/2) \frac{L}{2} \left\{ \frac{\sin c\left[(p\pi/L + \beta)\frac{L}{2}\right]}{j^p} - j^p \sin c\left[(p\pi/L - \beta)\frac{L}{2}\right] \right\} \tag{4-2}$$

Although a simple dipole array can easily be designed by crude analytical approach from an experienced designer, our intension here is to demonstrate the efficiency and

robustness of this newly proposed optimization algorithm. Ideally one wishes to apply synthesis, based on a desired frequency response, to obtain the desired parameters of the FSS. The objective function is defined here as:

$$f(\mathbf{x}) = \left\| \mathbf{F}_{desired} - \mathbf{F}_{comp}(\mathbf{x}) \right\| / \left\| \mathbf{F}_{desired} \right\| \tag{4-3}$$

where $\mathbf{x} = [\mathbf{x}_1, \mathbf{x}_2, \cdots, \mathbf{x}_N]$ is the vector of optimization parameters,

$$\left\| \mathbf{F}_{desired} - \mathbf{F}_{comp}(\mathbf{x}) \right\| = \sqrt{\sum_{j=1}^{M} \left\{ (\mathbf{F}_{desired})_j - \left[\mathbf{F}_{comp}(\mathbf{x}) \right]_j \right\}^2} \tag{4-4}$$

$$\left\| \mathbf{F}_{desired} \right\| = \sqrt{\sum_{j=1}^{M} \left[(\mathbf{F}_{desired})_j \right]^2} \tag{4-5}$$

M is the total number of test frequencies. $\mathbf{F}_{desired}$ and $\mathbf{F}_{comp}$ are the desired and computed vectors containing the reflection coefficients or transmission coefficients respectively.

The computer programs were written with Fortran to optimize FSS structures and the transmission or reflection coefficient for FSS is calculated. The simulations in this chapter are carried out on Compaq P-III-1GHz PC. The software is FORTRAN POWERSTATION 4.0 under WINDOWS' 2000.

4.3.2 Design of Freestanding FSS Dipole Array

4.3.2.1 Comparison of RGA and DES Applied to Design of a Dipole Array

A freestanding FSS dipole array is shown in Figure 4-2(a). Figure 4-3 shows the desired frequency response by simulating a freestanding FSS dipole array for the configuration parameters $\mathbf{x} = [a, b, L, W, \Omega] = [10mm, 10mm, 7.5mm, 1.875mm, 90^0]$ [2].

The design specifications are: the incident wave is TE polarized wave, and the angle of incidence is set as $\theta = 45^o$, $\phi = 1^o$.

Firstly, we applied RGA to optimize this FSS construction design [75]. The specific RGA adopted in this work employs a standard tournament selection scheme. The optimization parameters and the population size are chosen to be $N_{par} = 5$ and $N_{pop} = 50$ respectively. The optimization is terminated after 200 generations. The convergence criterion is set to be $f(x) < 0.012$. The crossover probability and the mutation probability are set as $P_{cross} = 0.9$ and $P_{mut} = 0.1$ respectively. The search ranges of five optimization parameters are set as follows: $5mm \le a \le 15mm$, $5mm \le b \le 15mm$, $5mm \le L \le 10mm$, $1mm \le W \le 2mm$, $80^0 \le \Omega \le 90^0$. The frequency range considered here is between 1 GHz and 28 GHz and the frequency step is set as 0.1 GHz. The total number of frequency points is 301. Several trial runs were conducted and the typical results are plotted as shown in Figure 4-4 to Figure 4-8.

The convergence behaviour of RGA is shown in Figure 4-4. The program was terminated in 73rd generation where the objective function $f(x) < 0.012$ satisfied the convergence criterion. The versatility of this proposed RGA technique is evident in its ability to design the performance of FSS with a desired frequency response. Each generation of evolution in RGA simulation takes about 3 minutes and 43 seconds on average. The CPU time of the whole simulation process for RGA is 4 hours and 30 minutes. The values of optimization parameters obtained in the last generation (73rd) are compared to the true values respectively and the results are tabulated in Table 4-1. From the table, the values of the last generation are in good agreement with the true values.

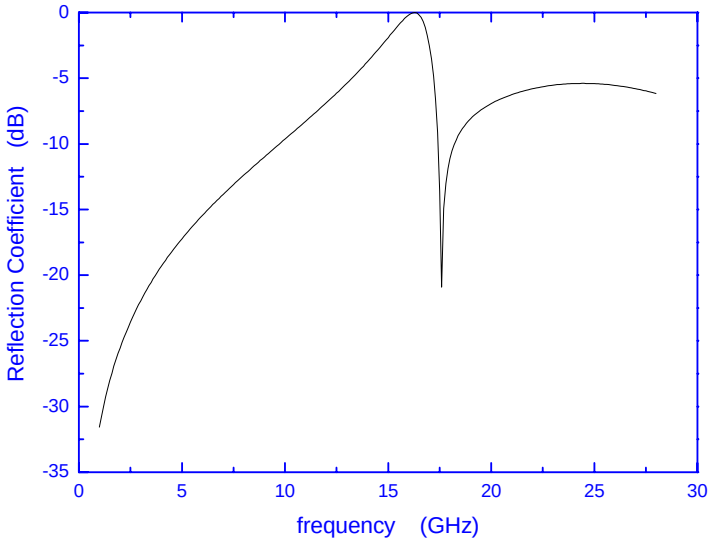

Figure 4-3 Desired FSS frequency response

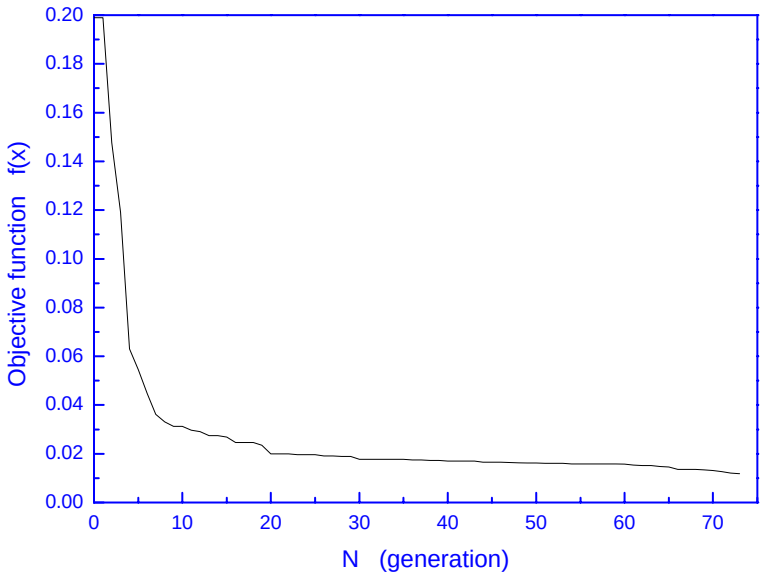

Figure 4-4 Convergence behaviour of RGA applied in the design of a freestanding FSS

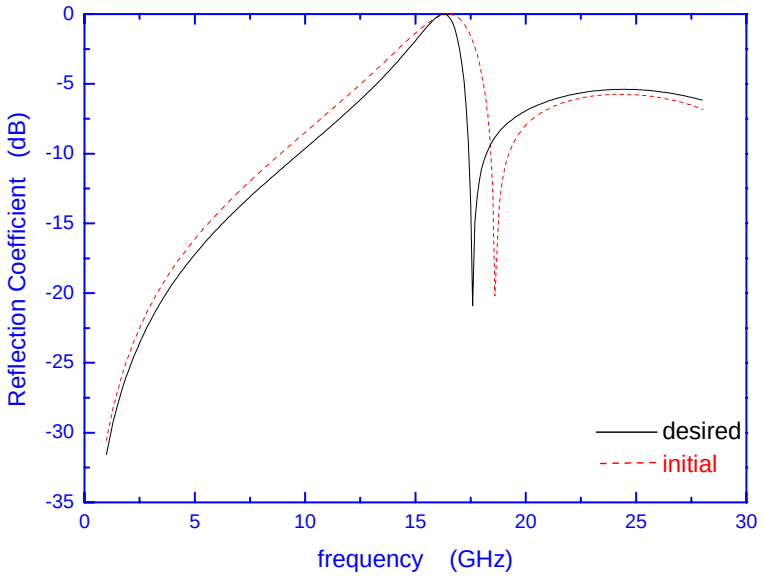

Figure 4-5 Frequency response of the initial generation and desired one in the design of a freestanding FSS using RGA

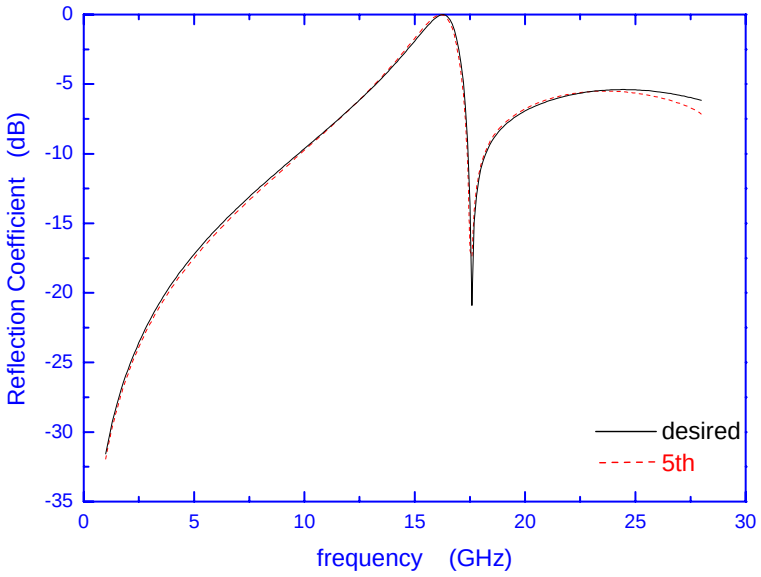

Figure 4-6 Frequency response of the 5th generation and desired one in the design of a freestanding FSS using RGA

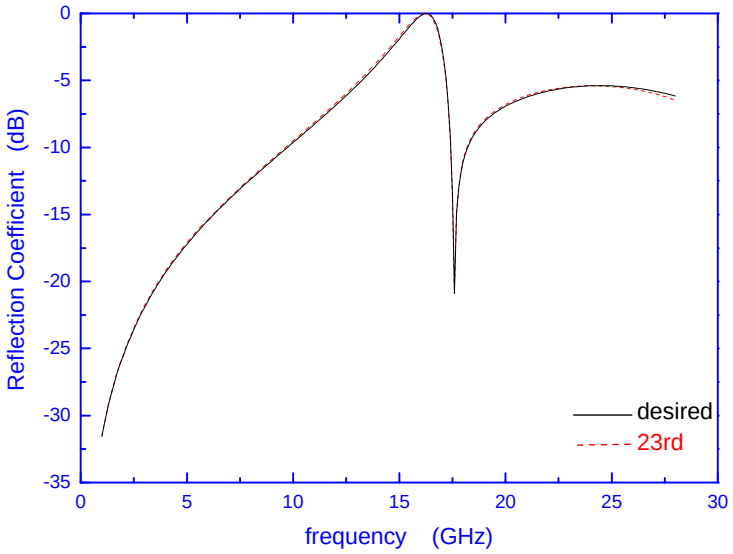

Figure 4-7 Frequency response of the 23rd generation and desired one in the design of a freestanding FSS using RGA

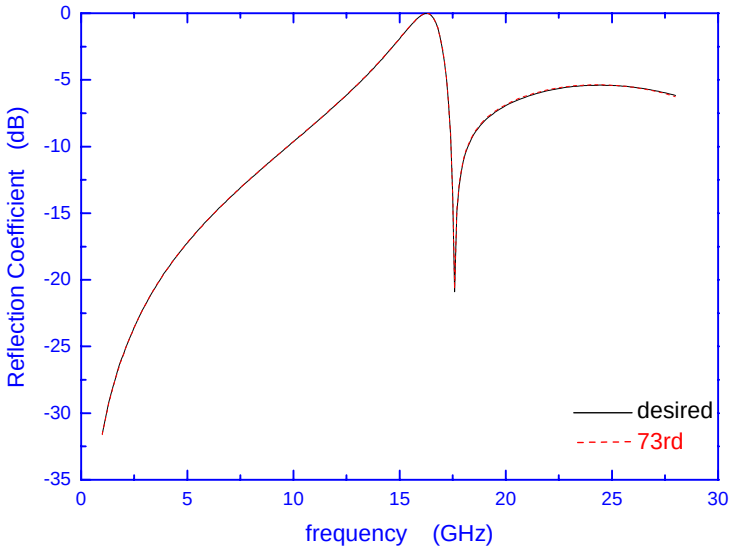

Figure 4-8 Frequency response of the last generation (73rd) and desired one in the design of a freestanding FSS using RGA

Table 4-1 The true values and the values of optimization parameters in the last generation

Optimization parameters of FSS	The true values	The values of the last generation (73^{rd})
The periodicity in x direction	10.0mm	10.03519mm
The periodicity in y direction	10.0mm	10.00931mm
The length of the dipole	7.5mm	7.51929mm
The width of the dipole	1.875mm	1.84659mm
The skewed angle	90^0	86.74^0

For comparison, the author also applied DES to design a freestanding dipole array with the same specification [85]. The frequency range considered is from 1 GHz to 30 GHz. The step size is 1GHz for the range of all frequencies except between 15 GHz and 18 GHz where 0.1 GHz step size is employed. The total number of test frequencies is 58. The optimization parameters are $N_{par} = 5$ and the population size is chosen to be $N_{pop} = 10 \times N_{par} = 50$. The optimization is terminated either after 200 generations or when $f(x) < 0.005$. The crossover probability and the mutation intensity are set to be $P_{cross} = 0.9$ and $P_{mut} = 0.7$ respectively. The search ranges of five optimization parameters are set as follows: $1mm \le a \le 20mm$, $1mm \le b \le 20mm$, $1mm \le L \le 15mm$, $0.1mm \le W \le 4mm$, $80^0 \le \Omega \le 100^0$.

The convergence behaviour of DES is shown in Figure 4-9 (solid curve). The program was terminated in the 36^{th} generation. The average time for each generation of evolution in DES simulation is about 45secs. The CPU time of the whole simulation process is 27minutes. The versatility of this proposed DES technique is evident. The synthesized

results at the initial, 15th and the last generation (36th) are compared and plotted as shown in Figure 4-10. The values of optimization parameters in the initial, 15th, 36th generations and the true values are compared and tabulated in Table 4-2. From the table, it can be observed that the values of the last generation are in very good agreement with the true values. For comparison, Figure 4-9 also combines the convergence behaviour of RGA shown in Figure 4-4. The reconstructed results obtained here further demonstrate the faster convergence of DES than RGA. The evidence comes from the fact that the true profiles are obtained with less generations, even with much larger search spaces.

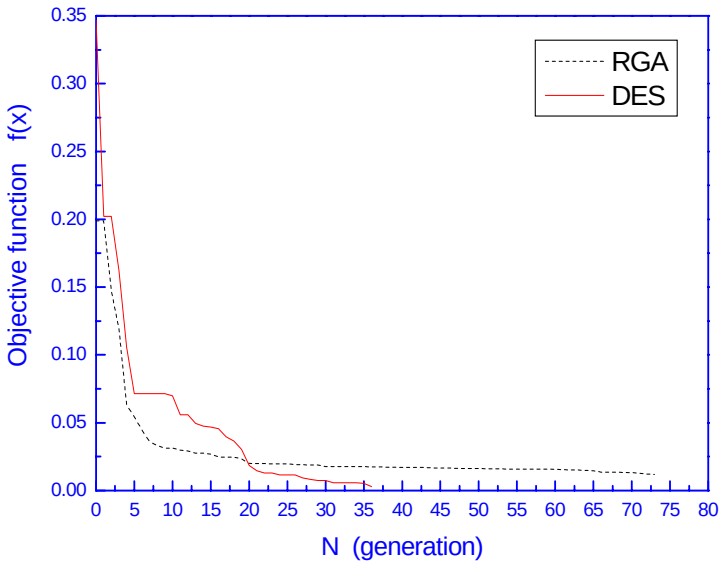

Figure 4-9 Comparison of convergence behaviour between the DES and RGA applied in the design of a freestanding FSS dipole array

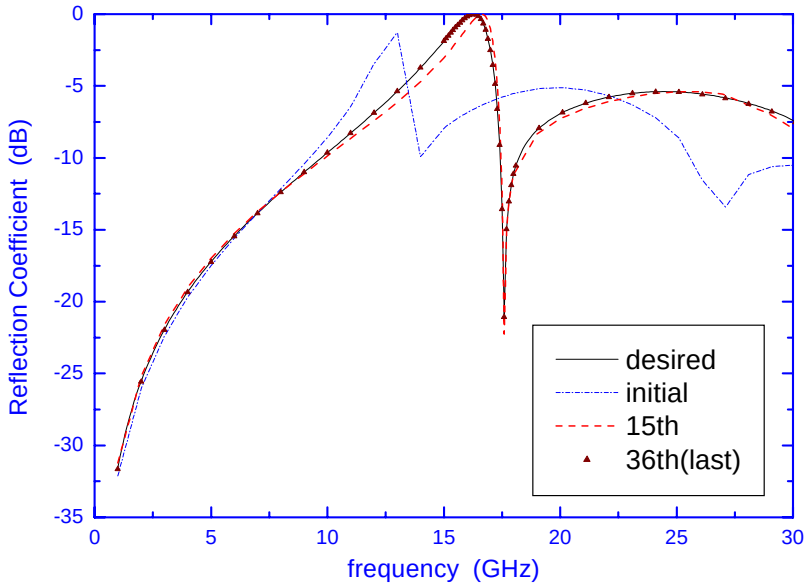

Figure 4-10 Comparison between the frequency response of the initial, 15th and 36th generation and desired one in the design of a freestanding FSS dipole array using DES

Table 4-2 The true values and the values of optimization parameters in the initial, 15th, and the last generation (36th) in the design of a freestanding FSS dipole array using DES

	True values	Initial Values	15th generation	Final Results (36th generation)
a	10.0mm	13.2mm	10.0mm	10.0mm
b	10.0mm	9.56mm	11.0mm	9.96mm
L	7.5mm	8.09mm	7.03mm	7.50mm
W	1.875mm	1.60mm	3.19mm	1.83mm
Ω	90^0	88.7^0	89^0	89.8^0

4.3.2.2 The Other Case for the Design of Freestanding FSS with Dipole Array

In this section, we will apply the above approach to synthesize a freestanding FSS with dipole elements. The design specifications call for the target [87]: $\mathbf{x} = [a, b, L, W, \Omega] = [17.8mm, 17.8mm, 12.7mm, 1.27mm, 90^0]$. Specifically, the incident wave is TM polarization wave, the angle of incidence is set as $\theta = 0.1^0$, $\phi = 90^0$ and the frequency range considered here is between 8 GHz and 16 GHz. The step size is 0.1 GHz and the total number of frequency points is 81. The search space is delimited as $\mathbf{x}^{\min} = [10mm,\ 10mm,\ 5mm,\ 0.1mm,\ 80^0]$ and $\mathbf{x}^{\max} = [25mm, 25mm, 15mm, 4mm, 100^0]$. The optimization parameters are $N_{par} = 5$ and the population size is chosen to be $N_{pop} = 8 \times N_{par} = 40$. The optimization is set to be terminated either after 200 generations or when $f(x) < 0.002$. The crossover probability and the mutation intensity are set as $P_{cross} = 0.9$ and $P_{mut} = 0.7$ respectively.

From these specifications, the objective function can be calculated by following the approach described in section 4.2. The evolution of the objective function during the optimization is depicted in Figure 4-11. The final population has clearly converged after 34 generations from the restart. The synthesized results are shown in Figure 4-12. The frequency characteristics of the last generation are matched closely to the prescribed curve. The values of optimization parameters obtained at the last generation are compared to the true values and the results are tabulated in Table 4-3. It can be seen that the computed results and true values are in close agreement. Each generation of evolution in DES simulation takes averagely about 2 minutes and 40 seconds. The CPU time of the whole simulation process for DES takes 1 hours and 31 minutes. This work was reported in [83].

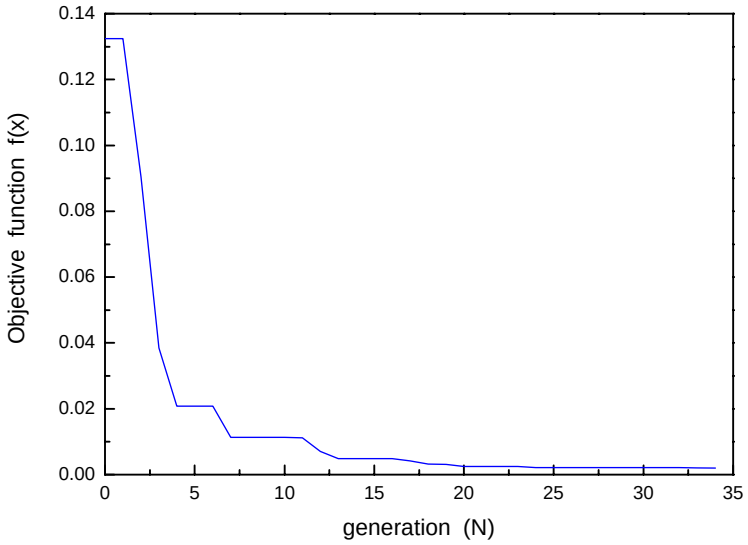

Figure 4-11Evolution of the objective function during DES optimization in the FSS design

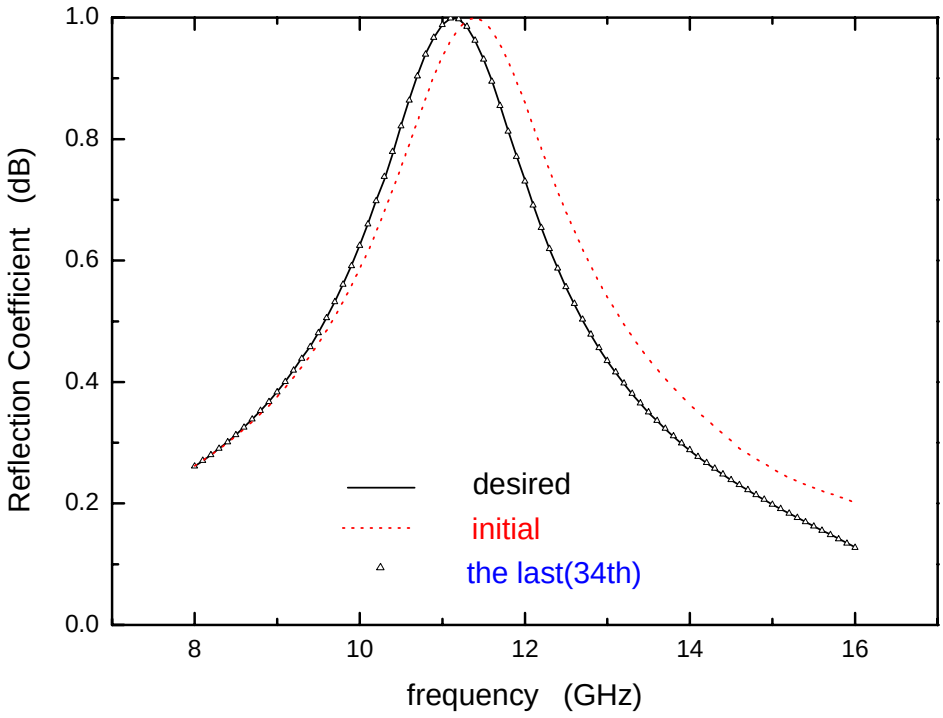

Figure 4-12 The synthesized results

Table 4-3 Comparison of the synthesized results

	True values	Initial values	Final Results
a	17.8mm	15.386mm	17.822mm
b	17.8mm	20.283mm	17.670mm
L	12.7mm	12.905mm	12.692mm
W	1.27mm	1.2958mm	1.2741mm
Ω	90^0	86.477^0	89.596^0

4.3.3 Design an FSS Dipole Array with Dielectric Substrate

The configuration parameters of the desired FSS are chosen from [88]: $\mathbf{x} = [a, b, L, W, \Omega, \varepsilon_r, t] = [6mm \quad 6mm \quad 4.15mm \quad 0.415mm \quad 90^o \quad 3.1 \quad 0.021mm]$. In that paper, the author proposed to use Schelkunoff's equation to study finite arrays of dipoles. Here, the spectral-domain MoM technique is used to validate the accuracy of the measurement from [88]. The design specifications are: the angle of incidence is set as $\theta = 5^o$, $\phi = 0^o$ and the frequency range considered here is between 25 GHz and 40 GHz. The step size is 0.2 GHz between 30 GHz and 35 GHz but is 1 GHz in other frequency range. In total, 36 test frequencies were used.

The optimization parameters are $N_{par} = 7$ and the population size is chosen to be $N_{pop} = 10 \times N_{par} = 70$. The optimization is set to be terminated either after 200 generations or when $f(x) < 0.003$. The crossover probability and the mutation intensity are set as $P_{cross} = 0.9$ and $P_{mut} = 0.7$ respectively. The search ranges of five optimization parameters

are set as follows: $1mm \le a \le 10mm$, $1mm \le b \le 10mm$, $1mm \le L \le 8mm$, $0.1mm \le W \le 1mm$, $80^0 \le \Omega \le 100^0$, $2.0 \le \varepsilon_r \le 4.0$, $0.01mm \le t \le 0.1mm$.

The objective function versus the generation number is shown in Figure 4-13. It indicates that the program achieves convergence after 29 generations. On average, each generation of evolution in DES simulation takes about 14 minutes. The CPU time of the whole simulation process for DES is about 6 hours and 46 minutes. The synthesized results shown in Figure 4-14 indicate that the curve at the last generation is very close to the prescribed one. The comparison of the values of optimization parameters in the initial generation, the last generation (29^{th}) and the true values are tabulated in Table 4-4. It can be observed from the table that the values of the last generation are in good agreement with the desired target. This work has been published in [85].

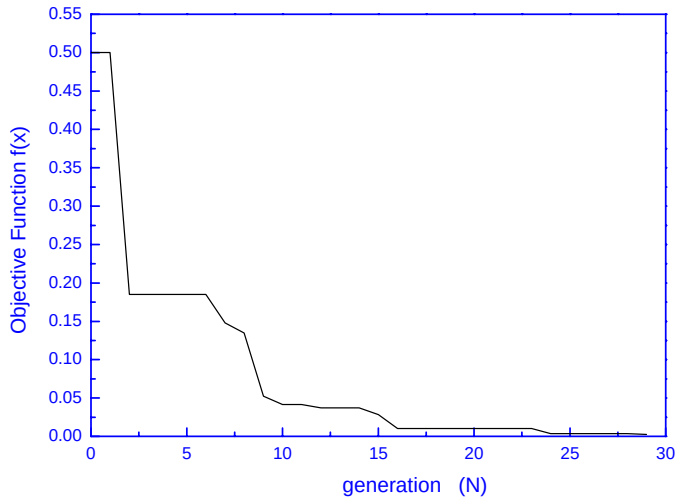

Figure 4-13 Convergence behaviour of DES applied in the design of an FSS dipole array with a dielectric substrate

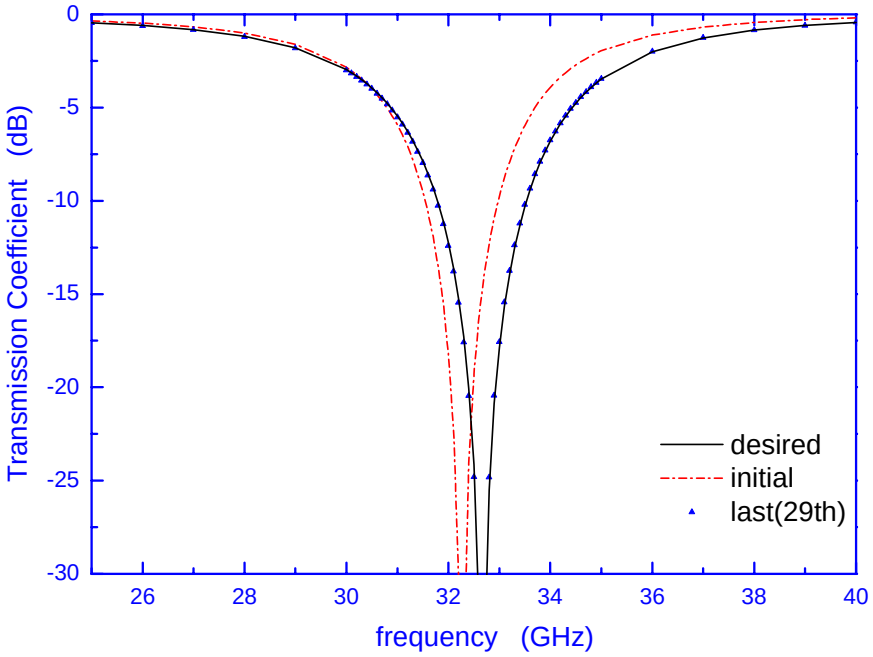

Figure 4-14 Comparison between the frequency response of the initial and 29th generation and desired one in the design of an FSS dipole array with a dielectric substrate

Table 4-4 The true values and the values of optimization parameters in the initial and the last generation (29th) in the design of an FSS dipole array with a dielectric substrate

	True values	Initial Values	Final Results (29th generation)
a	6.0mm	6.87mm	6.16mm
b	6.0mm	4.65mm	6.20mm
L	4.15mm	4.00mm	4.21mm
W	0.415mm	0.283mm	0.469mm
Ω	90^0	83.8^0	85.1^0
ε_r	3.1	2.25	2.74
t	0.021mm	0.011mm	0.018mm

4.4 Design of Multi-layered Frequency Selective Surfaces

In the previous section, the typical dipole array is firstly applied as optimization objective in the design of FSS structure with prescribed response. In this section, the multi-layered FSS structures are designed to obtain good band-pass or band-stop performance since they have broader bandwidths and close band centre spacing compared with the single layer FSS. The gangbuster array and hexagon array are chosen as optimization objective due to their superior bandwidth and stability to different incident angles and polarization. Hexagon array is strongly recommended in Munk's book [5] which indicated that the hexagon array is superior to the other loop element such as ring and square array because of its broadband bandwidth. The gangbuster array is used for wide-band filter design which is also recommended in Munk's book [5] for its good wide-band performance (faster roll-off). The arbitrarily desired bandwidth can be obtained by optimizing these two arrays.

The analysis of multi-layered FSS structures is described in Section 2.2. Here, the piecewise sinusoidal basis function for thin wire is employed to analyze the hexagon and gangbuster array instead of rooftop basis function. Its current in spacial domain is expressed as Eq. (2-23).

It is usually the greatest challenge to design band-pass or band-stop filters with large bandwidth. The narrow-band design is relatively easier to determine once a large bandwidth is mastered. Several designs are described here. Firstly, a hexagon array for the narrow-band application of GSM, GPS and 3G communication is designed. Then, the band-stop and band-pass filter with wide bandwidth are designed to demonstrate the efficiency of the proposed method.

4.4.1 Design of Band-pass FSS with Hexagon Array for Mobile Communication

The typical hexagon array consists of six-arms is shown in Figure 4-15 (a), where l is the length of hexagon arm, W is the width of the arm and g is the gap between the hexagon elements. P_a and P_b are the periodicity in the x and y direction respectively. Figure 4-15 (b) shows an FSS structure which include one hexagon array embedded in two dielectric layers and whose parameters that to be optimized with a view to realizing a specified frequency response. The objective here is to design an FSS structure to reject the signal at the frequency band of GSM that operates in 900MHz, 1800MHz and 1900MHz, Global Positioning System (GPS) working around 1500MHz and 3G operating around 2GHz. FSS hexagon array is designed to provide the required band-stop bandwidth ranging from 900MHz to 2GHz.

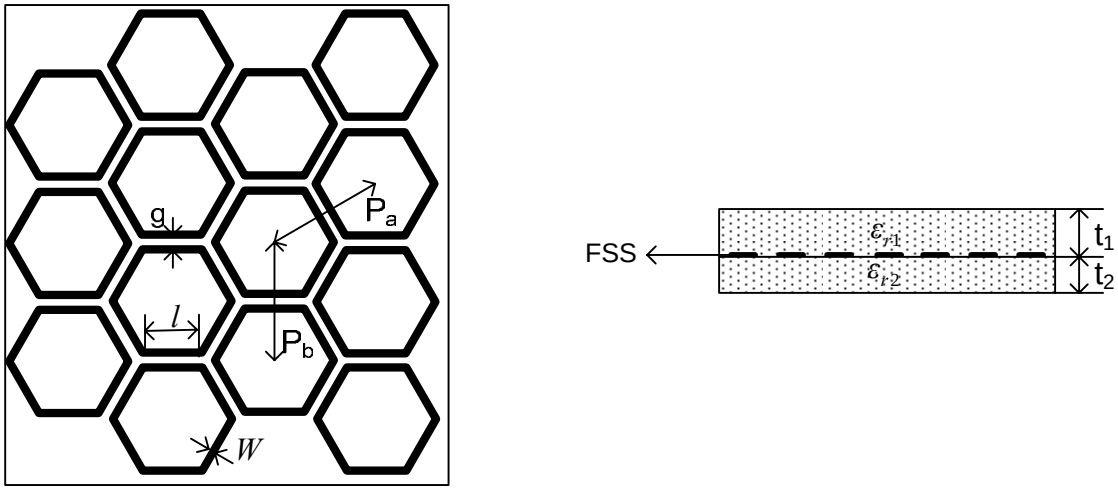

(a) (b)

Figure 4-15 (a) Hexagon array (b) One FSS screen embedded in two dielectric layers.

At the first step, determine the optimization parameters which will be tuned. To simplify the design, we take $\varepsilon_{r1} = \varepsilon_{r2}$ and W=0.1mm (thin wire). The length of hexagon arm l, the gap between elements g, the dielectric constant ε_r and the thickness of mediums t_1 and t_2 are taken as optimization parameters. Therefore, the configuration parameters of the hexagon array are $x = [l, g, \varepsilon_r, t_1, t_2]$ and $N_{par} = 5$.

In DES, the search parameters are set to be $P_{cross} = 0.9$ and $P_{mut} = 0.7$. The population size is set as $N_{pop} = 30$. The search range of the optimization parameters is set as $10.0mm \le l \le 30mm$, $0 < g \le 7.0mm$, $1.0 < \varepsilon_r \le 8.0$, $0 < t_1 \le 5.0mm$, $0 < t_2 \le 5.0mm$. The frequency is set in the range of 0.5 GHz to 3 GHz with the step size of 0.1 GHz which includes 26 frequency points.

The program is terminated after about 12 hours. The optimization parameters obtained are $x = [l, g, \varepsilon_r, t_1, t_2] = [20.41mm, 4.02mm, 3.5, 4.21mm, 5.20mm]$. The reflection frequency response at normal incidence is analyzed as shown in Figure 4-16. It is observed that the band-stop performance is obtained between 0.9 GHz and 2.0 GHz where the reflection coefficient is greater than 0.5dB which satisfy the desired frequency response. This is a very practical and important application with an increasing demand on wireless communication. If the band-pass performance at this frequency band is required (i.e. passing through the signal at the frequency band between 0.9 GHz and 2.0 GHz), an aperture hexagon array with the similar dimensions may be utilized to realize the complementary performance. This example is the narrow-band application for hexagon array. However, the advantage of the hexagon array is its broad-band application.

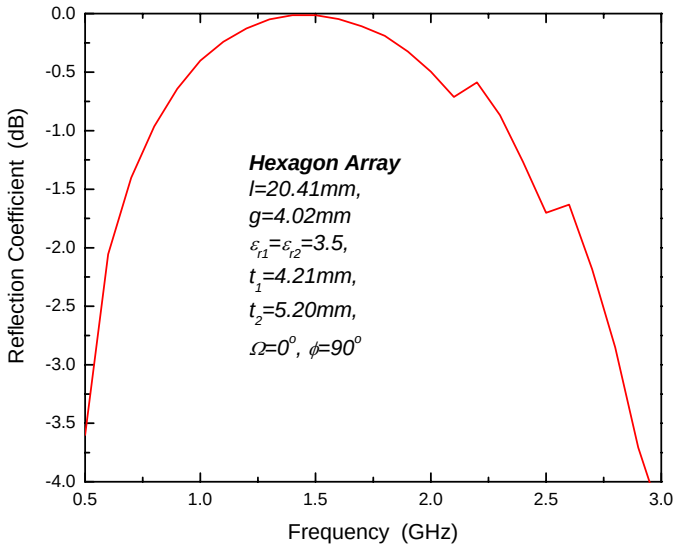

Figure 4-16 Hexagon array applied in the GSM, GPS and 3G communication

4.4.2 Design of Wide-band Band-stop Filter with Hexagon Array

The design of a band-stop filter takes the hexagon array as optimization objective. An FSS structure with two hexagon arrays embedded in the three dielectric layers are shown in Figure 4-17. The aim of this design is to obtain a band-stop filter with stop-band between 9.4 GHz and 17 GHz at normal incidence ($\theta = 0^0$). The reflection response at stop-band is greater than -0.5dB. Stable response with respect to the incident angle and polarization is required.

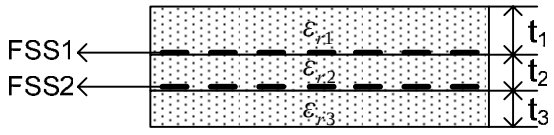

Figure 4-17 Two FSS screens embedded in three dielectric layers.

Here, $\varepsilon_{r1} = \varepsilon_{r2} = \varepsilon_{r3}$ is taken and W=0.1mm (thin wire). The configuration parameters for this design are $x = [l, g, \varepsilon_r, t_1, t_2, t_3]$ and $N_{par} = 6$. The desired ideal frequency response of the band-stop filter is shown in Figure 4-18. The objective function is mathematically defined as

$$f(x) = \sum_{freq=9.4}^{17} \left| [\mathbf{R}(x)]_{freq} + 0.5 \right| \tag{4-6}$$

Where *freq* is the frequency point in stop-band.

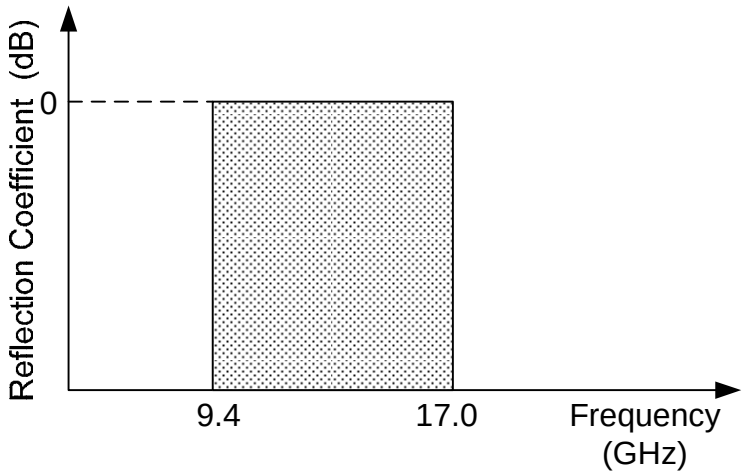

Figure 4-18 The frequency response of desired ideal band-stop filter

The search parameters in DES are set to be $P_{cross} = 0.9$ and $P_{mut} = 0.7$. The population size is set as $N_{pop} = 35$. The search range of the six optimization parameters is set as $2.0mm \le l \le 8mm$, $0 < g \le 1mm$, $1.0 < \varepsilon_r \le 6.0$, $0 < t_1 \le 2.0mm$, $0 < t_2 \le 2.0mm$, $0 < t_3 \le 2.0mm$. The frequency range is set as between 8GHz and 20GHz with the step size of 0.5 GHz which includes 25 frequency points.

The optimum results were obtained after about 4 hours. The optimized dimensions are shown in Table 4-5. Figure 4-19 shows the reflection coefficient of obtained hexagon array. Very good band-stop performance is obtained between 9.4 GHz and 17.0 GHz (flat stop-band and faster roll-off). Due to the symmetry of hexagon element, there is no significant difference between the reflection response at TE normal incidence and TM normal incidence (dash line) as shown in Figure 4-19. The reflection coefficient at TE 30^0 and TE 45^0 incidence is shown in Figure 4-20. It is observed that the hexagon array has the stable frequency response with respect to oblique angle of incidence. The TE transmission coefficient at normal incidence of the attained hexagon array which readings are less than -20dB at stop-band is also obtained and shown in Figure 4-20. This performance further illustrates that it is a good band-stop filter design.

In the design of band-stop filter, it is more feasible and practical to optimize the hexagon array by defining an arbitrary bandwidth instead of trail-and-error procedure. Very wideband stop-band (greater than 10GHz) with good performance can be realized by designing a hexagon array using our proposed method.

Table 4-5 Attained dimensions of optimization parameters

l	g	ε_r	t_1	t_2	t_3
3.825mm	0.101mm	2.2	0.645mm	1.836mm	0.602mm

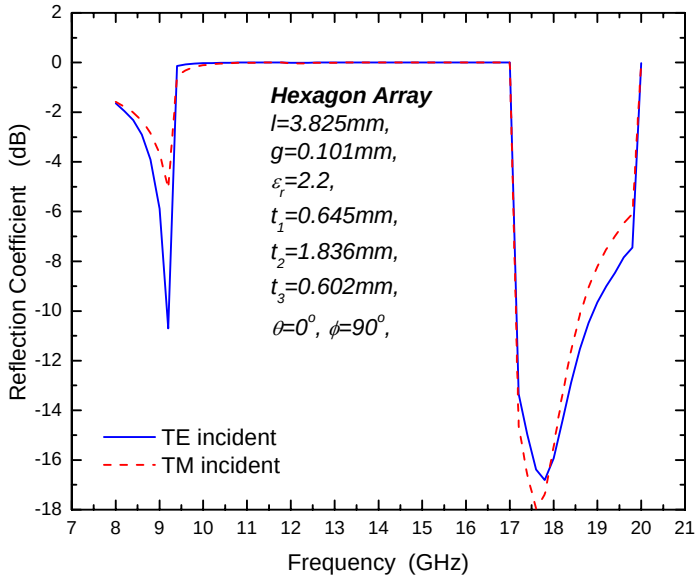

Figure 4-19 The reflection frequency response of attained hexagon array at TE and TM normal incidence.

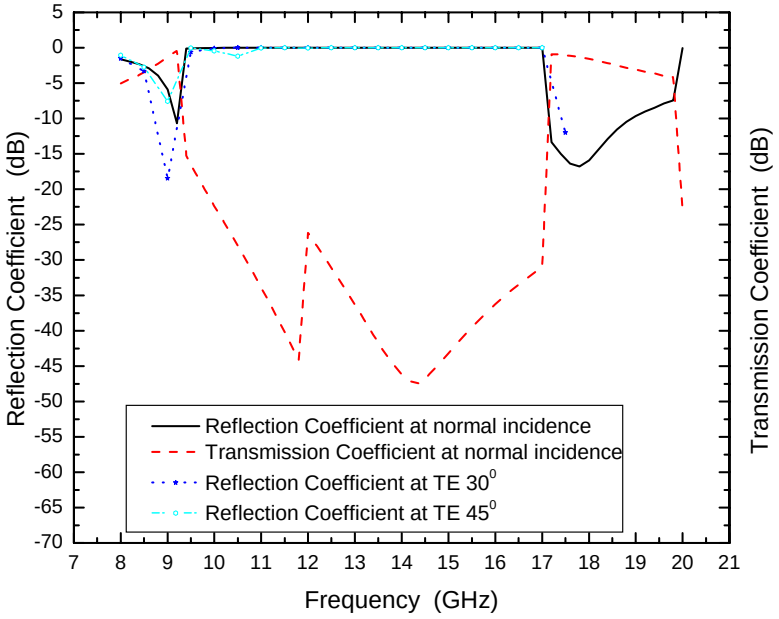

Figure 4-20 The reflection frequency response at the different incident angle and the transmission frequency response at normal incidence of attained hexagon array

4.4.3 Design of Multi-layered Band-pass Filter with Gangbuster Array

The typical gangbuster array is composed of simple straight dipoles arrayed in a fashion as shown in Figure 4-21. A single gangbuster surface can only handle linear polarization with the E-field being in the plane of the elements [5]. However, arbitrary polarization can easily be handled if we use two gangbuster surfaces twisted 90^0 with respect to each other. In our design presented here, the configuration of two twisted gangbuster arrays with three dielectric layers as shown in Figure 4-17 are selected as optimization objective.

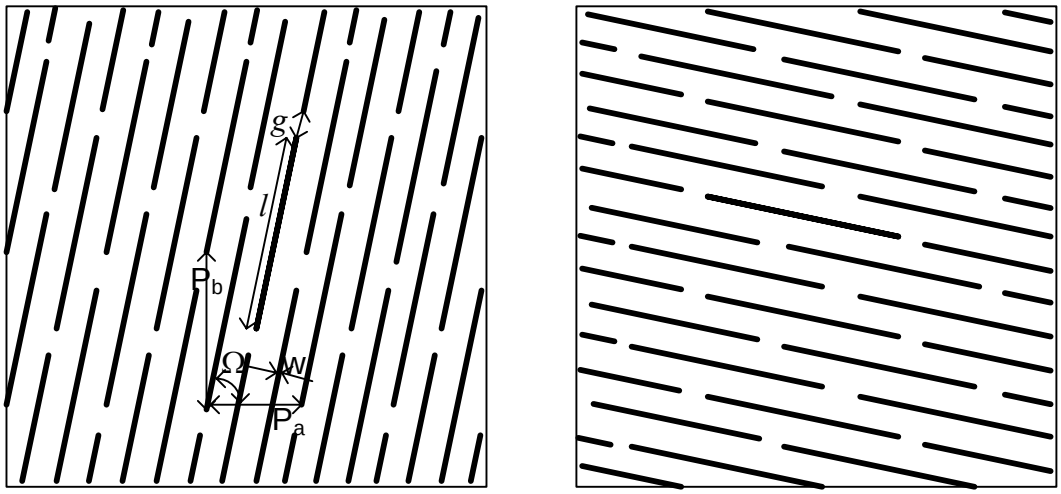

(a) (b)

Figure 4-21 Two Gangbuster arrays twisted 90^0 (a) FSS1 (b) FSS2

The design specifications are that of the pass-band between 14GHz-28GHz, normal TE incident wave and the pass-band transmission coefficient better than -0.5dB. The desired ideal frequency response of the band-pass filter is shown in Figure 4-22. The objective function is mathematically defined as

$$f(x) = \sum_{freq=14}^{28} \left| [\mathbf{T}(x)]_{freq} + 0.5 \right| \tag{4-7}$$

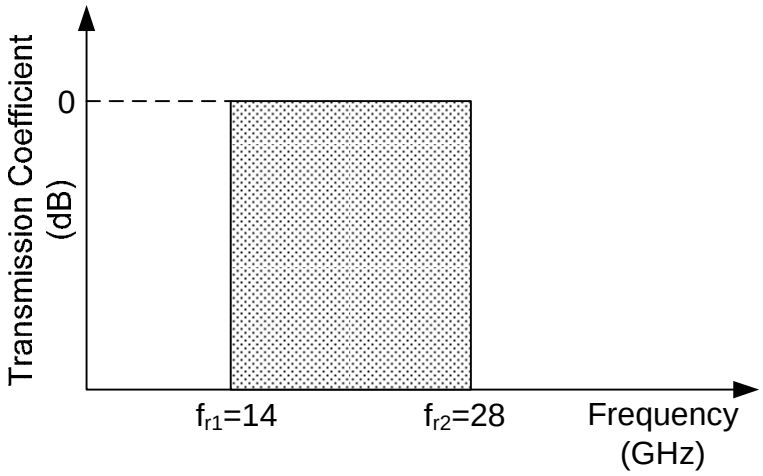

Figure 4-22 The frequency response of desired ideal band-pass filter

From the Figure 4-21 and Figure 4-17, the optimization parameters array are determined as $\mathbf{x} = [x_1, \cdots, x_7] = [l, g, \Omega, \varepsilon_r, t_1, t_2, t_3]$. Table 4-6 shows the definition and the search range for these seven optimization parameters. In DES, the search parameters are set to be $P_{cross} = 0.9$ and $P_{mut} = 0.7$. The population size is set as $N_{pop} = 35$. The frequency is set in the range of 10 GHz to 30 GHz with the step size of 0.5 GHz which includes 41 frequency points.

The program is terminated after two generations where the minimum objective function is obtained. The optimized parameters dimensions are tabulated in Table 4-6. The transmission and reflection frequency responses are shown in Figure 4-23. The flat transmission band (greater than -0.5dB) is obtained between 14.4 GHz and 18.4 GHz. Good reflection frequency response performance is observed at pass-band (less than -20dB). The transmission frequency response of attained band-pass filter with gangbuster

array at different incident angle is shown in Figure 4-24. It is observed that the frequency response of designed gangbuster array is insensitive with respect to oblique incident angles and is very suitable for broad-band application.

Table 4-6 Search range and optimized results for optimization parameters

Optimization parameters	Search range	Optimization results
Dipole length (l)	$4.0mm \le x_1 \le 25.0mm$	$x_1 = 8.89mm$
Gap between inter-dipole (g)	$0 \le x_2 \le 2.0mm$	$x_2 = 0.623mm$
Skewed angle (Ω)	$0 \le x_3 \le 90^0$	$x_3 = 45.5^0$
Dielectric constant ($\varepsilon_{r1} = \varepsilon_{r2} = \varepsilon_{r3}$)	$1.0 \le x_4 \le 6.0$	$x_4 = 2.51$
Thickness for dielectric 1 (t_1)	$0 \le x_5 \le 2.0mm$	$x_5 = 1.69mm$
Thickness for dielectric 2 (t_2)	$0 \le x_6 \le 2.0mm$	$x_6 = 0.214mm$
Thickness for dielectric 3 (t_3)	$0 \le x_7 \le 2.0mm$	$x_7 = 1.64mm$

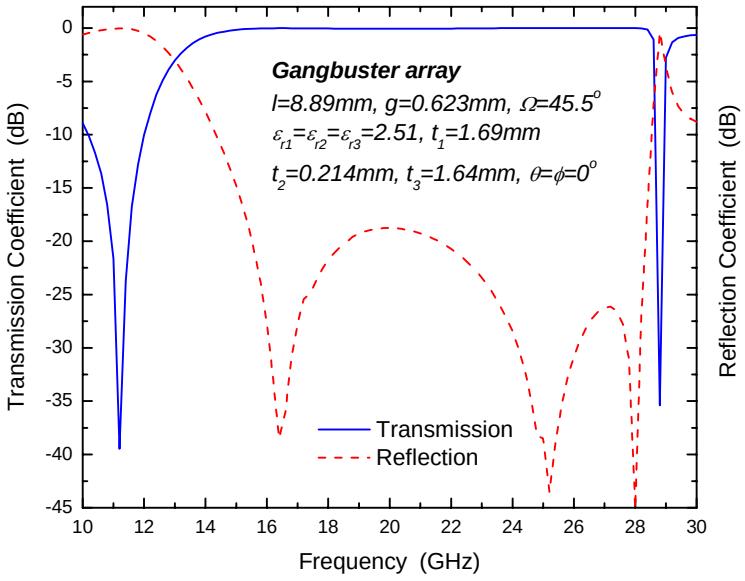

Figure 4-23 The frequency response of attained band-pass filter with gangbuster array at normal incidence.

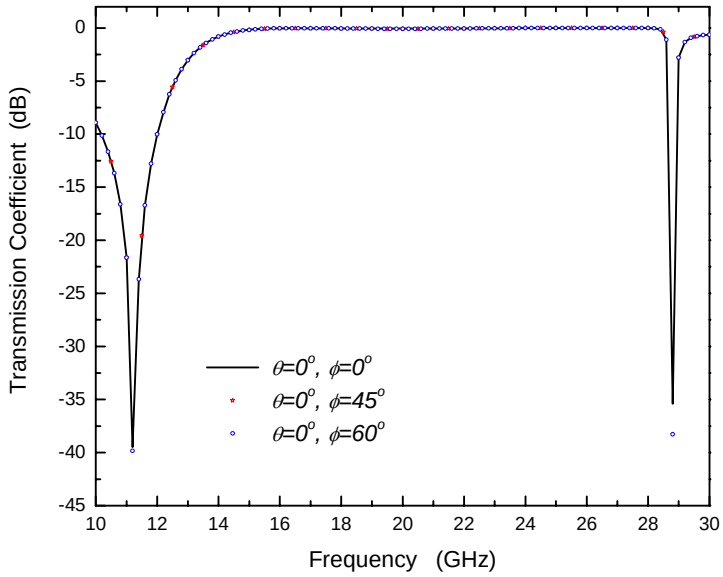

Figure 4-24 The transmission frequency response of attained band-pass filter with gangbuster array at different incident angle.

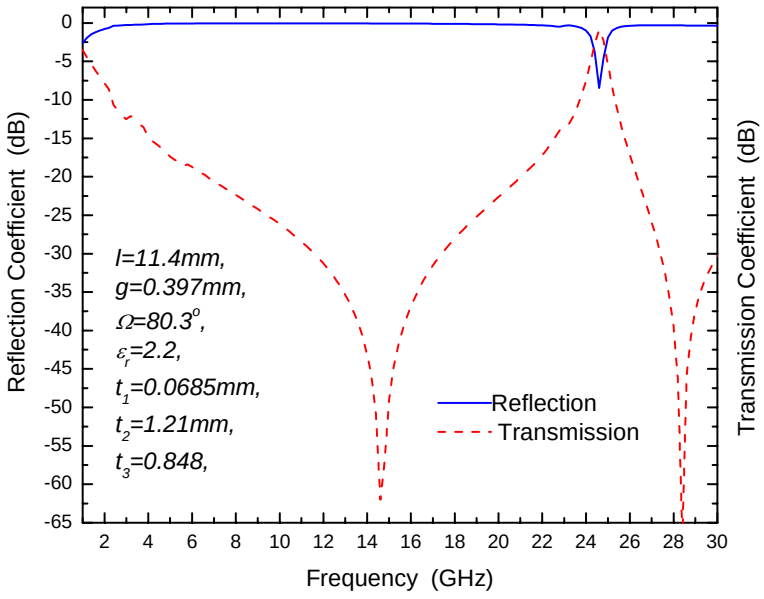

Figure 4-25 Band-stop filter with gangbuster array at normal incidence.

The gangbuster array also can be used to design band-stop filter with wide-band bandwidth. Figure 4-25 shows a gangbuster array with the stop-band between 2-24GHz. Good band-stop performance is observed.

The gangbuster array with two screens twisted 90^0 has stable frequency response with respect to the incident angle and polarization. The band-stop or band-pass filter with arbitrary bandwidth can be obtained using DES optimization without tedious trail-and-error procedure.

4.5 Conclusions

A novel design method using DES coupled with spectral-domain MoM is proposed in this chapter for the design of FSS with prescribed frequency response. DES is employed to optimize the standard, non-irregular geometries of FSS unit cell and dielectric properties. The analysis of frequency response of FSS screen is solved by employing the spectral-domain MoM technique.

The design process of FSS using optimization method is presented. The objective function is defined here as the relative error between the actual and prescribed frequency response. Thus, the problem of FSS design is cast into an optimization problem by minimizing the relative error function of frequency response affected by the optimization parameters.

The synthetic construction of an FSS dipole array with and without substrates is created as optimization objective. The entire-domain basis function in spectral domain for dipole array is derived. The synthesized results obtained for freestanding FSS (without

substrates) are in good agreement with the true profiles. In order to further validate the predominance of DES, RGA is applied to the same design construction for comparison. From the comparison, DES displays the faster convergence than RGA. Overall, the results demonstrate that DES is a more efficient and more robust method in the design of FSS. In the design of FSS dipole array with substrates, the reconstructed results display that the curve and the parameters values at the last generation, which is produced by the proposed method, is very close to the prescribed target. The results illustrate the capability of DES as optimization tool in the design of FSS.

The multi-layered hexagon array and gangbuster array are taken as optimization objective to realize the band-stop and band-pass filter design. The first application is to design a hexagon array which can reject the signal at the frequency band of GSM, GPS and 3G communication. The aperture hexagon array can be used to realize the band-pass performance at the same frequency band. The second application of the hexagon array is to obtain very broad-band band-stop filter. The good stability of frequency response with respect to the incident angle is demonstrated. The last two applications are to design wide-band band-pass and band-stop filter using two gangbuster arrays twisted together. Good pass-band and stop-band (flat band and faster roll-off) are obtained using this FSS structure. The arbitrary bandwidth can be obtained by the optimization setting using our proposed method. The tedious trail-and-error procedure is avoided. The advantage of optimization method is exhibited.

Chapter 5 Design of Multi-Band Frequency Selective Surfaces Using Differential Evolution Strategy Combined with Equivalent Circuit Model

5.1 Introduction

Multi-band FSS have been used as space filters in both commercial and military sectors. For example, the NASA's CASSINI's sub-reflectors were made of an FSS with double-square elements for multiplexing in S, X, Ku and Ka bands [89]. Lee and Langley designed an FSS with gridded-square elements to be used in a dual frequency band satellite antenna [51]. However, their designs are typically based on a trial-and-error process to synthesize an FSS array with a desired frequency response. The optimization technique, DES has been proposed to apply in the design of FSS in order to avoid tedious trial and error procedure in previous chapter. In this chapter, the DES is still employed as optimization tool to design multi-band FSS structures with prescribed performance objectives and constraints. The double-square, gridded-square and gridded-double-square

arrays are selected as optimization objective since their performances are relatively insensitive to the angle of incident wave. For FSS array composed of double-square, gridded-square and gridded-double-square elements, their frequency responses have been accurately analyzed using the ECM technique which has been tested through experiments [12-13, 31-32, 50-51]. Compared to the MoM technique, ECM exhibits rapidly computational time and can provide a fast solution to a design. Therefore, ECM is employed as analytical method in the design of multi-band FSS structures with double-square, gridded-square and gridded-double-square elements respectively in this chapter. The formulations of ECM applied to analyze the frequency response of FSS screen have been included in Chapter 2.3.

The objective in this chapter is to design FSS structures for multi-band applications. A novel method using DES combined with ECM is proposed. DES is employed to tune the FSS unit cell while ECM is used to analyze the transmission response from FSS screen. Six multi-band FSS design examples are conducted to demonstrate the efficiency of this method. Compared with other researchers design [12, 32, 51, 89], which is to search in the knowledge base through a trial-and-error process to synthesis an FSS array, the optimization algorithm DES can automatically seek and find the optimum configuration objective in very short time effectively. Single layer FSS structure is selected because it is more attractive than multi-layered FSS in the complexity of fabrication and alignment applications.

Section 5.2 presents the design process of FSS using DES combined with ECM. The objective function is redefined which is relevant with the performance of pass-band and stop-band. Designs of gridded-square array (Section 5.3), gridded-double-square array

(Section 5.4) and double-square array (Section 5.5 and 5.6) are enumerated to demonstrate the efficiency of the proposed method. The reason of choosing these arrays is to validate the proposed DES (optimization) cum ECM (analysis) method with some reported measurement results. One of the designs for gridded-square array operating in low-frequency region was fabricated on a low-cost glass-epoxy substrate for preliminary study of satellite program at the university. Finally, a designed triple-band double-square FSS array was also manufactured on a Mylar substrate.

The proposed method was program-coded in FORTRAN and carried out on NEC P-IV-2.4 GHz PC. The software is FORTRAN POWERSTATION 4.0 under WINDOWS 2000. The CPU processor time for solving each studied problems varied from a few seconds to up to 1.5 minutes. The relatively short time is due to the fast convergence performance of DES and the fast computation speed of ECM.

5.2 Design Process of FSS Using DES Combined with ECM

The flow chart of FSS design process given in chapter 4.2 is still applicable here. The difference is that the frequency characteristics of FSS screen are computed from the ECM technique instead of MoM. Furthermore, the definition of objective function is different from that of MoM. For gridded-square, gridded-double-square and double-square arrays, which are taken as optimization objective in the design examples, the equivalent circuits and the corresponding computation of circuit components impedances are also presented. The transmission response from FSS screen can be obtained after combining with the formulations in Chapter 2.3.

According to the optimization flow chart presented in Figure 4-1, given the range of optimization parameters of FSS unit-cell, DES iteratively constructs a composite whose frequency response closely matches the desired response. An important step in the design procedure is to choose parameters to control the optimization procedure. The optimization goal is to minimize the objective function $f(x)$ and find a feasible optimization vector x composed of N_{par} parameters.

5.2.1 Definition of Objective Function

The performance of an FSS is characterized by three main factors: the bandwidths of the transmission band or reflection band, the –0.5dB or -10dB band-edge ratio (the roll-off rate) and the stability of the transmission response to oblique angle of incidence. Thus, the objective function of the problem can be mathematically described as

$$f(\mathbf{x}) = A\left\{\sum_{i=1}^{M}\left|\left[\mathbf{T}(\mathbf{x})\right]_i + 0.5\right|\right\} + B\left\{\sum_{j=1}^{N}\left|\left[\mathbf{T}(\mathbf{x})\right]_j + 10\right|\right\} \tag{5-1}$$

where M is the total number of test frequencies in pass band and N is the total number of test frequencies in stop band. $\mathbf{T}$ is the computed transmission coefficients vectors. The bandwidths are normally defined by the –10dB level in reflection, and –0.5dB level in transmission. A and B are additional weighting coefficients. When $\mathbf{T}(\mathbf{x}) \geq -0.5dB$ in pass-band, $A = 0$. $B = 0$ when $\mathbf{T}(\mathbf{x}) \leq -10dB$ in stop-band. Otherwise, $A = 1,\ B = 1$.

5.3 Design of Dual-Band FSS with Gridded-Square Elements

5.3.1 Formulations of Components Impedances

The geometry and the equivalent circuit model for gridded-square array are shown in Figure 5-1T, where a single inductance L_1 represents the grid, and a series resonant circuit L_2 and C_2 represents the square.

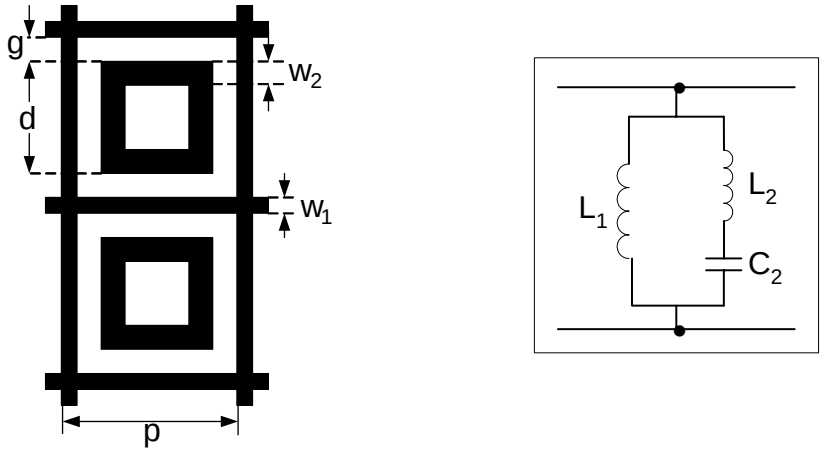

(a) (b)

Figure 5-1 Gridded-square array (a) geometry (b) equivalent circuit

The normalized admittance Y of an array at oblique incidence can be calculated according to the equivalent circuit. For narrow-band ($f_r / f_T \le 1.6$, where f_r is the resonant frequency and f_T is the center frequency of transmission band) gridded-square array, the impedances of these components are given as [32]

$$X_1 = \omega L_1 = F(p, w_1, \lambda) \tag{5-2}$$

$$X_s = F(p, 2w_2, \lambda) \times d / p$$

$$X_2 = \omega L_2 = 2.0 \times \frac{X_1 \times X_s}{X_1 + X_s} \tag{5-3}$$

$$B_2 = \omega C_2 = 2.0 \times \varepsilon_{reff} \times F(p, g, \lambda) \times d/p \tag{5-4}$$

For wide-band ($f_r / f_T > 1.6$) gridded-square array, the impedances of these components are given as [13]

$$X_1 = \omega L_1 = F(p, w_1, \lambda) \tag{5-5}$$

$$N = \begin{cases} 1.6 & at\ normal\ incidence \\ 1.7966 & at\ TE\,45^0 \\ 1.9480 & at\ TM\,45^0 \end{cases}$$

$$X_s = F(p, 2.5w_2, \lambda) \times d/p$$

$$X_2 = \omega L_2 = N \times \frac{X_1 \times X_s}{X_1 + X_s} \tag{5-6}$$

$$B_2 = \omega C_2 = 2.5 \times \varepsilon_{reff} \times F(p, g, \lambda) \times d/p \tag{5-7}$$

$$Y = j\left[\left(-\frac{1}{X_1}\right) + \left(\frac{B_2}{1 - X_2 \times B_2}\right)\right] \tag{5-8}$$

For very thin substrate or freestanding FSS, the effect of the supporting substrate is included in simple equivalent circuit model by incorporating an effective dielectric constant ε_{reff} in the calculation of susceptances [31]. The factor F, which stands for the normalized inductances or capacitances of the strip grating, can be calculated according to (2-82)-(2-85). The transmission coefficient T of the array is determined from (2-89).

5.3.2 Design of a Narrow-Band Gridded-Square Array

This design is the application of FSS to a dual frequency band reflector. The design problem involves creating an FSS array with the transmission band centered at 15.3 GHz and the reflection band at 23.1 GHz. The frequency band centers are spaced by a factor of 1.51. The original design and measured results were reported in [32]. The arrays were printed on very thin, 0.027mm polyester substrate. $\varepsilon_{reff} = 1.12$ was taken for ECM calculation.

Referring to Figure 5-1, the configuration parameters of gridded-square array are $x = [p, w1, w2, g]$. In DES, the search parameters are set to be $P_{cross} = 0.9$ and $P_{mut} = 0.7$. The population size is set as $N_{pop} = 10 \times N_{par} = 40$. The frequency range is taken from 10 GHz to 30 GHz with the step size of 0.1 GHz. The upper limit for the periodicity is determined by the onset of grating lobes. It can be avoided by ensuring $\lambda < p(1+\sin\theta)$, where λ is the wavelength and θ is the maximum angle of incidence. In this design, the highest frequency of interest is 30 GHz. Thus, the periodicity p must be less than 5.9 mm for the angle of 45^0 incidence. The lower limit for optimization parameters is determined by manufacturing tolerances. The search range of the four optimization parameters is set as $3.0mm \le p \le 5.9mm$, $0.1mm \le w1 \le 1.0mm$, $0.1mm \le w2 \le 1.0mm$, $0.1mm \le g \le 1.0mm$.

For a given frequency response, there exists an infinite number of combinations of dimensions. Table 5-1 tabulates five results produced by DES optimization for this specification. The maximum evolution generations for DES convergence and the CPU ruing time of the program are also presented. It is observed that the calculated band center

frequencies (transmission band and reflection band) at normal incidence for this five arrays are very close to the specified $f_T = 15.3\,GHz$ and $f_r = 23.1\,GHz$. The attained band spacing ratio f_r / f_T is close to 1.51, which also satisfies the design requirements. Furthermore, it is also observed that the dimensions of the configuration parameters can be obtained in a very short CPU computational time (<11 secs).

Table 5-1 Attained dimensions of optimization parameters and calculated band centers for gridded-square array at normal incidence

Array	Dimensions (mm)				f_T (GHz)	f_r (GHz)	f_r / f_T	Genera-tions	CPU time (secs)
	p	w_1	w_2	g					
1	5.05	0.137	0.155	0.609	15.2	23.1	1.52	3	0.72
2	5.13	0.278	0.263	0.466	15.3	23.0	1.5	26	6.6
3	5.81	0.728	0.573	0.362	15.3	23.0	1.5	21	4.7
4	4.76	0.211	0.201	0.409	15.4	23.1	1.5	2	0.7
5	4.97	0.443	0.354	0.286	15.4	23.0	1.49	30	10.2

The dimensions of array 1 in Table 5-1 are very close to that of array 3 presented in [32], which configuration dimensions (in mm) are $\{p, w_1, w_2, g\} = \{5.05, 0.15, 0.15, 0.6\}$. The calculated transmission responses at normal incidence for these two arrays are compared as shown in Figure 5-2. Obviously, good agreements are observed. There exists the measured results for array 3 in [32]. Their band centers at normal incidence, 45^0 TE incidence and 45^0 TM incidence are summarized in Table 5-2. For array 1, the transmission band at normal incidence is centered at 15.2 GHz (f_T) and the reflection band is centered at 23.1 GHz (f_r), giving a band spacing ratio of 1.52. The band center of

transmission band moves down by only 0.1 GHz from normal incidence to 45^0 incidence while a 0.5 GHz shift down in frequency occurs for the reflection band. Figure 5-3 shows the comparison between the simulated (array 1) and the measured (array 3 in [32]) transmission responses at normal incidence. Their comparison of transmission responses at TE 45^0 and TM 45^0 incidence are presented in Figure 5-4. Overall results show that f_T and f_r for array 1 are relatively stable with respect to the variation of incident angles.

In summary, this design demonstrates the efficiency of the proposed method (DES cum ECM). Compared with the synthesis design in [32] (trial and error procedure), the required configuration parameters can be easily obtained with the set search range of optimization parameters and the defined objective function for special problem in very short computational time.

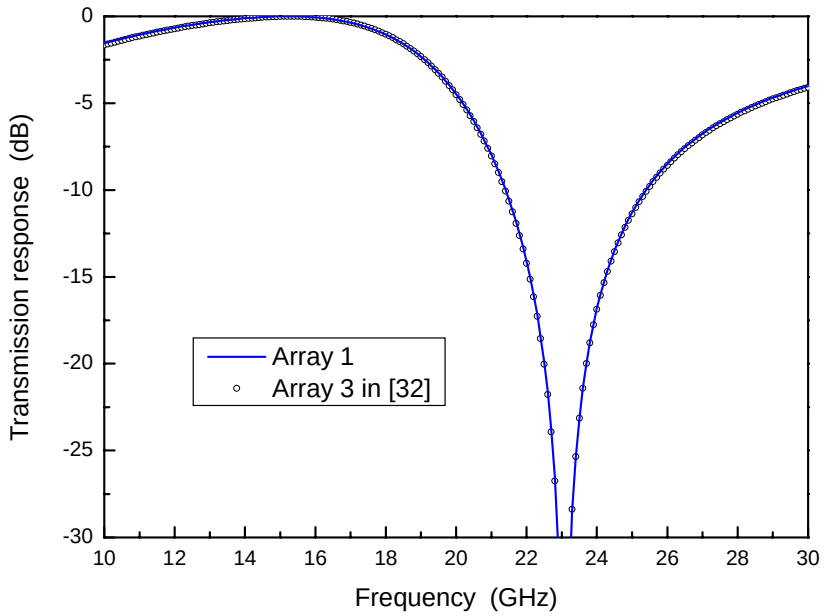

Figure 5-2 Simulated transmission responses for array 1 and array 3 in [32] at normal incidence

Table 5-2 Band centers of array 1 and array 3 in [32] for gridded-square array

	Transmission band center frequency f_T (GHz)			Reflection band center frequency f_r (GHz)		
	Array 1	Array 3 in [32]		Array 1	Array 3 in [32]	
	Simulated	Simulated	Measured	Simulated	Simulated	Measured
Normal incidence	15.2	15.3	15.3	23.1	23.1	23.1
45^0 TE incidence	15.2	15.3	16.0	22.8	22.8	22.7
45^0 TM incidence	15.1	15.2	15.8	22.6	22.6	22.8

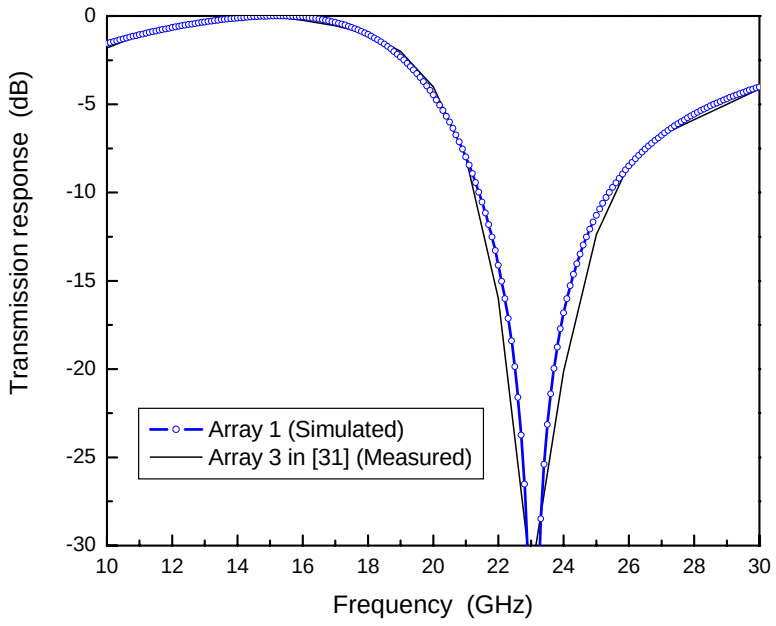

Figure 5-3 Simulated (array 1) and measured (array 3 in [32]) transmission responses at normal incidence for gridded-square array

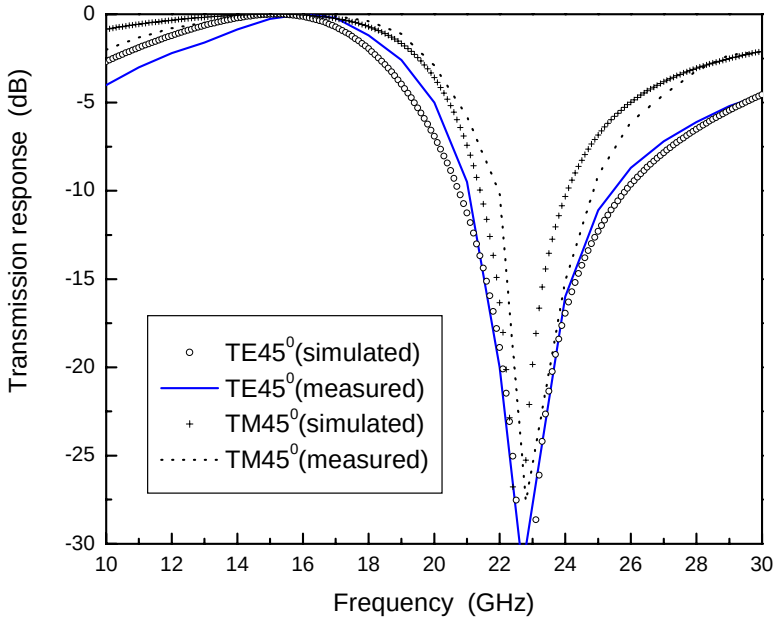

Figure 5-4 Simulated (array 1) and measured (array 3 in [32]) transmission responses at 45^0 TE incidence and 45^0 TM incidence for gridded-square array

5.3.3 Design of a Gridded-Square Array in Low-Frequency Region (1.8 / 2.45 GHz)

In view of the school of EEE effort in the satellite program, we are designing some FSS arrays for preliminary study for multi-band operation. The frequency band here is confined to 1GHz to 3GHz region. The exercise involves creating an FSS array with the transmission band centered at 1.8 GHz and the reflection band at 2.45 GHz.

In DES optimization, the search parameters are set to be $P_{cross} = 0.9$ and $P_{mut} = 0.7$. The population size is set to be $N_{pop} = 10 \times N_{par} = 40$. The frequency range is taken from 1GHz to 3.1 GHz with the step size of 0.01 GHz. The search range of the four optimization parameters is set as $50mm \le p \le 95mm$, $0.5mm \le w1 \le 30mm$,

$0.5mm \le w2 \le 30mm$, $0.5mm \le g \le 30mm$. The created array will be printed on very low-cost glass epoxy of 1.6mm thickness with dielectric constant of 4.5 for preliminary study. The empirically effective dielectric constant ε_{reff} of 1.8 is taken in ECM calculation for the substrate.

Five groups of results are tabulated in Table 5-3. It is observed that all five arrays at normal incidence have the transmission band centered close at 1.8 GHz and reflection band resonates close at 2.45 GHz, which satisfy the design specifications. These arrays have close band ratio f_r / f_T of about 1.38.

Table 5-3 Attained dimensions of optimization parameters for low-frequency gridded-square array at normal incidence

Array	Dimensions (mm)				f_T (GHz)	f_r (GHz)	f_r / f_T	-0.5dB (GHz) frequency	Band-width
	p	w_1	w_2	g					
1	80.0	6.8	0.7	22.5	1.77	2.45	1.38	1.41 - 1.99	32.77%
2	75.6	9.64	1.65	17.7	1.77	2.46	1.39	1.51 - 1.96	25.42%
3	82.9	10.7	1.8	21	1.77	2.43	1.37	1.48 – 1.96	27.12%
4	84.1	9.86	2.00	22.1	1.76	2.45	1.39	1.45 – 1.98	30.11%
5	64.6	9.55	1.89	11.7	1.77	2.44	1.38	1.58 – 1.92	19.2%

In consideration of larger bandwidth, array 1 was fabricated and measured. Measurements were conducted at the anechoic chamber at the school of EEE in NTU. Figure 5-5 shows the comparison of transmission responses between simulated and measured at normal incidence. A shallow null was measured at around 1.1 GHz. This is possible because the amplitude currents induced in the grid are very weak giving rise to a shallow resonance [90-91].

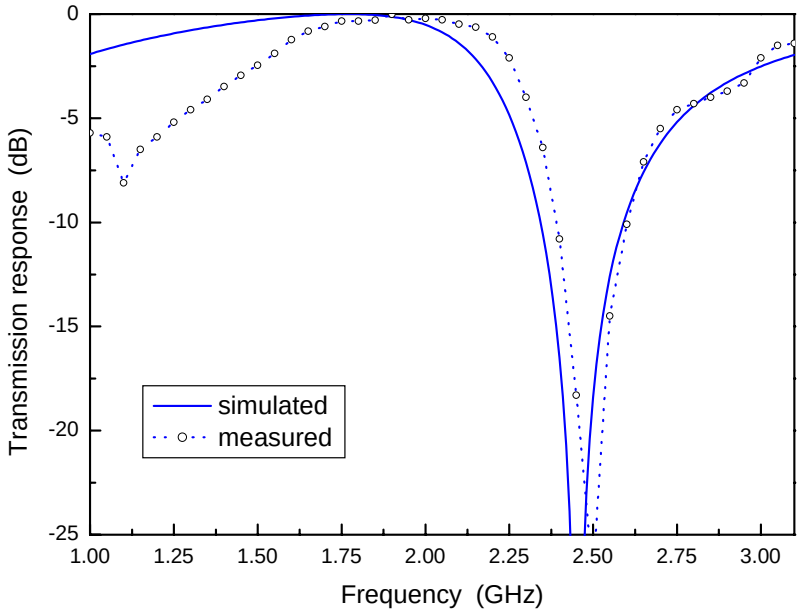

Figure 5-5 Simulated and measured transmission responses of array 1 at normal incidence for gridded-square array in low-frequency region

Their band centers are tabulated in Table 5-4. The measured and calculated band centers for this array are in close agreement. The measured transmission band is centered at 1.9 GHz (vs. 1.77 GHz for the model) and the reflection band at 2.5 GHz (vs. 2.45 GHz for the model). This gives a band-spacing ratio of 1.32 (vs. 1.38 for the model).

Table 5-4 Simulated and measured band centers of array 1 at normal incidence for gridded-square array in low-frequency region

Array	Transmission band Center frequency f_T (GHz)		Reflection band center frequency f_r (GHz)		Band ratio f_r / f_T	
	Simulated	Measured	Simulated	Measured	Simulated	Measured
1	1.77	1.9	2.45	2.5	1.38	1.32

The measured transmission responses at oblique incidences of normal, 15^0, 30^0, 45^0 TE and TM polarization are shown in Figure 5-6 and Figure 5-7 respectively. These band centers are relatively insensitive with respect to change of incident angles, as noted in the corresponding responses, moving by about 0.2 GHz from 0^0 to 45^0 incidence.

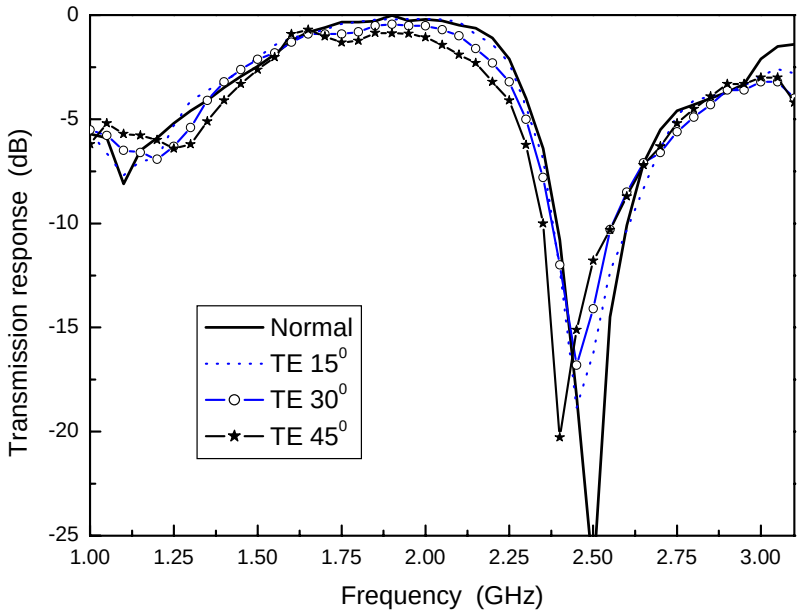

Figure 5-6 Measured transmission responses of array 1 for oblique incidences in TE polarized plane wave

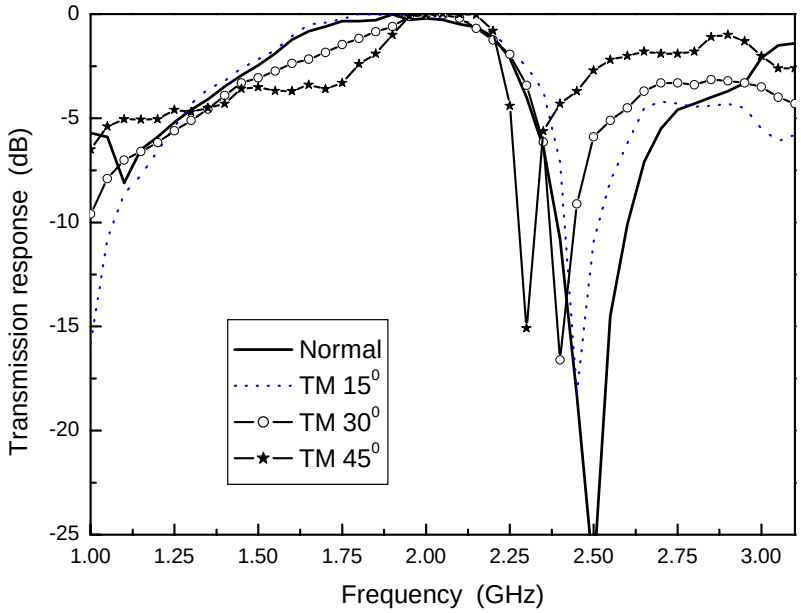

Figure 5-7 Measured transmission responses of array 1 for oblique incidences in TM polarized plane wave

5.3.4 Design of a Wide-Band Gridded-Square Array

The design criterion chosen here is to create an FSS array with a transmission band between 10.7-11.7 GHz and a reflection band between 18.2-20 GHz. The frequency band centers are spaced by a ratio of 1.7. This design specification was first reported in [51].

For larger band separations ($f_r / f_T > 1.6$) in gridded-square array, the conductor width of the square is more than 10% of the periodicity ($w_2 / p > 0.1$). In this design the maximum frequency of interest is about 22GHz and consequently the periodicity p must be less than 8.0mm for the angle of 45^0 incidence to avoid the onset of grating lobe. In our proposed method, the search range of the four optimization parameters $x = [p, w1, w2, g]$

is set as $4.0mm \le p \le 8.0mm$, $0.2mm \le w1 \le 2.0mm$, $0.2mm \le w2 \le 2.0mm$, $0.2mm \le g \le 2.0mm$. The population size is set as $N_{pop} = 10 \times N_{par} = 40$. The DES search parameters are set as $P_{cross} = 0.9$ and $P_{mut} = 0.7$. Here, $\varepsilon_{reff} = 1.12$ is used in ECM calculation.

Similar to the previous design, it can easily produce a group of parameters values which reaches the design objective after each simulation. Here, five results with maximum generation for converging and CPU running time for each created array are tabulated in Table 5-5.

Table 5-5 Attained dimensions of optimization parameters and calculated band centers for wide-band gridded-square array at normal incidence

Array	Dimensions (mm)				f_T (GHz)	f_r (GHz)	f_r / f_T	Genera-tions	CPU time (secs)
	p	w_1	w_2	g					
1	7.4	0.757	0.772	0.494	11.1	19.0	1.71	3	0.72
2	7.4	0.812	0.782	0.472	11.2	19.1	1.7	8	0.97
3	7.69	0.845	0.797	0.564	11.2	19.1	1.7	16	1.84
4	7.91	0.89	0.872	0.592	11.2	19.1	1.7	71	8.7
5	7.51	0.788	0.783	0.519	11.2	19.1	1.7	98	16.6

The calculated transmission response for array 1 at normal incidence is shown in Figure 5-8. It is observed that a pass-band bandwidth of 21.6% with an insertion loss of –0.5dB is obtained between 9.8GHz and 12.2GHz with the centre frequency at 11.1GHz. Figure 5-8 also shows the computed transmission response at TE $45^0$and TM 45^0 incidence for array 1. For stop-band, the common bandwidth for TE/TM incidence up to

45^0 (–10dB attenuation) is achieved as 15.3% with the centre frequency at 19.0GHz. The band spacing ratio f_r / f_t at normal incidence is equal to 1.71 which satisfies the design specifications. It is also observed that the transmission band is very stable to angles of incidence up to 45^0 in both the TE and TM incidences. At the reflection band, the band centers are shifted up by 1.2 GHz and 1.6 GHz in TE and TM incidence respectively. Overall, the results are acceptable for this design.

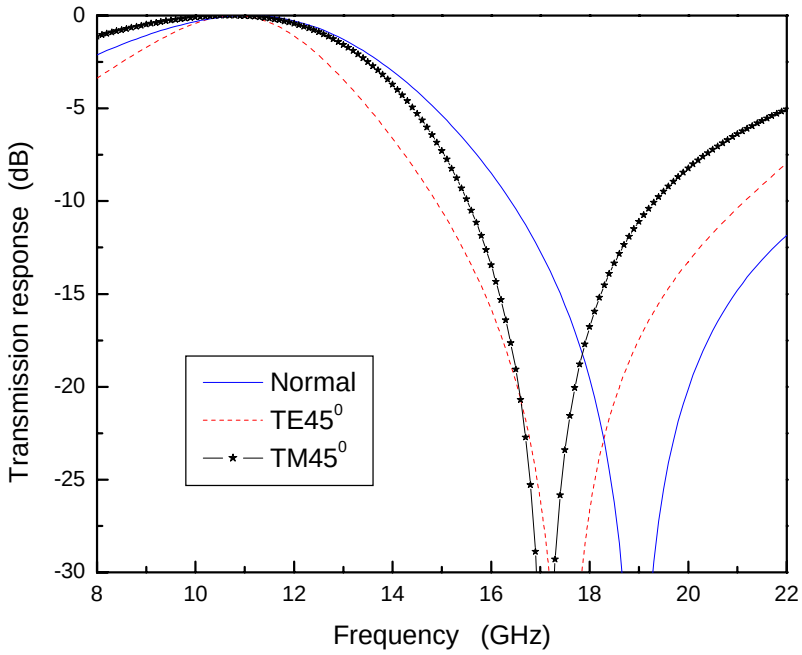

Figure 5-8 Simulated transmission characteristics of array 1 at normal incidence, $TE45^0$ and $TM45^0$ incidence for wide-band gridded-square array

Compared with previous researcher's work for the same design objective [51], our method (DES combined with ECM) avoids the trial and error operation. The required configuration can be easily obtained through DES optimization in a very short computational time.

5.4 Design of Multi-Band FSS with Gridded-Double-Square Elements

5.4.1 Formulations of Components Impedances

The geometry and the equivalent circuit model for gridded-double-square array are shown in Figure 5-9. A single inductance L_1 represents the grid which is responsible for the determination of the lower transmission band. A series resonant circuit L_2 and C_2 represents the outer square that determines the lower resonance. The upper reflection band is represented by L_3 and C_3.

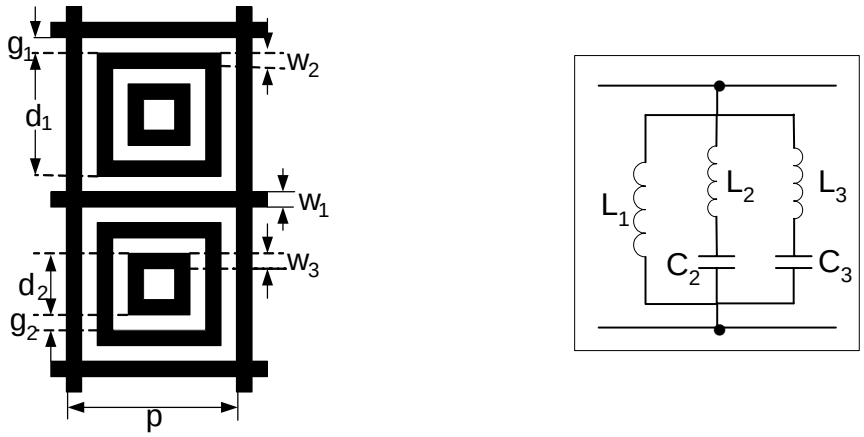

(a) (b)

Figure 5-9 Gridded-double-square array (a) geometry (b) equivalent circuit

For gridded-double-square array, the impedances of these components are given as [13]

$$X_1 = \omega L_1 = F(p, w_1, \lambda) \tag{5-9}$$

$$X_2 = \omega L_2 = 4.0 \times \frac{X_1 \times X_4}{X_1 + X_4} \times \frac{d_2}{p} \tag{5-10}$$

$$X_3 = \omega L_3 = 0.7 \times F(p, 2w_3, \lambda) \times d_2 / p \tag{5-11}$$

$$X_4 = F(p, 2w_2, \lambda)$$

$$B_0 = 4.0 \times \varepsilon_{reff} \times F(p, g_1, \lambda) \times d_1 / p$$

$$B_1 = 4.0 \times \varepsilon_{reff} \times F(p, g_2, \lambda) \times d_1 / p$$

$$B_2 = 0.25 \times \omega C_2 = 0.25 \times (0.8B_0 + 0.15B_1) \tag{5-12}$$

$$B_3 = \omega C_3 = \frac{B_0 \times B_1}{B_0 + B_1} \times \frac{d_2}{d_1} \tag{5-13}$$

$$Y = j\left[\left(\frac{B_3}{1 - X_3 \times B_3}\right) + \left(\frac{B_2}{1 - X_2 \times B_2}\right) - \frac{1}{X_1}\right] \tag{5-14}$$

Combined with the equations (2-83)-(2-86), the normalized admittance Y of an array can be calculated. Thus, the transmission response T can be determined from (2-90).

5.4.2 Design of a Triple-Band Gridded-Double-Square Array

This example demonstrates the design of a triple-band FSS to satisfy the specified design requirements to reflect frequency 17.0 GHz (f_r) signal while passing the frequency signal $f_{T1} = 12.7\,GHz$ and $f_{T2} = 24.3\,GHz$.

Gridded-double-square element is selected due to its typical response which has two transmission bands and one reflection-band between them. Referring to Figure 5-9, the configuration parameters for gridded-double-square array are $x = [p, w1, w2, w3, g1, g2]$. The frequency is set in the range of 8GHz to 34GHz with the step size of 0.1GHz. The interested maximum frequency is set as 28 GHz. We do not care the performance between

28 GHz and 34 GHz. Thus, the search range of the periodicity p must be less than 6.3mm for 45^0 incidence in order to avoid the onset of grating lobes. For this case, the search range of the six optimization parameters is set as $3.0mm \le p \le 6.3mm$, $0.1mm \le w1 \le 1.0mm$, $0.1mm \le w2 \le 1.0mm$, $0.1mm \le w3 \le 1.0mm$, $0.1mm \le g1 \le 1.0mm$, $0.1mm \le g2 \le 1.0mm$. The DES parameters used are $N_{par} = 6$, $N_{pop} = 10 \times N_{par} = 60$, $P_{cross} = 0.9$ and $P_{mut} = 0.7$. $\varepsilon_{reff} = 1.12$ is taken for ECM simulation.

There are infinite combinations of parameter values to realize these design requirements. Table 5-6 tabulates five groups of results. The maximum generation for DES converging and CPU running time for each generated array also are presented. It is observed that the configuration parameters still can be obtained at a very short time although the number of optimization parameters is increased (six for gridded-double-square array relative to four for gridded-square array). Compared with previous conducted synthesis design for the same objective in [12], DES can automatically find the optimum solution in the search range and prescribed specifications. Trial and error procedure is avoided.

Table 5-6 Attained dimensions of optimization parameters and convergence performance for gridded-double-square array at normal incidence

Array	Dimensions (mm)						Generations	CPU time (secs)
	p	w_1	w_2	w_3	g_1	g_2		
1	5.16	0.28	0.167	0.336	0.205	0.583	30	15.1
2	5.33	0.35	0.15	0.601	0.25	0.499	60	29.2
3	5.79	0.338	0.227	0.487	0.337	0.646	68	33.2
4	6.03	0.477	0.228	0.964	0.376	0.504	18	9.0
5	6.16	0.347	0.198	0.414	0.499	0.749	34	17.3

The simulated band centers at normal incidence, TE45^0 and TM45^0 incidence for five gridded-double-square arrays are summarized in Table 5-7. It is observed that all five arrays at normal incidence have the two transmission bands centered close on 12.7 and 24.3 GHz respectively and the reflection band resonates close at 17.0 GHz, which satisfy the design requirements. It is also observed that the band center frequency f_{T1} and f_r are relatively stable with respect to the incident angle variation. For array 1 and array 2, the second transmission band center frequency f_{T2} is relative stable in oblique angle of incidence while it is relative sensitive with the incident angle variation for array 3, 4 and 5. It is found that array 5 has the maximum 1.1 GHz shift from normal incidence to 45^0 incidence.

Table 5-7 Simulated band centers at normal incidence, TE45^0 and TM45^0 incidence for gridded-double-square array

Array	Transmission band center frequency f_{T1} (GHz)			Reflection band center frequency f_r (GHz)			Transmission band center frequency f_{T2} (GHz)		
	Normal	TE45^0	TM45^0	Normal	TE45^0	TM45^0	Normal	TE45^0	TM45^0
1	12.7	12.6	12.6	16.9	16.8	16.8	24.3	23.8	23.8
2	12.8	12.8	12.8	17.0	16.9	17.0	24.3	23.8	24.3
3	12.6	12.5	12.5	16.9	16.7	16.7	24.3	23.5	23.5
4	12.7	12.6	12.7	17.0	16.8	16.8	24.2	23.2	23.3
5	12.7	12.7	12.6	16.9	16.7	16.7	24.3	23.3	23.2

The synthesized dimensions for array 1 are very close to that of the array 3 in [12], which configuration dimensions are $[p, w_1, w_2, w_3, g_1, g_2] = [5.1, 0.22, 0.22, 0.22, 0.19, 0.58]$

(units in mm). Their comparison of transmission responses is shown in Figure 5-10. Good agreements are observed before 26 GHz. The band center ratios $f_r / f_{T1} = 1.33$ and $f_{T2} / f_r = 1.44$ (simulated at normal incidence) are obtained. The experiment results for the array 3 in [12] were reported. Figure 5-11 and Figure 5-12 show the comparison between the simulated (array 1) and the measured (array 3 in [12]) transmission responses at normal incidence, TE 45^0 incidence and TM 45^0 incidence. It is observed that f_{T1}, f_r and f_{T2} are very stable with the variation of incident angles for both simulated and measured results. Meanwhile, good agreements between simulated and measured results are also observed for incident angles up to 45^0 in both TE and TM incidence. The second resonant frequency (>28GHz) is very sensitive with respect to the change of incident angle and is consequently unsuitable for multi-band applications.

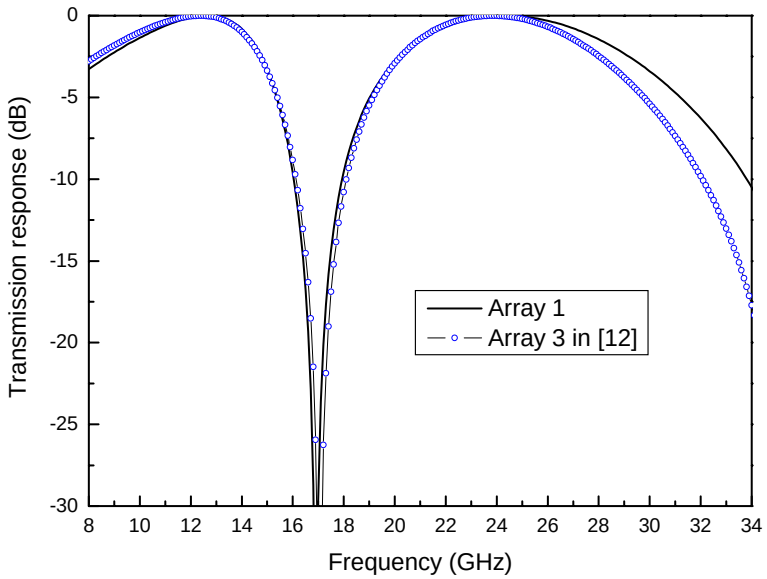

Figure 5-10 Simulated transmission responses of array 1 and array 3 in [12] at normal incidence for gridded-double-square array

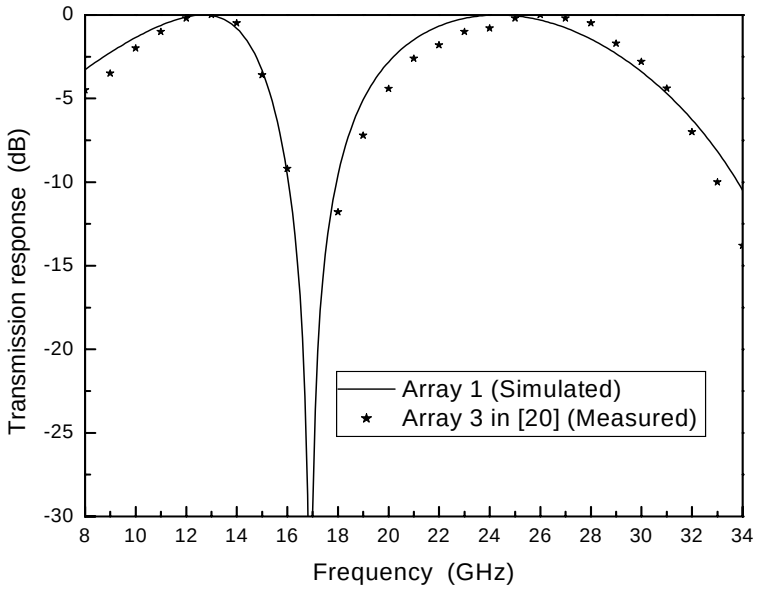

Figure 5-11 Simulated (array 1) and measured (array 3 in [12]) transmission responses at normal incidence for gridded-double-square array

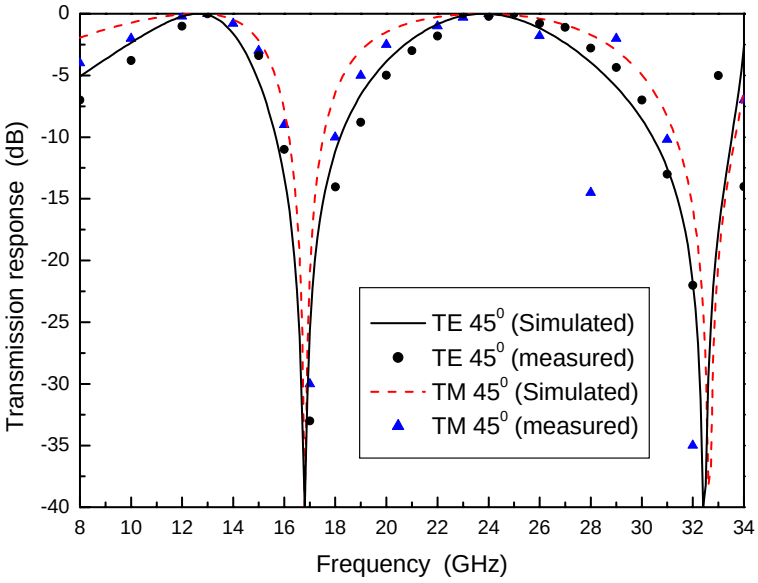

Figure 5-12 Simulated (array 1) and measured (array 3 in [12]) transmission responses at TE 45^0 and TM 45^0 incidence for gridded-double-square array

5.5 Design of Four-Band FSS with Wide-Band Double-Square Elements

5.5.1 Formulations of Components Impedances for Wide-Band Double-Square Array

The geometry and the equivalent circuit model for wide-band double-square array are shown in Figure 5-13. The single LC series resonant circuit models the frequency response up to and including the first resonance only [13].

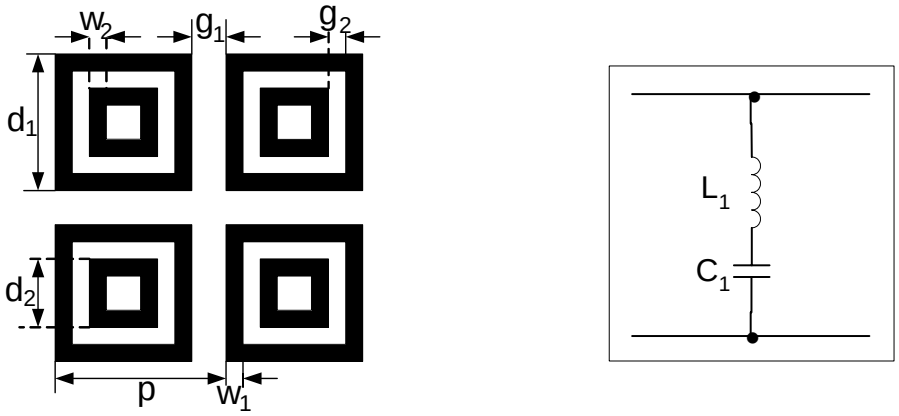

(a) (b)

Figure 5-13 Wide-band double-square array (a) geometry (b) equivalent circuit

For wide-band ($g_1/p > 0.25$) double-square array at normal incidence, the impedances of these components are given as [12]

$$X_0 = F(p, w_1, \lambda) \times d_1/p$$

$$B_0 = 4 \times \varepsilon_{reff} \times F(p, g_1, \lambda)$$

$$X_1 = \begin{cases} X_0, & 0.25 < g_1/p < 0.33 \\ X_0 \times 1.25, & 0.33 < g_1/p < 0.4 \\ X_0 \times 1.74, & g_1/p > 0.4 \end{cases} \quad (5\text{-}15)$$

$$B_1 = \begin{cases} B_0 \times 0.72, & 0.25 < g_1/p < 0.33 \\ B_0 \times 0.62, & 0.33 < g_1/p < 0.4 \\ X_0 \times 0.5, & g_1/p > 0.4 \end{cases} \quad (5\text{-}16)$$

$$Y = \frac{jB_1}{1 - X_1 \times B_1} \quad (5\text{-}17)$$

5.5.2 Design a Wide-Band Double-Square Array

The design of a Low-pass four-band FSS for Cassini configuration is described here. The design specifications are to have reflection at the Ka-band (33 GHz) wave while transmit the lower frequency waves at S-, X-, and Ku-band. In additional, it must be insensitive to the incident angle variation and polarizations.

The double-square patch elements are selected as optimization geometry because of its multi-band characteristics. For double-square array, wide range of band center spacing can be achieved by having larger g_1/p ratio. In this design, the maximum frequency of interest is about 36 GHz and consequently the periodicity p must be less than 4.9 mm for an oblique angle of 45^0 incidence in order to avoid the onset of the grating lobes. The search range of the five optimization parameters is set as $3.0mm \le P \le 4.9mm, 0.2mm \le w_1 \le 1.0mm, 0.2mm \le w_2 \le 1.0mm, 1.0mm \le g_1 \le 3.0mm,$ $0.2mm \le g_2 \le 2.0mm$. The frequency is set in the range of 1 GHz to 36 GHz and the step

size is 0.1 GHz. The population size is set to be $N_{pop} = 50$. The search parameters are set to be $P_{cross} = 0.9$ and $P_{mut} = 0.7$. Here, $\varepsilon_{reff} = 1.12$ is taken in ECM calculation for the 0.027 mm polyester substrate.

Table 5-8 tabulates five combinations of parameter values which are produced by DES optimization to realize this design objective. The number of generations for converging and CPU time taken for each created combination are also presented. Four-band low-pass FSS arrays are obtained, which can be used to transmit the S-, X- and Ku-band signals while reflecting Ka-band signal. Figure 5-14 shows the computed transmission responses of array 1 in Table 5-8 at normal incidence, TE 45^0 and TM 45^0 incidence. It can be observed that the resonant frequency f_r occurs at 32.9GHz and the maximum insertion loss of –0.5dB is obtained at 20.8 GHz at normal incidence. The resonant frequency moves down marginally to 31.2 and 31.5 GHz for TE and TM incidence respectively. The resonant frequency is relatively stable with respect to the incident angle variation.

Table 5-8 Attained dimensions of optimization parameters at normal incidence for wide-band double-square array

Array	Dimensions (mm)					-0.5dB (GHz)	f_r	Genera-tions	CPU time (Secs)
	p	w_1	w_2	g_1	g_2				
1	4.79	0.588	0.341	1.45	0.248	20.8	32.9	12	0.46
2	4.46	0.23	0.464	1.59	0.208	18.5	32.9	15	0.55
3	4.83	0.287	0.391	1.84	0.34	18.7	32.8	14	0.51
4	4.85	0.335	0.551	1.81	0.262	18.4	32.9	13	0.47
5	4.82	0.332	0.245	1.78	0.658	18.3	32.8	22	0.62

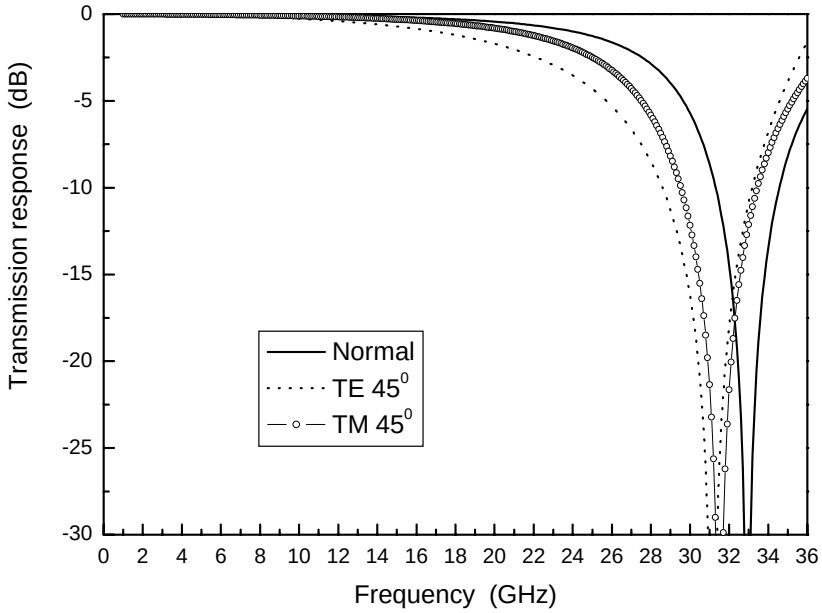

Figure 5-14 Computed transmission responses of array 1 at normal incidence, TE45^0 and TM45^0 incidence for wide-band double-square array

The synthesis design (trial and error procedure) for the same objective can be found in [89]. Compared with the design in [89], DES can automatically seek the optimum parameters values to satisfy the specific design objective in defined search range in very short computational time.

5.6 Design of Triple-Band FSS with Double-Square Elements

5.6.1 Formulations of Components Impedances for Narrow-Band Double-Square Array

The geometry and the equivalent circuit model for narrow-band double-square array are shown in Figure 5-15. The model consists of two LC series resonant circuits with L_1, C_1 representing the first resonant frequency and L_2, C_2 for the upper reflection band.

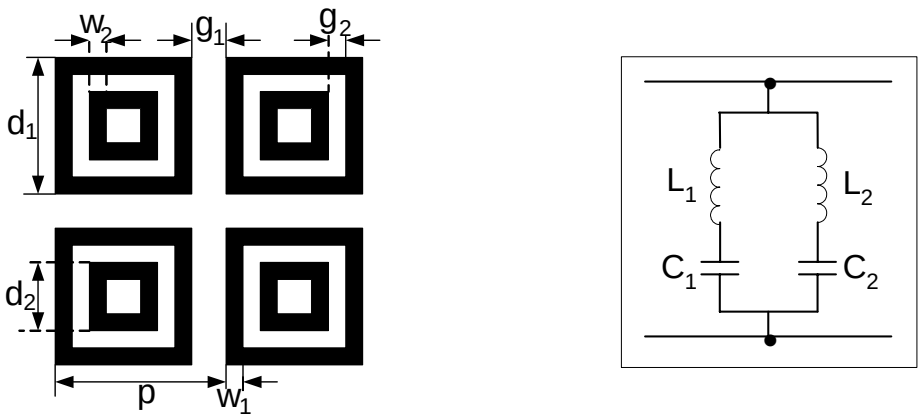

(a) (b)

Figure 5-15 Narrow-band double-square array (a) geometry (b) equivalent circuit

For narrow-band $(g_1/p < 0.25)$ double-square array, the impedances of these components are given as [50]

$$X_{1p} = F(p, w_1, \lambda)$$

$$X_{2p} = F(p, w_2, \lambda)$$

$$X_1 = \omega L_1 = 2.0 \times \frac{X_{1p} X_{2p}}{X_{1p} + X_{2p}} \times (d_1/p) \tag{5-18}$$

$$X_2 = \omega L_2 = F(p, 2w_2, \lambda) \times (d_2/p) \tag{5-19}$$

$$B_{1p} = 4.0 \times \varepsilon_{reff} \times F(p, g_1, \lambda)$$

$$B_{2p} = 4.0 \times \varepsilon_{reff} \times F(p, g_2, \lambda)$$

$$B_1 = \omega C_1 = 0.75 \times B_{1p} \times (d_1 / p) \tag{5-20}$$

$$B_2 = \omega C_2 = \frac{B_{1P} B_{2P}}{B_{1P} + B_{2P}} \times (d_2 / p) \tag{5-21}$$

$$Y = j\left[\left(\frac{B_1}{1 - X_1 B_1}\right) + \left(\frac{B_2}{1 - X_2 B_2}\right)\right] \tag{5-22}$$

5.6.2 Synthesis Configuration

Double-square FSS array is essentially a double-resonant structure providing low and high frequency reflection bands coupled with a transmission band between them. The proposed FSS design is to yield pass-band at 12.5-13.5 GHz with band center at 13.0 GHz (f_T). The center resonant frequencies are at 9.5 GHz (f_{r1}) and 16 GHz (f_{r2}) for the stop-band at 8-11 GHz and 15-18 GHz respectively. The design process involves synthesizing the geometry parameters of double-square array.

Referring to Figure 5-15, the configuration parameters of an FSS array with double-square elements are $x = [p, w1, w2, g1, g2]$. The DES parameters used are $N_{par} = 5$, $N_{pop} = 10 \times N_{par} = 50$. The search parameters of DES are set to be $P_{cross} = 0.9$ and $P_{mut} = 0.7$. The frequency chosen for the study is between 2 GHz and 18 GHz with the step size of 0.1 GHz. In this design, the maximum frequency of interest is about 18GHz and consequently p must be less than 9.76 mm for angle incidence of 45^0 to avoid the occurrence of grating lobes. The search range of the optimization parameters is set as:

$3.0mm \le p \le 9.76mm$, $0.2mm \le w1 \le 2.0mm$, $0.2mm \le w2 \le 2.0mm$, $0.2mm \le g1 \le 2.0mm$, $0.2mm \le g2 \le 2.0mm$.

Table 5-9 tabulates five groups of results by DES optimization. The maximum generation for DES convergence and CPU computational time are also presented. It is observed that all five arrays at normal incidence have the two reflection bands resonated close at 9.5 and 16 GHz respectively and the transmission band centered close at 13.0 GHz, which satisfy the design objective. To validate our design, array 1 was fabricated and measured. The designed FSS array was printed on a 0.127mm Mylar substrate, which has a dielectric constant of 3.5 and loss tangent of 0.01 (overall dimension of 265mm by 265mm). ε_{reff} =1.12 as suggested by Lee *et al* [13] is used here.

5.6.3 Measured Results and Discussions

Measurements were conducted at the anechoic chamber at the school of EEE in NTU. The measured transmission response at normal incidence is compared with the theoretical calculation as shown in Figure 5-16. Good agreements between the measured and optimized results are observed. The resonant frequencies of the simulated curve are 9.6 and 16.2 GHz that is very close to the initial desired values of 9.5 and 16.0 GHz respectively. The array has a band spacing $f_T / f_{r1} = 1.33$ and f_{r2} / f_T =1.27. In the simulated curve, –10dB attenuation points are achieved at 8.1, 10.8 GHz and –0.5dB points (pass-band) are achieved at 12.5-13.2 GHz.

Table 5-9 Attained values of optimization parameters and band centers for narrow-band double-square array at normal incidence

Array	Dimensions (mm)				f_{r1}	f_T	f_{r2}	f_T/f_{r1}	f_{r2}/f_T	Genera-tions	CPU time (Secs)
	p	w_1	w_2	g_1	g_2						
1	8.08	0.93	0.238	0.548	0.369	9.6	12.8	16.2	1.33	1.27	8	1.95
2	8.25	0.727	0.236	0.699	0.45	9.6	12.7	15.9	1.32	12.5	169	87.5
3	8.45	1.18	0.202	0.578	0.362	9.5	12.7	15.9	1.34	1.25	89	34.1
4	8.76	1.21	0.406	0.649	0.204	9.7	12.7	16.0	1.31	1.26	3	0.8
5	8.78	0.943	0.237	0.832	0.463	9.7	12.8	16.0	1.32	1.25	50	23.9

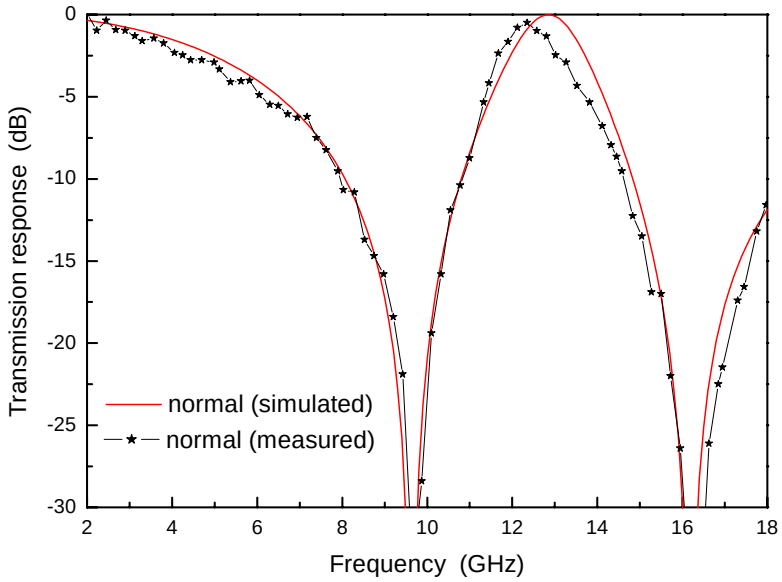

Figure 5-16 Simulated and measured transmission responses of array 1 at normal incidence for double-square array

The frequency responses of the double-square array for oblique incidence were also measured. Comparison of transmission responses between the measured and simulated at $TE15^0$, $TE30^0$, $TE45^0$ are shown in Figure 5-17 while their TM counterparts are shown in Figure 5-18. Table 5-10 tabulates the frequency band centers that are compared with the experimental results at oblique incident angles. It can also be found that the shifts of the frequency response with the change of incident angles are stable for both TE and TM incidences. Furthermore, this array is capable of giving relatively close band spacing with band center frequency ratios at about 1.3. The measured frequency responses for oblique incidence of a TE or TM polarized plane wave are shown in Figure 5-19. It can be observed that the resonant frequencies are very stable with respect to the incident angle

variation for this design. The transmission between the two resonances is also very stable. The insertion loss in pass-band is less than 0.5 dB.

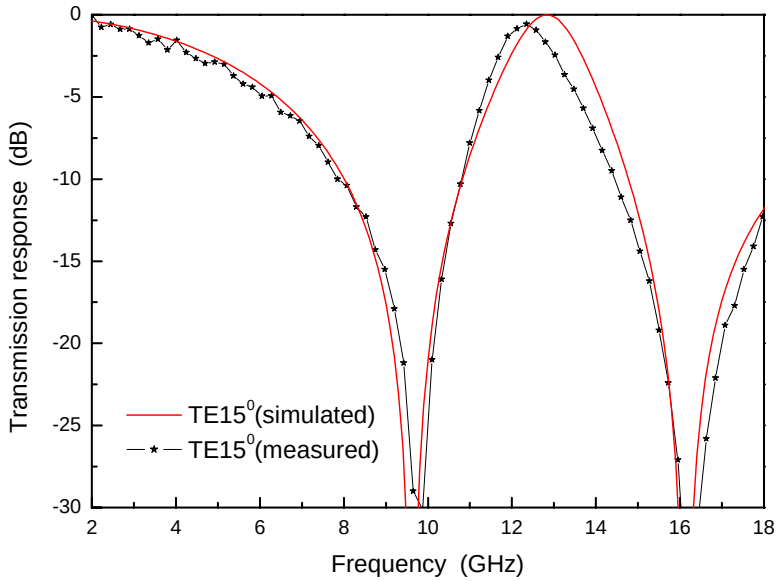

(a)

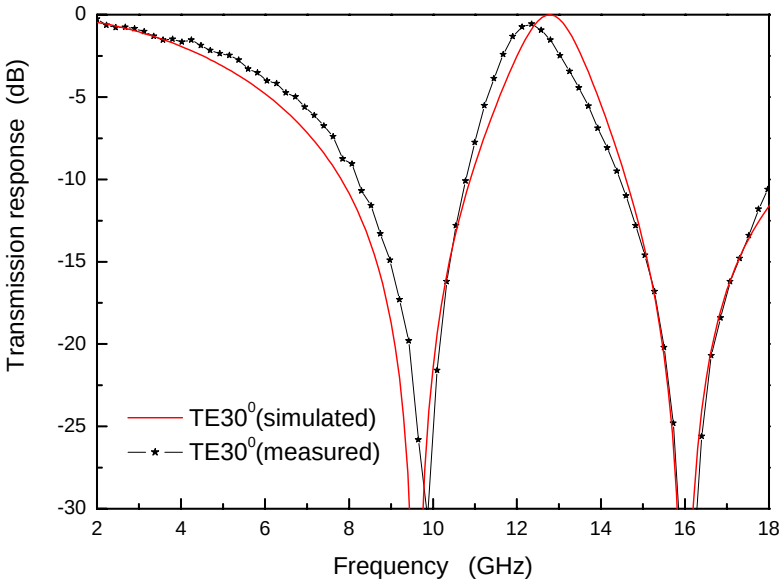

(b)

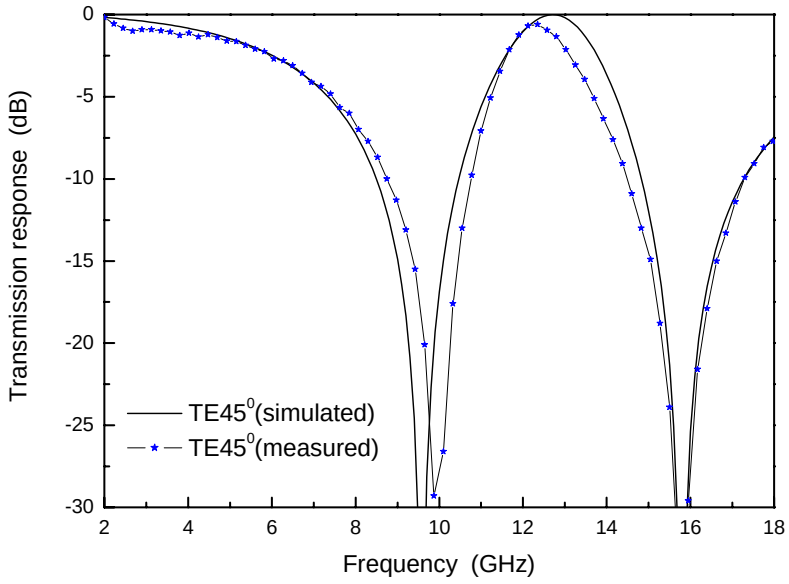

(c)

Figure 5-17 Simulated and measured transmission responses of array 1 at oblique incidence of TE polarized for double-square array (a) TE15^0 (b) TE30^0 (c) TE45^0

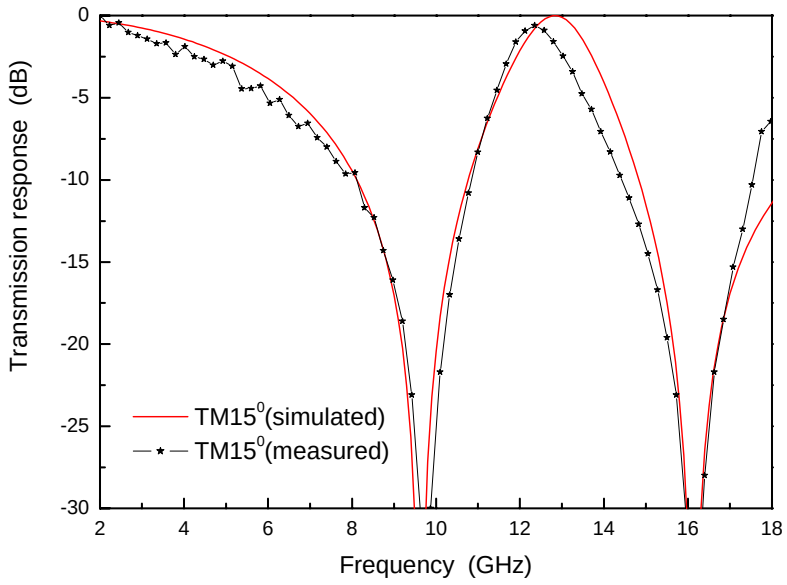

(a)

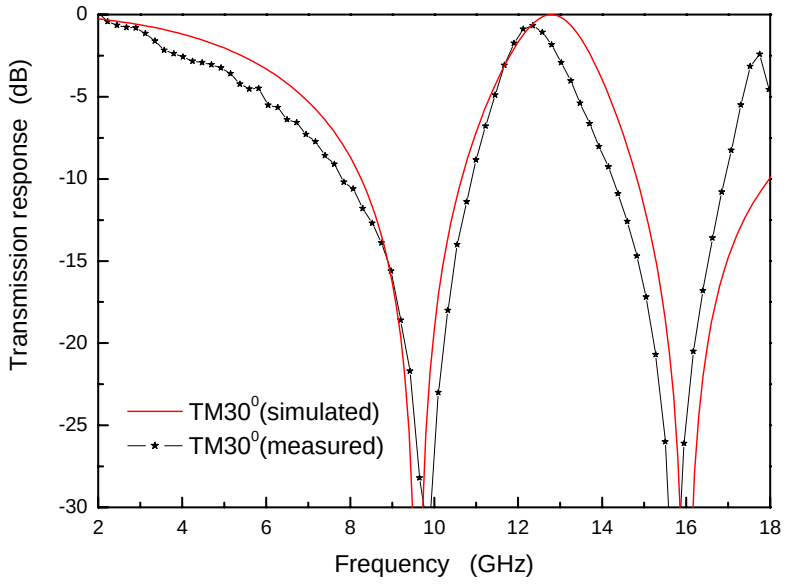

(b)

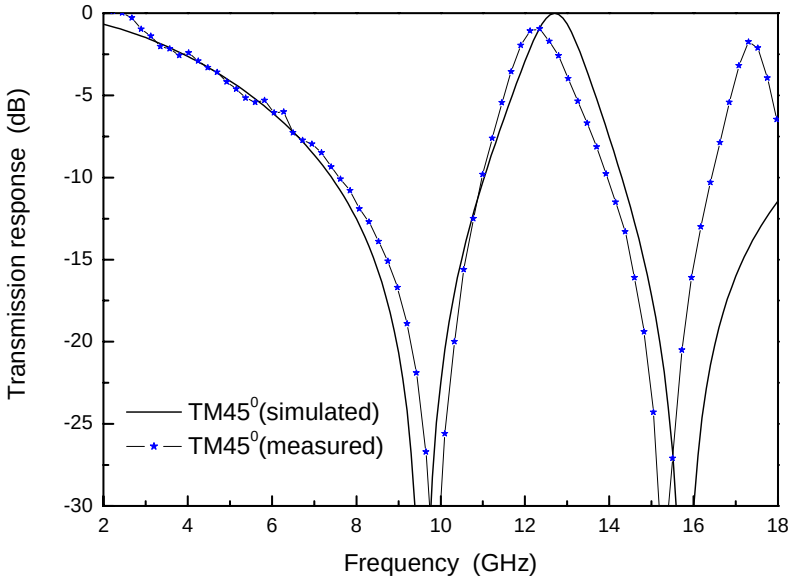

(c)

Figure 5-18 Simulated and measured transmission responses of array 1 at oblique incidence of TM polarized for double-square array (a) TM15^0 (b) TM30^0 (c) TM45^0

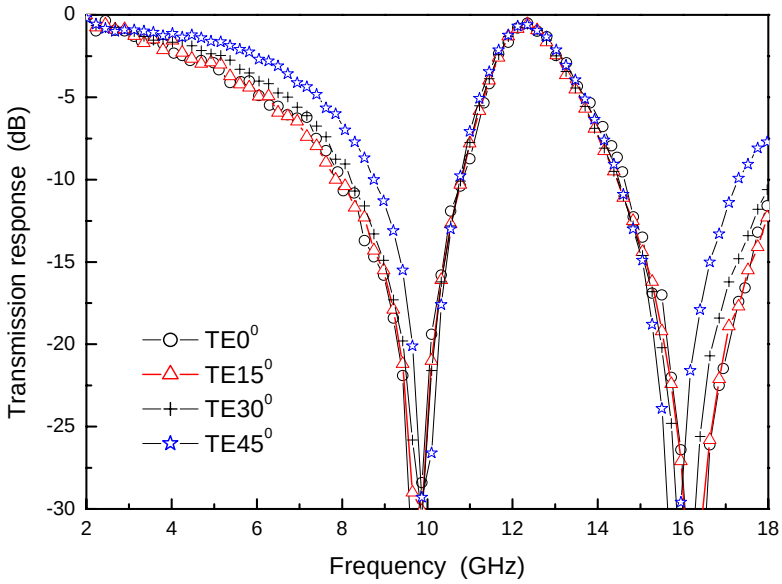

(a)

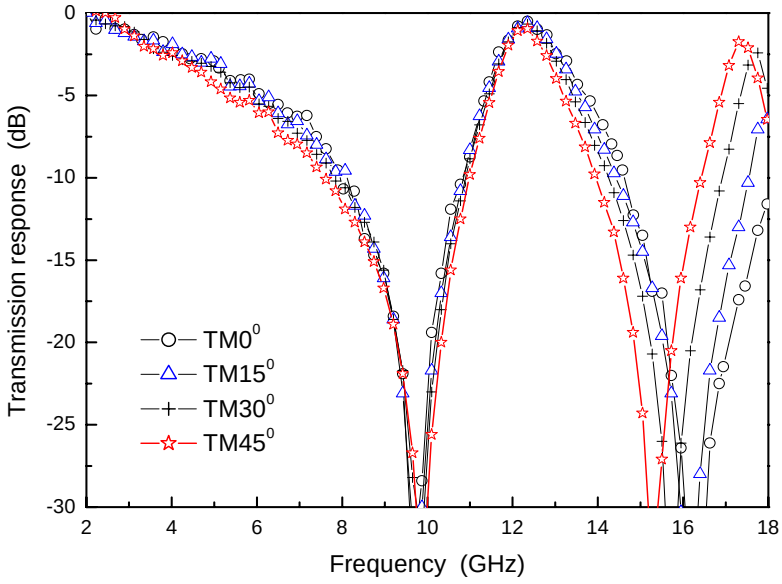

(b)

Figure 5-19 Measured frequency responses of designed double-square array for oblique incidence (a) TE incidence (b) TM incidence

Table 5-10 Measured and simulated band centers for the designed double-square array

	f_{r1} (GHz)			f_T (GHz)			f_{r2} (GHz)			Band ratio (measured)	
	C	M	Δf	C	M	Δf	C	M	Δf	f_T / f_{r1}	f_{r2} / f_T
Normal	9.6	9.7		12.8	12.4		16.2	16.3		1.28	1.31
TE15^0	9.6	9.7	0%	12.8	12.3	0.8%	16.1	16.2	0.6%	1.27	1.32
TE30^0	9.6	9.8	1%	12.8	12.3	0.8%	16.0	16.0	1.8%	1.26	1.30
TE45^0	9.6	9.9	2%	12.7	12.3	0.8%	15.8	15.8	3%	1.24	1.28
TM15^0	9.6	9.7	0%	12.8	12.4	0%	16.1	16.1	1.2%	1.28	1.30
TM30^0	9.6	9.8	1%	12.8	12.3	0.8%	16.0	15.8	3%	1.26	1.28
TM45^0	9.6	9.9	2%	12.7	12.3	0.8%	15.8	15.3	6%	1.24	1.24

Note: C = the results computed, M = the results measured, Δf = measured frequency shift with respect to normal incidence.

Good agreements between the simulated and measured results demonstrated that the proposed DES coupled with ECM is a useful technique in the design of FSS.

5.7 Conclusions

In this chapter, a novel method using DES combined with ECM is proposed to design FSS structures for multi-band applications. The efficient optimization algorithm, DES is employed to tune the FSS unit cell dimensions. The fast computation method, ECM is used to analyze the frequency response from FSS screen.

The design process is similar to that presented in Chapter 4.2. However, the frequency response of FSS screen is computed by ECM. The definition of objective function is also different from that of Chap. 4. It is relevant with the performances of pass-band and stop-band. In our proposed method, one only needs to set the search range of optimization parameters and give the convergence criterion (defined by the objective function). Then, the program can automatically seek and find the optimum configuration parameter values in very short time.

Six multi-band design examples are presented to demonstrate the efficiency of the proposed method. The first three designs are to design narrow-band and wide-band gridded-square arrays to diplex two separated frequency bands. One of designed FSS arrays operating in the low frequency region (1 to 3 GHz) was chosen to be fabricated for the preliminary study. The fourth one is to design a triple-band FSS with gridded-double-square array. The fifth one is to design a low-pass four-band FSS with wide-band double-square array to transmit the S-, X-, and Ku-band signals while rejecting Ka-band signal. The last one is to design a double-resonant double-square structure providing low (9.5 GHz) and high (16 GHz) frequency reflection bands coupled with a transmission band (13.0 GHz) between them. This designed FSS array was manufactured and measured. Good agreements between the simulated and measured results are observed.

All the optimized combinations to satisfy the specific requirements are created in a relatively short simulation time using above proposed methods (DES cum ECM). In addition, the tedious trial and error procedure is avoided. Overall results demonstrate that the proposed DES coupled with ECM is a useful technique in the design of FSS.

Chapter 6 Conclusions and Recommendations for Future Research

6.1 Conclusions

This thesis focuses on the design and optimization of FSS. Optimization algorithm is proposed to apply in the design of FSS to avoid the trial and error procedure. Previous research works on the optimization of FSS have produced complicated and irregular unit cell randomly by GA based on the binary-coded. It is impractical to fabricate. In this thesis, a more efficient optimization algorithm, DES is developed and combined with analytical method to optimize the standard, non-irregular FSS unit cell.

The analytical models derived for FSS are essential to the design of FSS. Two analytical methods, spectral-domain MoM and ECM for FSS are reviewed. Spectral-domain MoM can accurately analyze multi-layered FSS with arbitrary shape elements. Compared with the spectral-domain MoM technique presented by Mittra and Chan, the expressions of the reflection and transmission coefficients based on electric field instead

of vector electric potentials are derived here in our technique. Some revisions for the derivation of multi-layered Green's function are implemented. Unlike expressions from Mittra and Chan's, our developed spectral-domain MoM method is applicable to normal incidence. The other analytical method, ECM can provide frequency response of a FSS with relatively shorter computational time. For double-square, gridded-square and gridded-double-square elements, ECM can give the relatively accurate analysis, which has been reported through comparison with measured results.

Three kinds of optimization algorithms, SGA, RGA and DES are investigated. The convergence performance of SGA, RGA and DES is compared through minimizing the objective function under the same search range and convergence criterion. DES is found to be the most efficient and robust optimization tool among them because of its fastest convergence. The theoretical explanation about the efficiency of DES is also presented. Parameters (population size, crossover probability and mutation intensity) controls in DES are suggested for solving optimization problems. As a result, DES is chosen as optimization tool to optimize the FSS unit cell and dielectric properties in the design of FSS with prescribed performance in this thesis.

A novel design method is proposed to design FSS structures with prescribed performance, which is DES coupled with spectral-domain MoM. The frequency response from the FSS screen is analyzed by the spectral-domain MoM technique while the dimensions of the FSS unit cell and dielectric properties are optimized by DES. The objective function is defined as the relative error between actual and prescribed frequency response. The novel method is demonstrated through constructing an FSS dipole array without and with substrate. The good agreement between the synthesized results and the

true profiles proves the efficiency of the proposed FSS design method. Furthermore, RGA is also applied in the same configuration design. It further proves that DES is a more simple, efficient and robust method for the design of FSS. This proposed method also is applied in the design of band-pass and band-stop filter using hexagon array and gangbuster array. There is little literature about the design of these two arrays using optimization algorithm. A practical application example in mobile communication is realized using hexagon array. Flat pass-band and stop-band are obtained using these two arrays and broad-band performance is realized. Arbitrary bandwidth can be realized through designing the hexagon array or gangbuster array using our proposed optimization approach.

Another novel design method using DES combined with ECM is proposed to design FSS for multi-band application. The double-square, gridded-square and gridded-double-square elements are chosen as optimization objective because their resonant frequencies are fairly stable with respect to changes in the incident angle and polarization. Design examples are given to demonstrate the efficiency of the proposed method. Two of the designs, a gridded-square array and a double-square array, were fabricated and experimentally tested. Good agreements between the simulated and measured results and the fast computation speed demonstrate that the proposed DES coupled with ECM is a useful technique in the design of FSS. Compared with designs by other researchers, the proposed method can automatically seek and obtain the optimum configuration objective in very short time under simple and effective method. The trial and error process is avoided.

6.2 Recommendations for Future Research

Finally, we suggest a few topics, which can be explored as future work based on the thesis.

- To explore the possibility of improving the existing DES technique or novel optimization approach on the design of FSS in future. The objective is to obtain desired FSS frequency response with the faster convergence and shorter computational time.

- Although the underlying theoretical descriptions of FSS have been studied, computational time is still a major concern. In future, we suggest improving the spectral-domain MoM technique to decrease the computational time or develop other analysis methods to satisfy requirements of variable FSS structures.

- Multi-layered FSS structures with ring elements present the stable band-pass and band-stop performance. It is a big challenge to analyze ring structure accurately with the computer program coding. Further work can focus on the derivation of equivalent circuit for multi-layered FSS ring array or the selection of the basis function for ring elements in spectral-domain MoM technique.

- For every application, we have tried to compare results simulated from the proposed method with published experimental results or our measured results. However, some experiments cannot be carried out due to the limitation of fund. It would be better to do experiments for the actual devices under investigation to validate the proposed design.

Author's Publications

Journal Papers

1. X. F. Luo, P. T. Teo, A. Qing and C. K. Lee, "Design of Double-Square-Loop Frequency Selective Surfaces Using Differential Evolution Strategy Coupled with Equivalent Circuit Model", *Microw. Opt. Tech. Lett.*, vol. 44, no. 2, pp. 159-162, 20 Jan. 2005.

2. X. F. Luo, A. Qing and C. K. Lee, "On the Application of Differential Evolution Strategy to the Design of Frequency Selective Surfaces", *International Journal of RF and Microwave Computer-Aided Engineering*, USA, vol. 15, no. 2, pp. 173-180, March 2005.

3. P. T. Teo, X-F Luo, and C. K. Lee. "Transmission of convoluted periodic loop element with selective reflection" *Applied Physics Letters*, vol. 85, no.9, pp. 1454-1456, 30 Aug. 2004.

4. P. T. Teo, X. F. Luo and C. K. Lee, "Design of dual layer spatial filter via equivalent-circuit and smith chart approach for antenna's higher harmonics rejection", *WSEAS Transaction of Communications*, vol. 5, no. 5, pp. 647-655, May 2006.

5. P. T. Teo, X. F. Luo and C. K. Lee, "Frequency selective surfaces for GPS and DCS1800 mobile communication, part 1: quad layer and single layer FSS design", *IEE Proc. Microw. Antennas Propag* (Accepted).

6. C. K. Lee, P. T. Teo and X. F. Luo, "Frequency selective surfaces for GPS and DCS1800 mobile communication, part 2: integration with antenna for scattering reduction", *IEE Proc. Microw. Antennas Propag* (Accepted).

Conference:

1. X. F. Luo, A. Qing and C. K. Lee, "The design of Frequency Selective Surfaces (FSS) Using Real-coded Genetic Algorithm (RGA)," *IEEE Fourth International Conference on Information, Communications & Signal Processing and Fourth Pacific-Rim Conference on Multimedia (ICICS-PCM 2003)*, vol. 1, pp.391-395, Singapore, 15-18 Dec. 2003.

2. X. F. Luo, C. K. Lee and A. Qing, "Design of Frequency Selective Surfaces (FSS) Using Differential Evolution Strategy (DES)," *27th ESA Antenna Technology Workshop on Innovative Periodic Antennas: Electromagnetic Bandgap, Left handed materials, Fractal and Frequency Selective Surfaces*, pp. 201-207, Santiago de Compostela, Spain, 9-11th Mar. 2004.

3. X. F. Luo, P. T. Teo, A. Qing and C. K. Lee, "Design of double-square-loop frequency selective surfaces using differential evolution strategy coupled with equivalent circuit model," *The 4th international conference on microwave and millimeter wave technology*, pp. 94-97, Beijing, China, 18-21 Aug. 2004.

4. C. K. Lee, P. T. Teo and X. F. Luo, "Convoluted loop element for bandpass periodic array," *The 4th international conference on microwave and millimeter wave technology*, pp. 781-784, Beijing, China, 18-21 Aug. 2004.

5. X. F. Luo, P. T. Teo and C. K. Lee, "Bandpass frequency selective array design and its effect on DCS1800-GPS antenna scattering", *Loughborough Antennas and Propagation Conference 2005*, Loughborough University, UK, 4-6 Apr. 2005.

6. P. T. Teo, X. F. Luo and C. K. Lee, “Analysis and design of FSS for GPS and DCS1800 via equivalent circuit, transmission line and smith chart approach”, *Loughborough Antennas and Propagation Conference 2005,* Loughborough University, UK, 4-6 Apr. 2005.

Bibliography

[1] G. Marconi and C. S. Franklin, “Reflector for use in wireless telegraphy and telephony”, *US patent 1,301,473*, April 1919.

[2] R. Mittra, C. H. Chan and T. Cwik, “Techniques for analyzing frequency selective surfaces-A review,” *Proc. IEEE*, vol. 76, no. 12, pp. 1593-1615, Dec. 1988.

[3] T. K. Wu, *Frequency Selective Surface and Grid Array*, John Wiley & Sons Inc., 1995.

[4] J. C. Vardaxoglou, *Frequency Selective Surfaces: Analysis and Design*, Research Studies Press, John Wiley & Sons Inc., March 1997.

[5] B. A. Munk, *Frequency Selective Surfaces: Theory and Design*, John Wiley & Sons Inc., New York, 2000.

[6] B. A. Munk, *Finite Antenna Arrays and FSS*, John Wiley & Sons Inc., 2003.

[7] A. Stanley, B. Philips and E. A. Parker, “Ray tracing fields in a dichroic radome enclosing a Hertzian dipole,” *Proc. URSI International Conference on Mathematical Methods in Electromagnetic Theory*, Lviv, Ukraine, pp. 277-280, Sep. 1996.

[8] J. Hirai and I. Yokota, "Electromagnetic shielding glass of frequency selective surfaces," *Proceedings of the International Symposium on electromagnetic compatibility*, pp. 314-316, May 1999.

[9] J. J. Fratamico, M. J. Gans and G. J. Owens, “A wide scan quasi-optical frequency

diplexer," *IEEE Trans. Microw. Theory & Tech.*, vol. 82, no. 1, pp. 20-27, Jan. 1982.

[10] F. Terracher and G. Berginc, "Thin electromagnetic absorber using frequency selective surfaces," *IEEE Int. Symp. Antennas & Propagat.*, vol. 2, pp. 846-849, 2000.

[11] C. K. Lee, R. J. Langley and E. A. Parker, "Compound reflector antennas", *IEE Proc. Microw. Antennas Propag.*, vol. 139, no. 2, pp. 135-138, Apr. 1992.

[12] R. J. Langley and C. K. Lee, "Design of single-layer frequency selective surfaces for multiband reflector antennas," *Electromagnetics*, vol. 5, no. 4, pp. 331-347, 1985.

[13] C. K. Lee, "Modeling and design of frequency selective surfaces for reflector antennas," *Ph.D. dissertation*, Kent University, 1987.

[14] G. J. Cox, K. Zorzos, R. D. Seager and J. C. Vardaxoglou, " Study of frequency selective surface (FSS) resonator elements on a circular dielectric rod antenna for mobile communications," *IEE 11th International Conference on Antennas and Propagation (ICAP 2001)*, vol. 2, no. 480, pp. 758-761, April 2001.

[15] T. Cwik, S. Fernandez, A. Ksendzov, C. C. La Baw, P. D. Maker and R. E. Muller, "Multi-bandwidth frequency selective surfaces for near infrared filtering: design and optimization," *IEEE Int. Symp. Antennas & Propagat.*, vol. 3, pp. 1726-1729, 11-16 July *1999*, Orlando, FL.

[16] T. Cwik and G. Klimeck, "Integrated design and optimization of microelectronic devices", *IEEE Proc. Aerospace Conference*, vol. 5, pp. 131-138, 6-13 March 1999.

[17] J. B. Pryor, "On Ohmic losses in frequency selective surfaces at near-infrared wavelengths", Ph. D dissertation, Ohio State University, 2003.

[18] T. K. Chang, R. J. Langley and E. A. Parker, "An active square loop frequency

selective surface", *IEEE micro. Guided Wave Lett.*, vol. 3, no. 10, pp. 387-388, Oct. 1993.

[19] B. Philips, E. A. Parker and R. J. Langley, "Active FSS in an experimental horn antenna switchable between two beamwidths", *Electron. Lett.*, vol. 31, no. 1, pp. 1-2, Jan. 1995.

[20] T. K. Chang, R. J. Langley and E. A. Parker, "Active frequency-selective surfaces", *IEE Proc. Microw. Antennas Propag.*, vol. 143, no. 1, pp. 62-66, Feb. 1996.

[21] E. A. Parker and S. B. Savia, "Active frequency selective surfaces with ferroelectric substrates", *IEE Proc. Microw. Antennas Propag.*, vol. 148, no. 2, pp. 103-108, Apr. 2001.

[22] B. Schoenlinner, A. Abbaspour-Tamijani, L. C. Kempel and G. M. Rebeiz, " Switchable low-loss RF MEMS Ka-band frequency-selective surface", *IEEE Trans. Microw. Theory & Tech.*, vol. 52, no. 11, pp. 2474-2481, Nov. 2004.

[23] J. C. Vardaxoglou, P. Y. Lau and M. Kearney, "Frequency selective surface from optically excited semiconductor on a substrate", *Electron. Lett.*, vol. 34, no. 6, pp. 570-571, 19 March 1998.

[24] D. S. Lockyer, J. C. Vardaxoglou and M. J. Kearney, "Plane wave transmission response of selectively doped and micromachined silicon wafers under optical illumination", *International Topical Meeting on Microwave Photonics,* vol. 1, pp. 169-172, 17-19 Nov. 1999.

[25] D. B. Webb, E. Michielssen and R. Mittra, "Thick frequency selective surfaces", *IEEE Int. Symp. Antennas & Propagat.*, vol. 4, pp. 1795-1798, 18-25 July 1992.

[26] H. Loui, E. F. Kuester, F. Lalezari and Z. Popovic, "Thick FSSs for large scan angle

applications", *IEEE Int. Symp. Antennas & Propagat.*, vol. 2, pp. 2172-2174, 20-25 June 2004.

[27] C. Antonopoulos, R. Cahill, E. A. Parker and I. M. Sturland, "Multilayer frequency-selective surfaces for millimeter and submillimetre wave applications", *IEE Proc. Microw. Antennas Propag.*, vol. 144, no. 6, pp. 415-420, Dec. 1997.

[28] K. Ueno, T. Itanami, H. Kumazawa and I. Ohtomo, "Characteristics of frequency selective surfaces for a multi-band communication satellite", *IEEE Int. Symp. Antennas & Propagat.*, vol. 2, pp. 735-738, 24-28 June 1991.

[29] T. K. Wu and S. W. Lee, "Evaluation of multi-band reflector antennas with frequency selective subreflectors", *IEEE Int. Symp. Antennas & Propagat.*, vol. 1, pp. 262-265, 28 June-2 July 1993.

[30] T. K. Wu, K. Woo, S. W. Lee, "Multi-ring element FSS for multi-band applications", *IEEE Int. Symp. Antennas & Propagat.*, vol. 4, pp. 1775-1778, 18-25 July 1992.

[31] R. J. Langley and E. A. Parker, "Equivalent circuit model for arrays of square loops", *Electron. Lett.*, vol. 18, no. 7, 1982, pp. 294-296.

[32] C. K. Lee and R. J. Langley, "Equivalent circuit models for frequency selective surfaces at oblique angles of incidence", *IEE Proc. Microw. Opt. Antennas*, vol. 132, no. 6, pp. 395-399, Oct. 1985.

[33] E. W. Lucas and T. P. Fontatna, "A 3-D hybrid finite element/boundary element method for the unified radiation and scattering analysis of general infinite periodic arrays", *IEEE Trans. Antennas Propagat.*, vol. 43, no. 2, pp. 145-153, Feb. 1995.

[34] P. Harms, R. Mittra and K. Wai, "Implementation of the periodic boundary condition in the finite-difference time-domain algorithm for FSS structures", *IEEE Trans.*

Antennas Propagat., vol. 42, no. 9, pp. 1317-1324, Sept. 1994.

[35] R. F. Harrington, *Field Computation by Moment Methods*, New York: IEEE Press, 1993.

[36] P. N. Kaleeba, A. Tennant, B. Chambers and J. P. Idez, "Electromagnetic analysis of active radar absorbers", *IEEE Int. Symp. Antennas & Propagat.*, vol. 4, pp. 295-298, 22-27 June 2003.

[37] P. T. Teo, X-F Luo, and C. K. Lee, "Transmission of convoluted periodic loop element with selective reflection", *Applied Physics Letters*, vol. 85, no.9, pp. 1454-1456, 30 August 2004.

[38] G. Manara, A. Monorchio and R. Mittra, "Frequency selective surface design based on genetic algorithm," *Electron. Lett.*, vol. 35, pp. 1400-1401, Aug. 1999.

[39] S. Chakravarty and R. Mittra, "On the Application of the Microgenetic Algorithm the Design of Broad-Band Microwave Absorbers Comprising Frequency-Selective Surfaces Embedded in Multilayered Dielectric Media," *IEEE Trans. Microw. Theory &Tech.*, vol. 49, no. 6, pp. 665-676, June 2001.

[40] S. Chakravarty and R. Mittra, "Application of the Micro-Genetic Algorithm (MGA) to the design of broad-band microwave absorbers using multiple frequency selective surface screens buried in dielectrics", *IEEE Trans. Antennas Propagat.*, vol. 50, no. 3, pp. 284-296, Mar. 2002.

[41] S. Chakravarty and R. Mittra, "Application of the Micro-Genetic Algorithm to the Design of Spatial Filters With Frequency-Selective Surfaces Embedded in Dielectric Media," *IEEE Trans. Electromagn Compatibility*, vol. 44, No.2, pp. 338-346, May 2002.

[42] S. Chakravarty and R. Mittra, "Design of a frequency selective surfaces (FSS) with very low cross-polarization discrimination via the parallel micro-genetic algorithm (PMGA)", *IEEE Trans. Antennas Propagat*., vol. 51, no. 7, pp. 1664-1668, July 2003.

[43] A. Qing and C. K. Lee, "An improved model for full wave analysis of multi-layered frequency selective surfaces with gridded square element," *Progress in Electromagnetics Research,* PIER 30, chap. 14, pp. 285-303, 2001.

[44] C. H. Tsao and R. Mittra, "Spectral-domain analysis of frequency selective surfaces comprised of periodic arrays of cross dipoles and Jerusalem crosses", *IEEE Trans. Antennas Propagat.*, vol. 32, no. 5, pp. 478-486, May 1984.

[45] A. Qing, X. Xu, and Y. B. Gan, "Spectral-domain method for the analysis of Frequency Selective Surfaces", *Technical report*, Temasek Laboratories, National University of Singapore, Dec. 6, 2004.

[46] I. Anderson, "On the Theory of self-resonant grids", *Bell Syst. Tech. J.*, vol. 54, no. 10, pp. 1725-1731, 1975.

[47] N. Marcuvitz, *Waveguide Handbook*, McGraw-Hill, New York, pp. 139-153 and 280-284, 1951.

[48] I. R. Wait, "Reflection at arbitrary incidence from a parallel wire grid", *Applied Sci. Res.*, vol. 4, pp. 393-400, 1954.

[49] M. J. Archer, "Wave reactance of thin planar strip gratings", *Int. J. Electronics*, vol. 58, no.2, pp. 187-230, 1985.

[50] R. J. Langley and E. A. Parker, "Double-square frequency selective surfaces and their equivalent circuit", *Electron. Lett.*, vol. 19, no. 17, pp. 675-677, 1983.

[51] C. K. Lee and R. J. Langley, "Design of single layer frequency selective surface", *Int. J. Electronics*, vol. 63, no. 3, pp. 291-296, 1987.

[52] R. J. Langley and A. J. Drinkwater, "Improved empirical model for the Jerusalem cross", *IEE Proc. Pt. H*, vol. 129, no. 1, pp. 1-6, 1982.

[53] J. A. Arnaud and F. A. Pelow, "Resonant-grid quasi-optical diplexer", *Bell Syst. Tech. J.*, vol. 54, no. 2, pp. 263-283, 1975.

[54] W. Gregorwich, "The design and development of frequency selective surfaces for phased arrays", *IEEE Proc. Aerospace conference*, vol. 5, pp. 471-479, 6-13 March 1999.

[55] S. B. Savia and E. A. Parker, "Equivalent circuit model for superdense linear dipole FSS", *IEE proc. Microw. Antennas Propag.*, vol. 150, no. 1, pp. 37-42, Feb. 2003.

[56] A. Gottvald *et al*., "Global optimization methods for computational electromagnetics", *IEEE Trans. Magn.*, vol. 28, pp. 1537-1540, Feb. 1992.

[57] P. G. Alotto, "Stochastic algorithms in electromagnetic optimization", *IEEE Trans. Magn.*, vol. 34, pp. 3674-3684, May 1998.

[58] J. H. Holland, *Adaptation in Natural and Artificial Systems*, Ann Arbor, MI: Univ. of Michigan Press, 1975.

[59] K. A. De Jong, "An analysis of the behavior of a class of genetic adaptive systems", *Ph. D dissertation*, Univ. Michigan, Ann Arbor, 1975.

[60] L. Davis, *Genetic Algorithm and Simulated Annealing*, London, U.K.: Pittman, 1987.

[61] D. E. Goldberg, *Genetic Algorithms in Search, Optimization and Machine Learning*, MA: Addison-Weiley, 1989.

[62] D. E. Goldberg and K. Deb, "A comparative analysis of selection schemes used in genetic algorithms", in *Foundations of Genetic Algorithms*, G. J. E. Rawlins, Ed. San Mateo, CA: Morgan Kaufmann, 1991.

[63] L. J. Eshelman and J. D. Schafer, "Real-coded genetic algorithms and interval-schemata", in *Foundation of Genetic Algorithms 2*, pp. 187-202, L. D. Whitley, ED. San Mateo, CA: Morgan Kaufmann, 1992.

[64] D. S. Weile and E. Michielssen, "Genetic algorithm optimization applied to electromagnetics: A review," *IEEE Trans. Antennas Propagat.*, vol. 45, no. 3, pp. 343-353, Mar. 1997.

[65] R. L. Haupt, "An Introduction to Genetic Algorithms for Electromagnetics," *IEEE Antennas and Propagation Magazine,* vol. 37, no. 2, pp. 7-15, April 1995.

[66] J. M. Johnson and Y. Rahmat-Samii, "Genetic algorithms in engineering electromagnetics", *IEEE Antennas and Propagation Magazine,* vol. 39, pp. 7-21, 1997.

[67] R. L. Haupt, "Thinned arrays using genetic algorithms", *IEEE Trans. Antennas Propagat.*, vol. 42, pp. 993-999, 1994.

[68] E. Michielssen, J.-M. Sajer, S. Ranjithan and R. Mittra, "Design of lightweight, broad-band microwave absorbers using genetic algorithms", *IEEE Trans. Microw. Theory & Tech.*, vol. 41, pp. 1024-1031, 1993.

[69] D. S. Weile, E. Michielssen and D.E. Goldberg, "Genetic algorithm design of Pareto optimal broad band microwave absorbers", *IEEE Trans. Electromag. Compatibility*, vol. 38, pp. 518-524, 1996.

[70] E. Michielssen, S. Ranjithan and R. Mittra, "Optimal multilayer filter design using real-coded genetic algorithms," *IEE Proc. J, Optoelectronics*, vol. 139, no. 6, pp. 413-420, Dec. 1992.

[71] A. Qing, C. K. Lee, and L. Jen, "Electromagnetic inverse scattering of two-dimensional perfectly conducting objects by real-coded genetic algorithm," *IEEE Trans. Geosci. Romote Sens.*, vol. 39, no. 3, pp. 665-676, 2001.

[72] E. Michielssen, J. M. Sajer, and R. Mittra, "Design of multilayered FSS and waveguide filters using genetic algorithms," *IEEE Int. Symp. Antennas & Propagat.*, vol.3, pp. 1936-1939, 1993.

[73] E. A. Parker, A. Chuprin, J. C. Batchelor, S. B. Savia, "GA optimization of crossed dipole FSS array geometry," *Electron. Lett.*, vol. 137, pp 996-997, August 2001.

[74] G. Manara, A. Monorchio, R. Mittra, "A new genetic-algorithm-based frequency selective surface for dual frequency application," *IEEE Int. Symp. Antennas & Propagat*, vol. 3, pp. 1722-1725, 11-16 July 1999.

[75] X. F. Luo, A. Qing and C. K. Lee, "The design of Frequency Selective Surfaces (FSS) Using Real-coded Genetic Algorithm (RGA)", *IEEE Fourth International Conference on Information, Communications & Signal Processing and Fourth Pacific-Rim Conference on Multimedia (ICICS-PCM 2003)*, vol. 1, pp. 391-395, Singapore 15-18 Dec. 2003.

[76] M. Ohira, H. Deguchi, M. Tsuji and H. Shigesawa, "Multiband single-layer frequency selective surface designed by combination of genetic algorithm and geometry-refinement technique", *IEEE Trans. Antennas Propagat.*, vol. 52, no. 11, pp. 2925-2931, Nov. 2004.

[77] A. Qing, C. K. Lee, and L. Jen, "Microwave imaging of parallel perfectly conducting cylinders using real-coded genetic algorithm," *Journal of Electromagnetic Waves and Applications*, vol. 13, pp. 1121-1143, 1999.

[78] K. A. Michalski, "Electromagnetic imaging of circular-cylindrical conductors and tunnels using a differential evolution algorithm," *Microw. Opt. Tech. Lett.*, vol. 27, no. 5, pp. 330-334, Dec. 2000.

[79] K. A. Michalski, "Electromagnetic imaging of elliptical-cylindrical conductors and tunnels using a differential evolution algorithm," *Microw. Opt. Tech. Lett.*, vol. 28, no. 3, pp. 164-169, Feb. 2001.

[80] K. V. Price, "Differential Evolution: A Fast and simple numerical optimizer," *Proc. North American Fuzzy Information Processing Conf.*, pp. 524-527, 1996.

[81] S. L. Cheng and C. Hwang, "Optimal Approximation of Linear Systems by a Differential Evolution Algorithm," *IEEE Transactions on Systems, Man, and Cybernetics-Part A: systems and humans*, vol. 31, no. 6, pp. 698-707, Nov. 2001.

[82] A. Qing, "Electromagnetic inverse scattering of multiple two-dimensional perfectly conducting objects by the differential evolution strategy", *IEEE Trans. Antennas Propagat.*, vol. 51, no. 6, pp. 1251-1262, June 2003.

[83] X. F. Luo, C. K. Lee and A. Qing, "Design of Frequency Selective Surfaces (FSS) Using Differential Evolution Strategy (DES)", *27th ESA Antenna Technology Workshop on Innovative Periodic Antennas: Electromagnetic Bandgap, Left handed materials, Fractal and Frequency Selective Surfaces*, Santiago de Compostela, Spain, pp. 201-207, 9-11th Mar. 2004.

[84] X. F. Luo, P. T. Teo, A. Qing and C. K. Lee, "Design of double-square-loop frequency selective surfaces using differential evolution strategy coupled with equivalent circuit model," *The 4th international conference on microwave and millimeter wave technology*, Aug. 18-21, 2004, pp. 94-97, Beijing, China.

[85] X. F. Luo, A. Qing and C. K. Lee, "On the Application of Differential Evolution Strategy to the Design of Frequency Selective Surfaces", *Int. J. RF. Microw. CA Engineer.*, USA, vol. 15, no. 2, pp. 173-180, March 2005.

[86] X. F. Luo, P. T. Teo, A. Qing and C. K. Lee, "Design of Double-Square-Loop Frequency Selective Surfaces Using Differential Evolution Strategy Coupled with Equivalent Circuit Model", *Microw. Opt. Tech. Lett.*, vol. 44, no. 2, pp. 159-162, 20 Jan. 2005.

[87] C. H. Tsao, "Spectral-domain approach for analyzing scattering from frequency selective surfaces", *Ph.D. Dissertation*, 1981.

[88] M. M. A. Allam, E. A. Parker, "Aspects of frequency selective surfaces: finite arrays of dipoles", *Fifth National Radio Science Conference*, Cairo, pp. 16-18, 1998.

[89] T. K. Wu, "Four-band frequency selective surface with double-square-loop patch elements", *IEEE Trans. Antennas Propagat.*, vol. 42, no. 12, pp. 1659-1663, Dec. 1994.

[90] E. A. Parker and J. C. Vardaxoglou, "Plane-wave illumination of concentric-ring selective surfaces", *IEE Proc. H*, vol. 132, no. 3, pp. 176-180, 1985.

[91] J. C. Vardaxoglou and E. A. Parker, "The performance of two tripole arrays as frequency selective surfaces", *Electron. Lett.*, vol. 19, pp. 709-710, 1983.

Appendix A

Method of Moments (MoM)

Eq. (2-14) can be solved with the Method of Moments (MoM). In this appendix, the basic description of Moment of method (MoM) is presented [34], which is applied to solve the integrated equation in the analysis of FSS performance. Consider the inhomogeneous equation

$$L(u) = g \tag{A-1}$$

where u is the unknown induced current to be determined, g is the known incident field, and L is a linear operator relating the unknown u to the known g.

Let u be expanded in a series of basis functions as

$$u = \sum_n a_n f_n \tag{A-2}$$

where a_n are unknown coefficients. Substituting (A-2) into (A-1), we get

$$\sum_n a_n L(f_n) = g \tag{A-3}$$

We take the inner product of (A-3) with each test function w_m. Then,

$$\sum_n a_n \langle w_m, L(f_n) \rangle = \langle w_m, g \rangle, \qquad m = 1, 2, 3, \cdots \tag{A-4}$$

The scalar product $\langle a, b \rangle$ is defined as

$$\langle a, b \rangle = \int_s a^* b ds \tag{A-5}$$

where a^* is the complex conjugate of a. (A-4) can be written in matrix form as

$$[L_{mn}][a_n] = [g_m] \tag{A-6}$$

where,

$$[L_{mn}] = \begin{bmatrix} \langle w_1, Lf_1 \rangle & \langle w_1, Lf_2 \rangle & \cdots \\ \langle w_2, Lf_1 \rangle & \langle w_2, Lf_2 \rangle & \cdots \\ \cdots & \cdots & \cdots \end{bmatrix}$$

$$[a_n] = \begin{bmatrix} a_1 \\ a_2 \\ \vdots \end{bmatrix}$$

$$[g_m] = \begin{bmatrix} \langle w_1, g \rangle \\ \langle w_2, g \rangle \\ \vdots \end{bmatrix}$$

In Galerkin's method, the test function is chosen to be the same function as the basis function.

Appendix B

Floquet's Theorem

Floquet's theorem states that if a linear differential equation has periodic coefficients and periodic boundary conditions, then the stable solutions will generally be a periodic function times an exponentially decreasing function.

In this appendix, we give the derivation of eq. (2-13). Assuming that a periodic structure has an infinite number of periods, for simplicity, let us consider a singly periodic structure that is assumed to be infinite and uniform in x direction and y direction. According to Floquet's theorem, the current in x direction in the periodic structure can be described as

$$J'(x) = J(x)e^{-jk_x^{inc}x} \tag{B-1}$$

The current in x direction satisfies the following equation [3]

$$J(x+P_x) = J(x)e^{jk_x^{inc}P_x} \tag{B-2}$$

where k_x^{inc} and P_x are the incident wave number and periodicity in the x direction, respectively.

Consequently,

$$J'(x+P_x) = J(x+P_x)e^{-jk_x^{inc}(x+P_x)}$$
$$= J(x)e^{jk_x^{inc}P_x}e^{-jk_x^{inc}(x+P_x)} = J(x)e^{-jk_x^{inc}x} = J'(x) \quad \text{(B-3)}$$

Hence, $J'(x)$ is a periodic function with a periodicity of P_x that can be represented by a Fourier series:

$$J'(x) = \sum_{m=-\infty}^{\infty} \tilde{J}_m e^{j(2m\pi/P_x)x} \quad \text{(B-4)}$$

Thus, $J(x)$ can be expressed as

$$J(x) = \sum_{m=-\infty}^{\infty} \tilde{J}_m e^{j(2m\pi/P_x+k_x^{inc})x} \quad \text{(B-5)}$$

The same approach is applied in y direction, therefore, we can get

$$J(x,y) = \sum_{m=-\infty}^{\infty}\sum_{n=-\infty}^{\infty} \tilde{J}_{mn} e^{j(2m\pi/P_x+k_x^{inc})x} e^{j(2n\pi/P_y+k_y^{inc})y} \quad \text{(B-6)}$$

The eq. (2-13) is obtained.

Appendix C

Detailed Flowchart of DES

For the readers' further understanding, the detailed flow chart of DES is shown in Figure C-1. Input parameters include the number of optimization parameters N_{par}, size of population N_{pop}, crossover probability P_{cross}, mutation intensity P_{mut} and convergence criterion. The convergence conditions will be satisfied when the objective function $f(x)$ is less than an acceptable value or the program will be terminated after maximum specified generations. ε is an acceptable value which is defined by the user and *Objf* represents the value of objective function. The detailed mutation operation and crossover operation are also shown in Figure C-2 and Figure C-3 respectively.

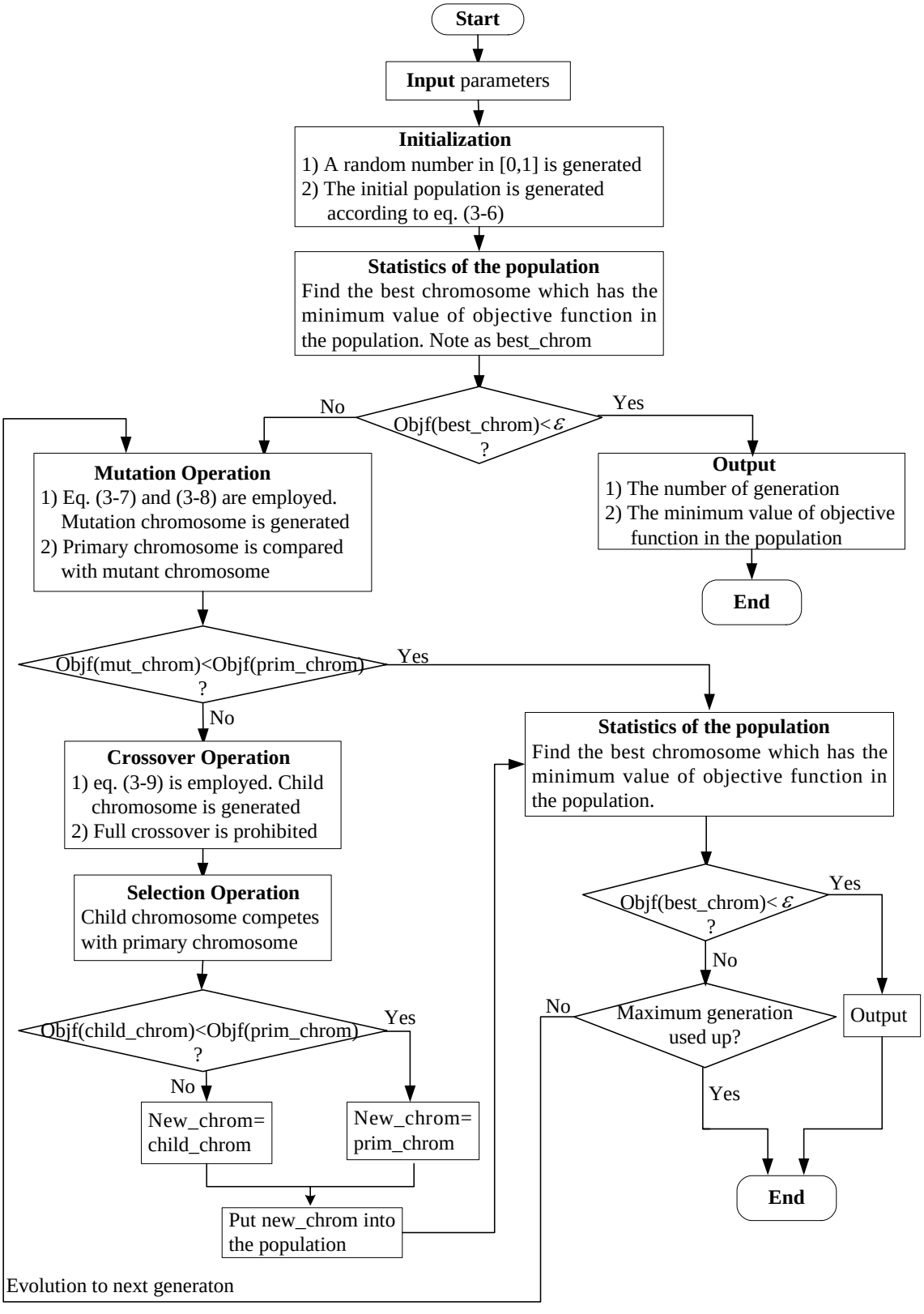

Figure C-1 The main flow chart of DES

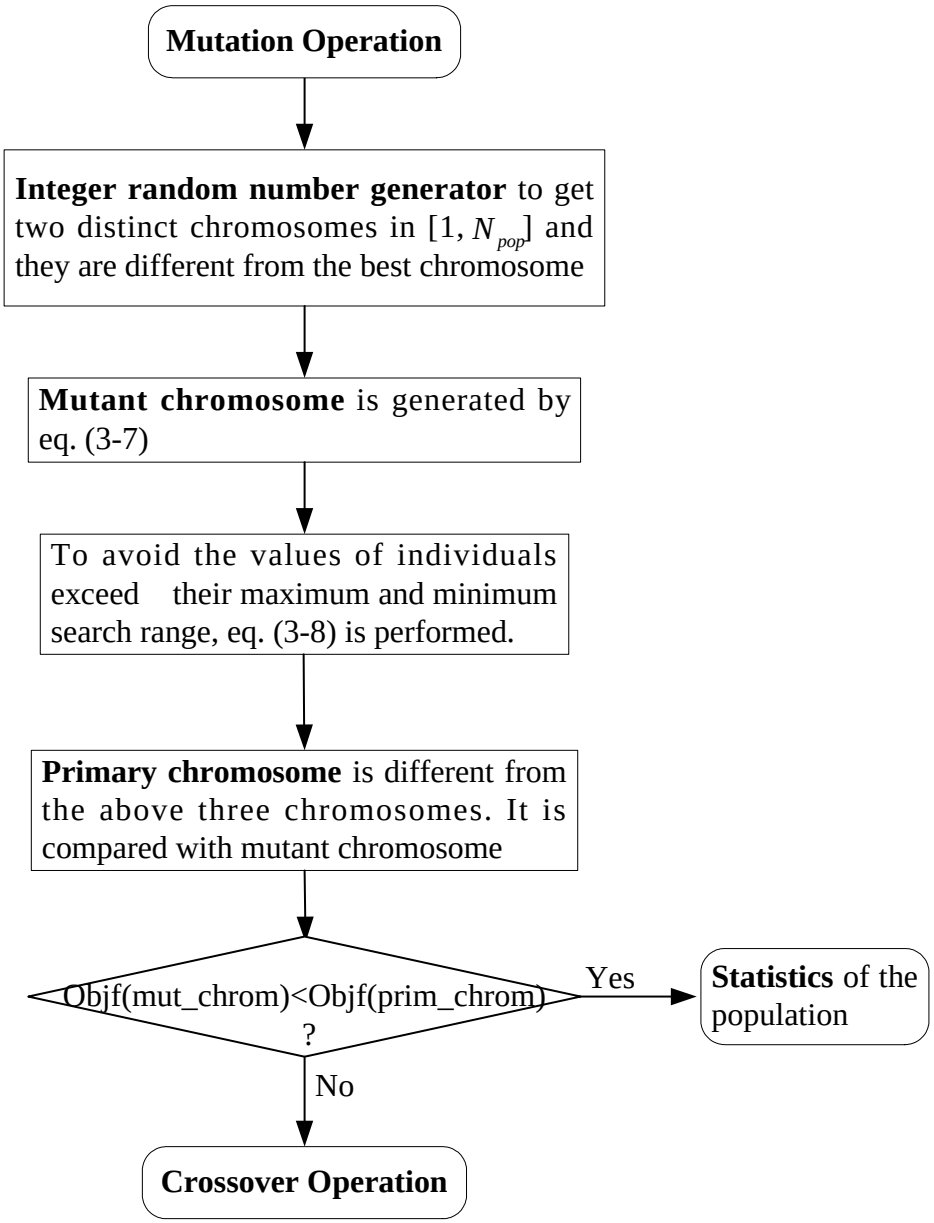

Figure C-2 Flow chart of mutation operation in DES

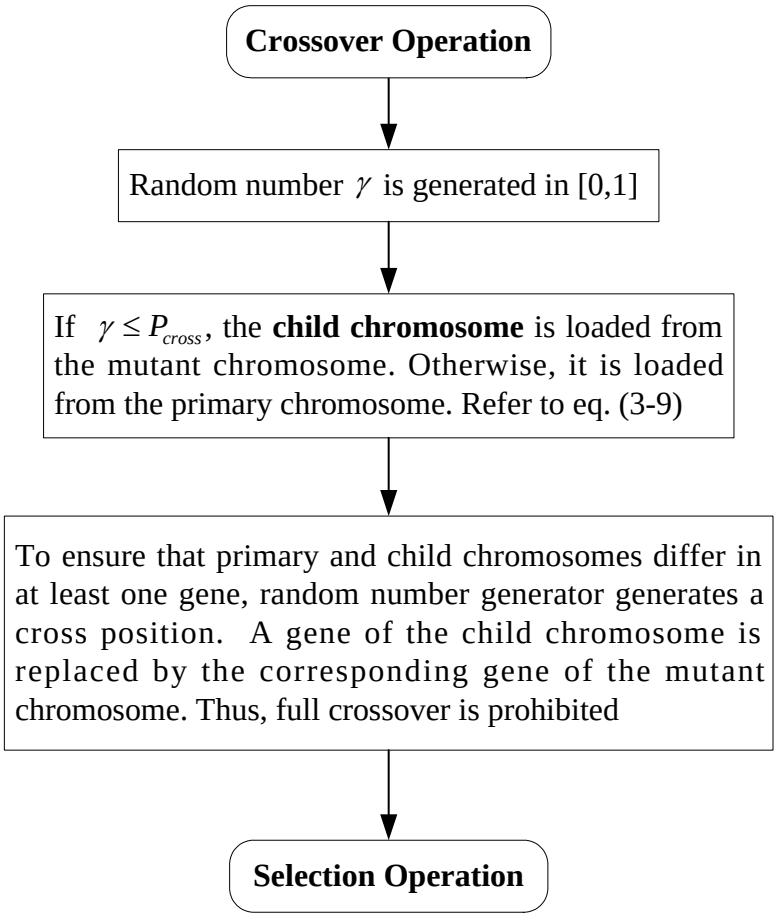

Figure C-3 Flow chart of crossover operation in DES

Appendix D

Measurements in NTU

The measurements of transmission response can be performed in an anechoic chamber by placing the FSS surface between two horn antennas. An ideal anechoic chamber is to provide an environment free of reflecting objects and electromagnetic interfering signals. The low reflectance is achieved by the use of an electromagnetic wave absorbent layer, often pyramidal in shape, covering all of the reflecting surfaces within the chamber. The installed chamber is electromagnetically shielded. This treatment eliminates the reflection of test signals beyond the test area or the penetration of external signals, which penetrate the test area causing distortion or difficulty in obtaining repeatable test results.

The measurement results presented in this thesis were conducted in the anechoic chamber at the school of EEE, Nanyang Technological University, as shown in Figure D-1. The set-up equipment included 2 ridge-horn antennas, a FSS holder bracket (non-metallic), a network analyzer and a spectrum analyzer. This experimental setup uses standard-gain horns as transmitting and receiving antennas. By turning the horn antenna's polarization from vertical to horizontal, it is possible to measure TE and TM transmission characteristics of the FSS test panel between the two horns. The transmitting antenna was

located at a distance of 177cm from the stand and the receiving one at 87cm. The measurements were made in the far-field region, where the minimum distance is $2D^2/\lambda$.

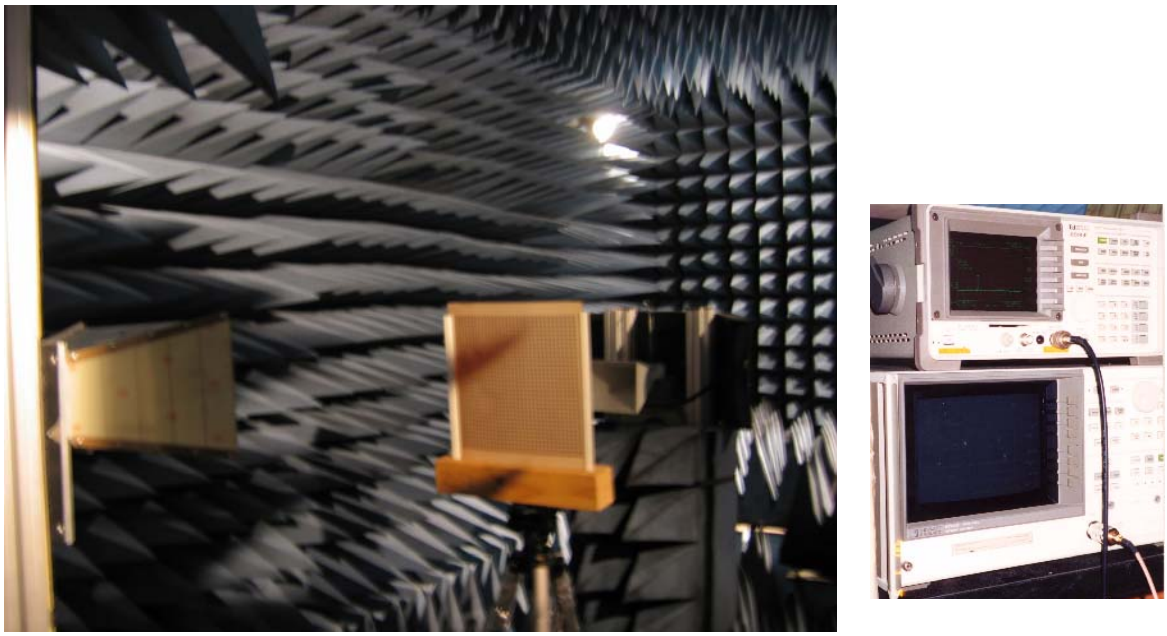

Figure D-1 FSS measurements in the anechoic chamber of NTU

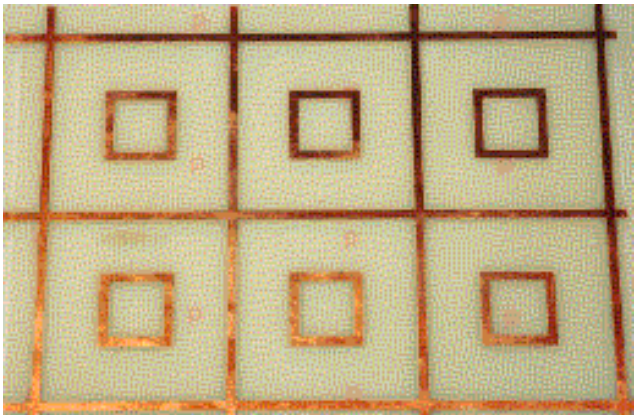

(a)

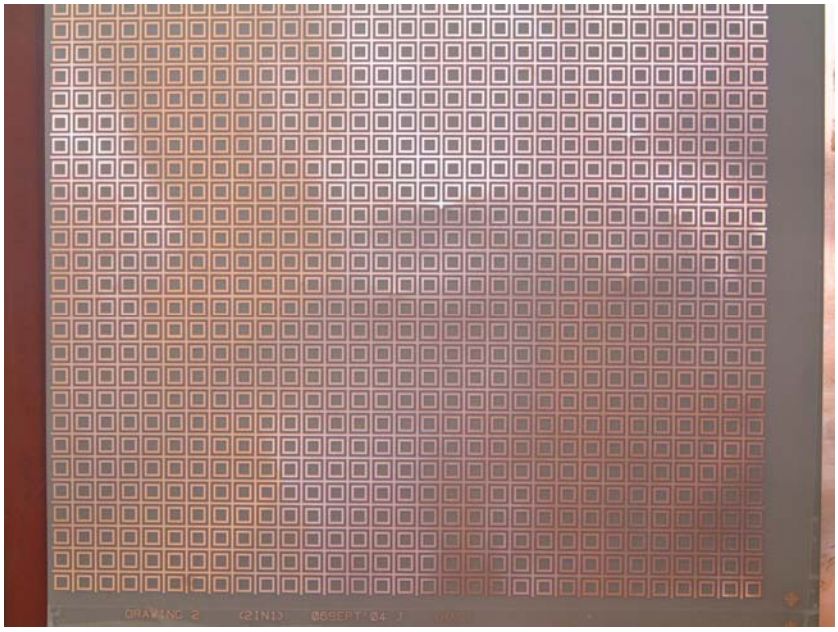

(b)

Figure D-2 Pictures of FSS arrays fabricated for this thesis (a) gridded-square array for 1-3GHz application (b) double-square array for triple-band application